2023

Development of a Quasi-Dimension GCI Combustion Model Aided by CFD

Jinsu Kim
West Virginia University, jk0062@mix.wvu.edu

Recommended Citation

Kim, Jinsu, "Development of a Quasi-Dimension GCI Combustion Model Aided by CFD" (2023). *Graduate Theses, Dissertations, and Problem Reports*. 12230.
https://researchrepository.wvu.edu/etd/12230

Development of a Quasi-Dimension GCI Combustion Model Aided by CFD

Jinsu Kim

Dissertation submitted to the
Benjamin M. Statler College of Engineering and Mineral Resources
at West Virginia University
in partial fulfillment of the requirements for the degree of
Doctor of Philosophy
in
Mechanical Engineering

Hailin Li, Ph.D., Chair
Cosmin Dumitrescu, Ph.D.
Harold Sun, Ph.D.
Kenneth Means, Ph.D.
Scott Wayne, Ph.D.
V'yacheslav Akkerman, Ph.D.

Department of Mechanical and Aerospace Engineering
Morgantown, West Virginia
2023

Keywords: Premixed combustion, GCI engine, System simulation, CFD,
Combustion model, VVA, CCSCR

Abstract

Development of a Quasi-dimension GCI Combustion Model Aided by CFD

Jinsu Kim

Advanced combustion strategies have been proposed to improve fuel efficiency while minimizing exhaust emissions. Gasoline compression ignition (GCI) combustion featuring partially premixed compression ignition (PPCI) and diffusion combustion has been recognized as an attractive, viable combustion strategy for its potential and advantages over conventional diesel and gasoline engines. The optimization of the GCI engine system requires the development of a quasi-dimensional GCI combustion model capable of simulating GCI combustion while requesting less computational burden than CFD simulation, which is very critical in engine system simulation.

This study developed a quasi-dimension, phenomenological combustion model for PPCI and diffusion combustion to facilitate the early development of GCI combustion strategy. Due to the limited GCI engine test results, additional parametric CFD studies were conducted and served as a reference to develop the GCI combustion model and investigate the effect on GCI combustion of thermal conditions typically considered during early strategy development. A reduced toluene primary reference fuel and ethanol (TPRFE) mechanism with 65 species and 283 reactions was used to simulate GCI combustion in CFD and quasi-dimension models. Additionally, the behavior of high-pressure gasoline spray was investigated using CFD to support the development of the phenomenological spray dynamics model.

The traditional phenomenological SI and CI combustion model frameworks were improved to simulate gasoline PPCI-diffusion combustion accurately with the spray dynamics, air entrainment, ignition delay, and heat release sub-models. The traditional spray model was improved and validated using CFD simulation results as a reference. The CFD result identified a high level of fuel concentration at the spray tip due to the drag and pushing momentum by the following fuel packets. This observation was accounted for in the development of the spray model. The ignition delay was calculated by solving the chemistry kinetics and curve fitting using the identical chemistry mechanism employed in CFD analysis. This research demonstrated that the phenomenological combustion model developed in this study could simulate fuel spray, fuel atomization, ignition delay, and heat release process.

The GCI model has been integrated into GT-Suite and successfully applied to improve the combustion process with the valvetrain system. Various variable valve actuation (VVA) strategies were investigated at low-load operating conditions, including early exhaust valve open (EEVO), late exhaust valve open (LEVO), negative valve overlap (NVO), positive valve overlap (PVO), and exhaust gas rebreathing (RB). The RB strategies were identified as the most effective in promoting in-cylinder gas temperature by increasing the hot internal residual gas fraction.

This research also numerically investigated the potential of a close coupled-selective catalytic reduction (CC-SCR) system in further NOx emissions of a heavy-duty diesel engine using GT-suite. Diesel engine transient test results were utilized to evaluate CC-SCR instead of GCI results due to limited GCI testing data available. The effects of volume and geometry of the CC-SCR on NOx reduction were numerically investigated under the HD FTP transient cycle. The simulation results revealed that CC-SCR was a very effective strategy, showing that nearly 80 %

of the total reduction was realized at the CC-SCR under the transient cycle. This study examined the necessity of accounting for the non-uniform distribution of exhaust gas and urea in the SCR model based on the observation of inhomogeneity at the inlet of CC-SCR in CFD simulation.

Acknowledgment

I would like to express my appreciation and thanks to my academic and research advisor, Dr. Hailin Li, for his invaluable guidance, patience, and encouragement while I pursued my doctoral studies at West Virginia University. I couldn't have finished my studies without everything he had done for me for years. I also appreciate my advisory committee members, Dr. Cosmin Dumitrescu, Dr. Harold Sun, Dr. Kenneth Means, Dr. Scott Wayne, and Dr. V'yacheslav Akkerman, not only for their lectures but also for their valuable time, suggestions, and comments on my research proposal and dissertation.

I especially want to thank Dr. Harold Sun for my internship experience at GAC in Detroit, MI, and research opportunity. Without his kind guidance and help, I couldn't have had industry experience and finished my internship successfully. I also thank Dr. Yu Zhang, Dr. Praveen Kumar, and Dr. Ashish Shah from Aramco America for sharing their valuable knowledge on GCI combustion, system-level analysis, comments, and engine test results. I thank Dr. Hongsheng Guo from the National Research Council Canada for providing me with his HCCI combustion model. I also appreciate Dr. Zhiming Gao for HD FTP cycle testing data and chemistry mechanism in the SCR model.

I thank DOE for my research funding (DE-EE0009654, Fast Simulation of Real Driving Emissions from Heavy-duty Diesel Vehicle Integrated with Advanced Aftertreatment System). I also thank Converge Science for providing the academic license of ConvergeCFD software and Gamma Technology for the GT-Power license and technical support.

Lastly, I would like to thank my parents for supporting me with their trust and love. I thank my friends for giving me unforgettable memories in Morgantown and their support.

Table of Contents

Chapter 1. Introduction 1
1.1 Background 1
1.2 Motivation 4
1.3 Brief Description of The Platform Used in This Study 8
1.4 Objective of Study 10
Chapter 2. Literature Reviews 12
2.1 Auto-Ignition Behavior 12
2.2 Low Temperature Combustion 15
2.3 Combustion Modeling Approaches 20
2.4 Multizone Combustion Model 24
2.5 1D/Phenomenological Spray Models. 24
2.6 Limitation of the 0/1D combustion model 26
Chapter 3. Simulation of GCI Combustion Using CFD 29
3.1 Gasoline Compression Ignition Engine 29
3.2 ConvergeCFD Model 30
3.3 CFD Model Validation Against Experimental Data 34
Validation at 2000 rpm / 12 bar IMEP 35
Validation at 2250 rpm / 18 bar IMEP 39
3.4 Examination of Factors Affecting GCI Combustion Using CFD 41
Effect of the Temperatures at IVC on Combustion and Emissions 41
Effects of Intake Pressures on Combustion and Emissions 48
Effect of EGR Rate on Combustion and Emissions 50
3.5 Summary 56
Chapter 4. Development of a Quasi-dimension PPCI-Diffusion Combustion Model and its Validation 58
4.1 Spray Dynamics 60
4.2 Multizone Model 71
4.3 Phenomenological Model 73
Phenomenological Flame Propagation Model 73

Phenomenological CI Combustion Model 78
4.4 Quasi-Dimensional GCI Combustion Model Validation and Results 89
Model Validation Against Testing Results 89
Intake Temperature Variation 91
Intake Pressure Variation 96
EGR Rate Variation 100
4.5 Summary 104
Chapter 5. GCI Combustion Model Application in a System-Level Simulation 105
5.1 1D GT Model Description 105
5.2 Variable Valve Actuation Strategy 107
5.3 Summary 118
Chapter 6. Numerical Investigation of the Potential of CC-SCR in Further Reducing NOx Emissions 119
6.1 CC-SCR CFD Simulation 119
6.2 SCR GT-Suite Model with Different Dimensions 122
6.3 Closed Coupled SCR GT Model Analysis 126
6.4 Summary 136
Chapter 7. Conclusions and Future Work 137
7.1 Conclusions of This Study 137
7.2 Future Work 140
Reference 142
Appendix I Reduced TPRF-E Mechanism 148
Appendix II Reduced SCR Mechanism 151

List of Figures

Figure 1: A typical process of combustion strategy development with incorporation of the CFD and thermodynamic combustion model 6
Figure 2 In-cylinder pressure and burn rate comparisons between CFD results and the current CI model available in GT-Power. 7
Figure 3 An example of GT-Power vehicle simulation configuration. 8
Figure 4 An example of an aftertreatment system for diesel engine system: DOC, DPF, and SCR. 9
Figure 5 The cylinder CAD model used in CFD closed-cycle analysis. 9
Figure 6 Auto-ignition heat release traces for PRF80 (two-stage ignition) and iso-octane (single-stage ignition) [16]. 13
Figure 7 Various advanced combustion strategies in the LTC concept. [17] 18
Figure 8 Combustion modeling approaches a) single zone, b) two-zone, and c) multi-zone model. 22
Figure 9 a) Illustration of fuel injection in packets and b) air-fuel mixing process within a packet [45]. 23
Figure 10 Schematic diagram of fuel injection model [65] 26
Figure 11 CFD mesh setup with the adapted mesh refinement. 34
Figure 12 Motoring in-cylinder pressure comparison between experiment and CFD results. 35
Figure 13 Comparison of the CFD simulated In-cylinder pressure and heat release rate with experimental data at 2000 rpm and 12 bar IMEP. 36
Figure 14 Comparison of CFD simulated combustion phasing and peak in-cylinder pressure with experimental data at 2000 rpm and 12 bar IMEP 37
Figure 15 Comparison of CFD simulated engine out NOx and CO emissions with experimental data at 2000 rpm and 12 bar IMEP. 37
Figure 16 Variation of NOx and CO simulated using CFD at 2000 rpm / 12 bar IMEP. 38
Figure 17 Comparison of the CFD simulated In-cylinder pressure and heat release rate with experimental data at 2250 rpm and 18 bar IMEP. 39
Figure 18 Comparison of CFD simulated combustion phasing and peak in-cylinder pressure with experimental data at 2250 rpm and 18 bar IMEP. 40

Figure 19 Comparison of the NOx and CO engine-out emissions from experiment and CFD simulation at 2250 rpm and 18 bar IMEP condition. 40
Figure 20 Variation of NOx and CO simulated using CFD at 2250 rpm / 18 bar IMEP. 41
Figure 21 Effect of intake temperature on GCI combustion at 1250 rpm 3 bar IMEP. 43
Figure 22 Mass species of H_2O_2 and OH as a function of CAD in 360, 380, and 400 K cases. .. 44
Figure 23 Effect of TIVC on combustion phasing, IMEP, and engine out CO and NOx emissions at 1250 rpm 3 bar IMEP. 44
Figure 24 Effect of TIVC on cylinder pressure and apparent heat release rate at 2000 rpm, 12 bar IMEP, and 360 K TIVC... 45
Figure 25 Effect of TIVC on combustion phasing, IMEP, and engine out CO and NOx emissions at 2000 rpm 12 bar IMEP. 46
Figure 26 Effect of TIVC on in-cylinder pressure and apparent heat release process at 2250 rpm and 18 bar IMEP in CFD simulation.. 47
Figure 27 Effect of TIVC on combustion phasing, IMEP, and Engine out CO and NOx emissions at 2250 rpm 18 bar IMEP. 47
Figure 28 Effect of PIVC on in-cylinder pressure and apparent heat release process at 2000 rpm and 12 bar IMEP in CFD simulation.. 48
Figure 29 Effect of PIVC on IMEP, combustion phasing, engine out NOx and CO emissions at 2000 rpm 12 bar IMEP. 49
Figure 30 Effect of PIVC on in-cylinder pressure and apparent heat release process at 2250 rpm and 18 bar IMEP in CFD simulation.. 49
Figure 31 Effect of PIVC on IMEP, combustion phasing, engine out NOx and CO emissions at 2250 rpm and 18 bar IMEP. 50
Figure 32 Effect of EGR rate on cylinder pressure and apparent heat release rate at 1250 rpm 3 bar IMEP, and 380 K TIVC. 51
Figure 33 Effect of EGR on the formation of H_2O_2 and OH at 1250 rpm, 3 bar IMEP, 380 K TIVC... 51
Figure 34 Effect of EGR on IMEP, combustion phasing, engine out NOx and CO emissions at 1250 rpm 3 bar IMEP, 380 K TIVC.. 52
Figure 35 Effect of EGR rate on cylinder pressure and apparent heat release rate at 2000 rpm 12 bar IMEP, and 360 K TIVC. 53

Figure 36 Effect of EGR rate on the formation of H_2O_2 and OH 2000 rpm, 12 bar IMEP, and 360 K TIVC. 54

Figure 37 Effect of EGR on IMEP, combustion phasing, engine out NOx and CO emissions at 2000 rpm 12 bar IMEP, and 360 K TIVC. 54

Figure 38 Effect of EGR on cylinder pressure and apparent heat release rate at 2250 rpm 18 bar IMEP, and 360 K TIVC. 55

Figure 39 Effect of EGR rate on H_2O_2 and OH at 2250 rpm, 18 bar IMEP, and 360 K TIVC. 55

Figure 40 Effect of EGR on IMEP, combustion phasing, engine out NOx and CO emissions at 2250 rpm, 18 bar IMEP, and 360 K TIVC. 56

Figure 41 Overall structure of the PPCI–diffusion combustion model. 59

Figure 42 Variation of high-pressure gasoline spray penetration length with change in time. High-pressure gasoline fuel injection penetration experiment [76]. 62

Figure 43 Comparison of variation of spray penetration measured in [76] with that predicted by the traditional penetration model [47], reference [75], and the modified model developed in this research. 63

Figure 44 Comparison between traditional model (a) and improved model (b). 64

Figure 45 History of the equivalence ratio at the center line of the fuel spray from CFD simulation. Start of injection was set at -20 °CA ATDC with 1500 bar injection pressure. 66

Figure 46 Equivalence ratio distribution at -6 °CA ATDC simulated using CFD model analysis. 66

Figure 47 Simulated distribution of the equivalence ratio vs penetration length at -6 °CA ATDC estimated by (a) improved spray model, (b) traditional spray model. 67

Figure 48 Equivalence ratio distribution under spray wall impingement condition. The wall location was 20 mm. 68

Figure 49 Illustration of turbulent flame propagation [81] 75

Figure 50 Flow chart of phenomenological CI combustion model in this study. 79

Figure 51 Illustration of direct fuel injection and phenomenological spray jet model. 79

Figure 52 Flow chart of the ignition delay sub-model. 81

Figure 53 Illustration of ignition location and flame radius. 84

Figure 54 A detailed flowchart of GCI model. 88

Figure 55 GCI model validation against experimental data at 2000 rpm, 12 bar IMEP 90
Figure 56 GCI model validation results against experimental data at 2250 rpm, 18 bar IMEP... 90
Figure 57 Validation of GCI model against CFD simulation data at 360, 380, and 400 K at IVC at 1250 rpm and 3 bar IMEP. 93
Figure 58 Validation of GCI model against CFD simulation data at 350, 360, and 370 K at IVC at 2000 rpm and 12 bar IMEP. 94
Figure 59 Validation of GCI model against CFD simulation data at 350, 360, and 370 K at IVC at 2250 rpm and 18 bar IMEP. 95
Figure 60 Validation of GCI model against CFD simulation data at 1.05, 1.1, and 1.15 bar at IVC at 1250 rpm and 3 bar IMEP, TIVC 380 K. 97
Figure 61 Validation of GCI model against CFD simulation data at 1.7, 1.8, and 1.9 bar at IVC at 2000 rpm and 12 bar IMEP, TIVC 360 K. 98
Figure 62 Validation of GCI model against CFD simulation data at 2.5, 2.6, and 2.7 bar at IVC at 2250 rpm and 18 bar IMEP, TIVC 360 K. 99
Figure 63 Validation of GCI model against CFD simulation data with EGR 20, 30, and 40 % at IVC at 1250 rpm 3 bar IMEP, TIVC 380 K. 101
Figure 64 Validation of GCI model against CFD simulation data with EGR 10, 20, and 30 % at IVC at 2000 rpm 12 bar IMEP, TIVC 360 K. 102
Figure 65 Validation of GCI model against CFD simulation data with EGR 10, 20, and 30 % at IVC at 2250 rpm 18 bar IMEP, 360 K. 103
Figure 66 A single cylinder engine GT model with sub-systems. 106
Figure 67 Variable valve actuation strategies simulated in this study: (a) EEVC and LEVC, (b) NVO, (c) PVO, (d) exhaust rebreathing with timings, and (e) exhaust rebreathing with variable lifts. 108
Figure 68 Exhaust and intake mass flow rate with EEVC and LEVC strategy. 110
Figure 69 Comparison of burned mass fraction, temperature at IVC, peak in-cylinder pressure, and PMEP with base/EEVC/LEVC valve strategies. 110
Figure 70 Exhaust and intake mass flow rate during valve overlap period with NVO and PVO strategy. 111
Figure 71 Comparison of burned mass fraction, temperature at IVC, peak in-cylinder pressure, and PMEP with base/NVO/PVO valve strategies. 111

Figure 72 Exhaust and intake mass flow rate with different timing of exhaust gas rebreathing strategy. 113
Figure 73 Comparison of burned mass fraction, temperature at IVC, peak in-cylinder pressure, and PMEP with base(NO-RB), RB-early(-20 ˚CA), RB-base, RB-late (+20 ˚CA) valve strategies. 113
Figure 74 Exhaust and intake mass flow rate with different lifts of exhaust gas rebreathing strategy. 114
Figure 75 Comparison of burned mass fraction, temperature at IVC, peak in-cylinder pressure, and PMEP with RB-base/RB-high lift/RB-low lift valve strategies. 114
Figure 76 LogP-logV diagram comparison with valvetrain strategies. 115
Figure 77 Summary of the effect of VVA strategies on (a) TIVC, (b) TEVO, (c) Max. in-cylinder pressure, (d) burned mass, (e) IMEP, and (f) PMEP. 117
Figure 78 3D CFD model of the closed coupled SCR system with a turbocharger. 120
Figure 79 Cross sectional diagram of gas velocity across the CC-SCR system. 121
Figure 80 Cross-sectional diagrams of velocity magnitude at 0.27, 0.35, and 0.41 m from the turbine outlet. 121
Figure 81 SCR model in GT-Suite. 123
Figure 82 Comparison of NOx emissions simulated by GT-Suite SCR model with experimental results [88]. 124
Figure 83 (a) Uniform and (b) non-uniform species distributions 125
Figure 84 NOx conversion efficiency with different mass flow rates, 1D and 3D, uniform, and non-uniform inlet distribution. 125
Figure 85 Impact of inlet temperature and model dimensions on computational time. 126
Figure 86 The CC-SCR and main SCR system in GT-Suite model. 127
Figure 87 Location of NOx measurement in simulation. 128
Figure 88 Accumulated NOx emitted from engine, CC-SCR, and main SCR. The volume of the CC-SCR varied from 10 % ~ 50 % of the main SCR 128
Figure 89 Variation of the temperatures at inlet, CC-SCR, and main SCR with time under the first 500 second HD FTP transient cycle simulation 130
Figure 90 Variation of the temperatures at the inlet, CC-SCR + main SCR case (scenario1), and main SCR only case under the first 500 second HD FTP transient cycle simulation .. 130

Figure 91 Impact of CC-SCR geometry on gas space velocity and NOx reduction efficiency of CC-SCR. 131

Figure 92 Accumulated NOx emissions at engine-out, CC-SCR out, and main SCR out. The volume of the CC-SCR varied from 10 % ~ 50 % with reduced main SCR volume accordingly. Total SCR volume was kept constant. 133

Figure 93 Effect of CC-SCR on the accumulated NOx after main SCR with/without increasing the total volume of the SCR system. 133

Figure 94 Instantaneous accumulated NOx, contribution at each SCR, concentration, and reduction efficiency of the NOx emission during HD FTP transient cycle with 30 % CC-SCR and total SCR volume of 15.7 L. 134

Figure 95 Instantaneous NOx concentration and reduction rate with main SCR only and 30 % CC-SCR case + main SCR. The volume of the total SCR is 15.7 L. 135

List of Tables

Table 1 Specification of the test engine in this study. 29

Table 2 Combustion models available in ConvergeCFD. 32

Table 3 Composition of TPRFE surrogate fuel used in this study. 33

Table 4 Detail sub-model for ConvergeCFD case setup. 33

Table 5 Engine test operating condition at 2000 rpm and 12 bar IMEP..................................... 36

Table 6 Engine test operating condition at 2250 rpm and 18 bar IMEP..................................... 40

Table 7 Operating condition and species composition employed in this simulation................... 42

Table 8 Experimental test conditions for vaporizing spray [74]... 61

Table 9 List parameters and values for used in Eq. 4.55 ~ Eq. 4.59... 82

Table 10 Summary of combustion characteristics of model and CFD simulations at 1250 rpm 3 bar IMEP. 93

Table 11 Summary of TIVC impact on combustion characteristics of GCI combustion at 2000 rpm 12 bar IMEP simulated by GCI model and CFD, respectively.............................. 94

Table 12 Summary of combustion characteristics of model and CFD simulations at 2250 rpm 18 bar IMEP. 95

Table 13 Summary of combustion characteristics of model and CFD simulations at 1250 rpm 3 bar IMEP. 97

Table 14 Summary of combustion characteristics of model and CFD simulations at 2000 rpm 12 bar IMEP. 98

Table 15 Summary of combustion characteristics of model and CFD simulations at 2250 rpm 18 bar IMEP. 99

Table 16 Summary of combustion characteristics of model and CFD simulations at 1250 rpm 3 bar IMEP. 101

Table 17 Summary of combustion characteristics of model and CFD simulations at 2000 rpm 12 bar IMEP. 102

Table 18 Summary of combustion characteristics of model and CFD simulations at 2250 rpm 18bar IMEP. 103

Table 19 Low-load engine operating condition simulated in this chapter................................. 106

Table 20 initial boundary conditions 120

Table 21 Boundary condition and inlet composition in this simulation. 123
Table 22 List of cases considered in this simulation. Total SCR volume (CC-SCR + main SCR) was increased. 127
Table 23 List of the cases considered in this simulation. Total SCR Vol. was kept constant at 15.7 L. 132

Nomenclature

AFR	Air Fuel Ratio
AHRR	Apparent Heat Release Rate
AMR	Adaptive Mesh Refinement
BMEP	Brake Mean Effective Pressure
CA	Crank Angle
CA10	Crank Angle corresponding to 10 % of total heat release
CA50	Crank Angle corresponding to 10 % of total heat release
CA90	Crank Angle corresponding to 50 % of total heat release
CAD	Crank Angle Degree
CC-SCR	Closed Coupled Selective Catalytic Reduction
CEQ	Chemical Equilibrium
CFD	Computational Fluid Dynamics
CI	Compression Ignition
CO	Carbon Monoxide
CO_2	Carbon Dioxide
CPSI	Cells per squire inches
CTC	Characteristic Time Combustion
DOC	Diesel Oxidation Catalyst
DPF	Diesel PM Filter
ECFM	Extended Coherent Flame Model
EEVO	Early Exhaust Valve Overlap
EGR	Exhaust Gas Recirculation
EVO	Exhaust Valve Opening
EXP	Experiment
FGM	Flamelet Generated Manifold
FTP	Federal test procedure
GA	Genetic Algorithm
GCI	Gasoline Compression Ignition
GDCI	Gasoline Direct Injection Compression Ignition
GHG	Green House Gases
HC	Hydro Carbon
HCCI	Homogeneous Charge Compression Ignition
HD	Heavy duty
HFS	High Fuel Stratification
HP	High Pressure
HRR	Heat Release Rate
HTHR	High Temperature Heat Release
IC	Internal Combustion
IMEP	Indicated Mean Effective Pressure
ISFC	Indicated Specific Fuel Consumption
ITHR	Intermediate Temperature Heat Release
IVC	Intake Valve Closing
KH	Kelvin-Helmholtz
LD	Light Duty
LEVO	Late Exhaust Valve Overlap
LP	Low pressure
LTC	Low-Temperature Combustion
LTHR	Low Temperature Heat Release
MFS	Medium Fuel Stratification
MPRR	Maximum Pressure Rise Rate
NOx	Nitrogen Oxides
NTC	No Time Counter
NVO	Negative Valve Overlap
ODE	Ordinary Differential Equation
PCCI	Premixed Charge Compression Ignition
PCP	Peak Cylinder Pressure
PFR	Primary Reference fuel
PFS	Partial Fuel Stratification
PIVC	Pressure at intake valve closing
PM	Particulate Matter
PMEP	Pumping Mean Effective Pressure
PPCI	Partially Premixed Compression Ignition
PRR	Pressure Rise Rate
PVO	Positive Valve Overlap
RB	Rebreathing

RCCI	Reactivity-Controlled Compression Ignition
RIF	Representative Interactive Flamelet
ROI	Rate of Injection
RPM	Revolution per minute
RT	Rayleigh-Taylor
SCCI	Stratified Charge Compression Ignition
SCR	Selective Catalytic Reduction
SI	Spark Ignition
SMD	Sauter Mean Diameter
TCM	Thermodynamic Combustion Models
TDC	Top Dead Center
TEVO	Temperature at Exhaust Valve Opening
TIVC	Temperature at Intake Valve Closing
TPRFE	Toluene Primary Reference Fuel, and Ethanol
TWC	Three-Way Catalyst
UI	Uniformity Index
VVA	Variable Valve Actuation

Chapter 1. Introduction

1.1 Background

According to the International Energy Agency report, the global carbon dioxide (CO_2) emission from the transportation sector in 2022 is rebounding by 3 % compared to the previous year as passenger and cargo transportation have increased. Despite the anticipated demand, achieving the Net Zero Emissions by 2050 scenario still requires the reduction of CO_2 in the transportation sector by 20 % to 5.7 Gt by 2030 [1]. In this regard, the US Environmental Protection Agency (EPA) revised the current greenhouse gas (GHG) standards and announced that the fleet-wide CO_2 compliance target will be lowered by 28 % for light-duty (LD) from 2023 model year (MY) through 2026 MY. Furthermore, for heavy-duty (HD) standards, California Air Resources Board (CARB) is considering lowering the on-road HD vehicle tailpipe nitrogen oxides (NOx) emissions by 90 %, down to 0.027 g/kWh by 2027. Meanwhile, the second phase of GHG regulation from the US EPA requires a 3% CO_2 reduction for HD vehicles from 2021 to 2027 [2].

Conventional internal combustion (IC) engines, such as spark-ignited (SI) and compression ignition (CI) engines, have been facing significant challenges to meet emission regulations. The major challenges of SI engines are the knock-limited compression ratio, pumping loss due to the throttling effect in low load, and excessive emissions during the cold start period before the light-off temperature of the three-way catalyst (TWC) is achieved. The pumping loss during intake stroke can be reduced by employing variable valvetrain actuation strategies (VVA), such as early or late intake valve closing (IVC). Also, it was shown that more than 80 % of the total emissions from SI engines were observed due to the lower conversion efficiency of TWC during the cold start process [3, 4]. Therefore, several strategies have been investigated and applied to minimize excessive emissions during the cold-start period. The most popular methods are a fuel-rich mixture, retarded combustion phasing, and close-coupled TWC [5]. However, the fuel-rich mixture strategy results in high-level emission of hydrocarbon (HC) and carbon monoxide (CO) due to the incomplete combustion and fuel consumption penalty. For CI engines, despite the better thermal efficiency than SI engines, the trade-off between particulate matter (PM) and NOx is the most difficult challenge.

To meet the stringent emissions regulations, CI engines have to be equipped with expensive aftertreatment systems such as Diesel Oxidation Catalyst (DOC), Diesel PM Filter (DPF), and Selective Catalytic Reduction (SCR) system. DOC oxidates CO and unburned HC with oxygen stored in monoliths into CO_2 and water [6]. DPF is also a honeycomb-shaped monolith that collects PM emitted from a diesel engine, and the collected PM is burned by a process called DPF regeneration. SCR is one of the technologies developed to convert NOx into N_2 and water, using urea injected into exhaust gas [7]. Although these systems effectively minimize harmful emissions, aftertreatment systems entail sophisticated controls and a high maintenance cost. Therefore, it is ideal to reduce the engine-out emissions, which lowers the dependency on the aftertreatment systems and the complexity of the applications.

There has been research on advanced combustion technologies that differ from the conventional approaches to mitigate these issues. The homogeneous charge compression ignition (HCCI) strategy was one of the possible solutions proposed in early studies to mitigate both NOx and PM simultaneously by early fuel injection and forming a lean homogeneous air-fuel mixture before combustion. Also, low combustion temperature by premixed charge reduces the heat loss from the engine combustion chamber to the coolant. Thus, it shows high thermal efficiency. However, the HCCI engine has been criticized for its high CO and HC emissions due to the incomplete combustion resulting from long ignition delay and the air-fuel mixture at the combustion chamber boundary, including the crevice. Moreover, the fact that HCCI is highly governed by chemistry kinetics and the lack of direct control over the combustion phase makes it difficult to employ HCCI in vehicle applications [8-10]. The extremely high peak cylinder pressure (PCP) and maximum pressure rise rate (MPRR) because of the simultaneous ignition also made applying HCCI combustion at a high load very difficult.

Numerous innovative low-temperature combustion (LTC) strategies have also been proposed in the past decades to overcome the drawbacks and limitations of HCCI combustion. The strategies examined include different fuels, fuel injection strategies altering the degree of stratification, and varying bulk gas temperature and pressure, such as variable valve timing and Exhaust Gas Recirculation (EGR). One of the crucial factors of fuel for LTC is the chemical reactivity of the fuel. Diesel-like fuels are usually challenging to atomize and evaporate but have short chemical ignition delay. In contrast, gasoline-like fuels have relatively short but strong molecule bonds, making them less reactive and having longer ignition delays [11]. The premixed charge compression ignition (PCCI) combustion strategy uses diesel fuel and has early injection, which provides enough time for fuel to form a premixed air-fuel mixture. Also, reactivity-controlled compression ignition (RCCI) was proposed and demonstrated using two fuels that show different chemical reactivities [12-14]. Low reactivity fuel was injected into the intake manifold either during the intake stroke or early compression stroke for premixed charge preparation. Then, the second fuel with high reactivity was injected to initiate the ignition. However, the application of RCCI has been criticized for the need for two fuels stored onboard.

Fundamentally, the LTC concept is to realize lower temperatures during combustion than conventional combustion by minimizing locally fuel-rich regions. In this regard, gasoline's low reactivity and long ignition delay would be helpful because it provides ample time to avoid locally rich areas in a highly diluted environment. LTC can be achieved by fuel stratification and fuel reactivity.

Gasoline Compression Ignition (GCI) combustion can be categorized into three modes by the degree of fuel stratification: partial fuel stratification (PFS), medium fuel stratification (MFS), and high fuel stratification (HFS) [15]. Nevertheless, the low reactivity and high latent heat of the gasoline poses some challenges in low-load operating conditions and during cold start. On the one hand, the longer ignition delay due to low reactivity is suitable since it offers longer mixing time than diesel to create a premixed charge in high-load operating conditions. On the other hand, at low load conditions where the thermal condition in the engine cylinder is not favorable for autoignition, air and fuel tend to over-mix and become too lean to ignite. As a result, significant levels of CO and HC are emitted under low load conditions, and additional thermal energy input is needed to promote the self-ignition of the fuel in cold start and light load conditions.

1.2 Motivation

Combustion strategy establishment during engine development generally encompasses extensive investigation in testing and numerical analysis. Although engine testing can produce actual final outputs, it often requires significant efforts and financial costs associated with the testing process. It won’t be very effective during the early development stage when a different platform is examined before hardware is available. Additionally, instrumental limitations and availability often pose limitations in measuring physical parameters and analyzing phenomena in a cylinder, such as temperature and species distribution. Consequently, numerical simulation study is often utilized along with feasibility testing to fill the gap between these two methods.

The typical process of utilizing a simulation approach for engine development incorporates Computational Fluid Dynamics (CFD) results with 0D/1D simulations. Once CFD results are available in a particular operating condition, the estimated heat release rate from CFD is derived and implemented into a system-level simulation to evaluate the performance of the engine system at the operating condition, as shown in Figure 1. This approach will provide accurate estimation in early development without real hardware. However, in this way, it is required to run all the cases of interest to obtain the heat release rate from CFD, and this will take a significant amount of time. Moreover, the changes in other factors, such as EGR, intake temperature, and intake pressure, cannot be taken into consideration accordingly if the heat release rate is extracted from a case setup that differs from the actual operating condition. Also, the engine control strategy is often constructed and coupled with the aftertreatment system to meet stringent emissions standards. The lack of a thermodynamic GCI combustion model makes optimizing engine control strategy and minimizing tailpipe emissions hard. Therefore, developing a combustion model for a system-level simulation tool is necessary.

Despite the fact that existing conventional combustion models for SI and CI engines have been extensively adopted for numerous research, they may not be an appropriate method to simulate the behavior of partially premixed compression ignition (PPCI)-diffusion combustion due to its different combustion processes.

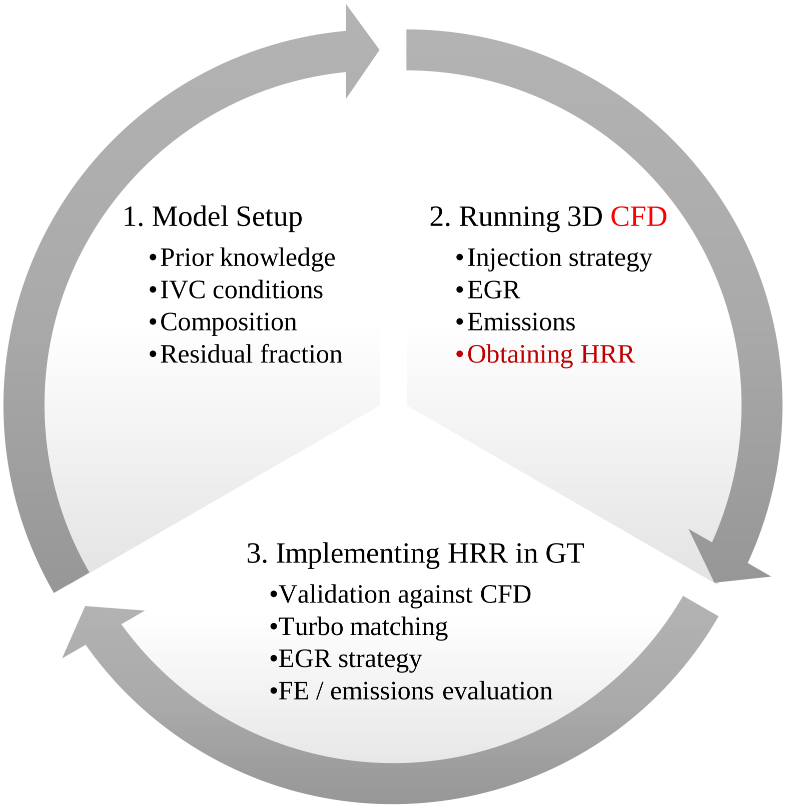

Figure 1: A typical process of combustion strategy development with incorporation of the CFD and thermodynamic combustion model.

In the PPCI strategy, the first injection during late compression stroke forms a partially premixed charge, and it is locally stratified, unlike HCCI or conventional SI combustion, due to a shorter mixing time while it is globally lean. The locally stoichiometric but overall lean air-fuel mixture can be 1) auto-ignited in a particular region or 2) remain unburned due to unfavorable local thermal conditions in the cylinder. However, the current SI combustion model assumes that the air-fuel mixture in the combustion chamber is ideally homogeneous or almost uniform and that fuel burns by flame propagation in a cylinder. Therefore, the current SI model is not suitable for simulating PPCI combustion. Although the compression ignition combustion model has been proven to predict diesel premixed and diffusion combustion accurately, the model cannot be readily used for PPCI. It still needs to be calibrated for gasoline fuel and partially premixed combustion because diesel combustion usually has a short premixed combustion period caused by ignition delay. Figure 2 shows the preliminary comparison results at different operating points between the CFD results and the current 0/1D CI model in commercial software. The CI model is first calibrated to 2250 rpm / 16 bar BMEP condition as shown in (a) in the figure. Air entrainment, ignition delay, and each premixed and diffusion combustion rate were calibrated, utilizing a genetic algorithm (GA). Although the heat release estimation showed a marginal error, the PPCI and diffusion combustions correlated well with the CFD result.

However, when the calibrated model was used at different low load conditions denoted as (b), the premixed combustion stage was also poorly predicted since the low reactivity of the gasoline caused the longer ignition delay. The longer delay made the combustion comparable to the premixed combustion. This simple comparison result necessitates developing a combustion model which comprises partially premixed and diffusion GCI combustion.

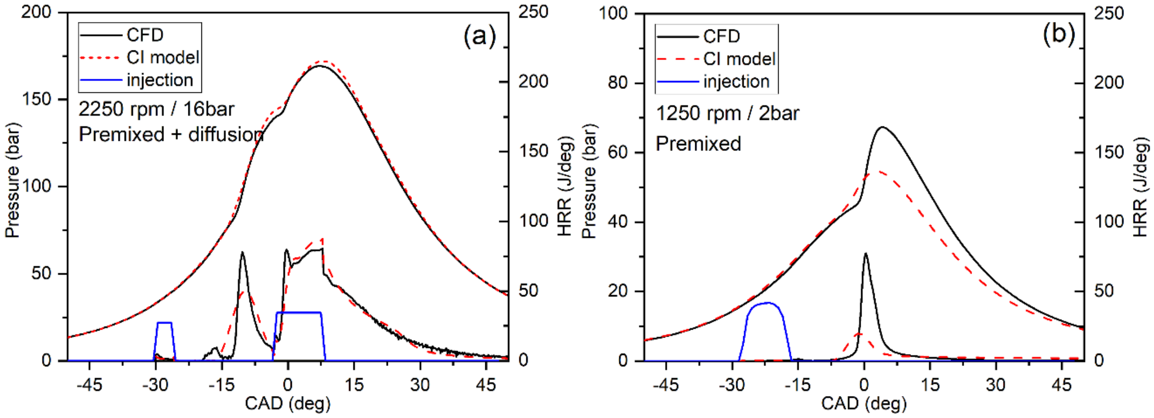

Figure 2 In-cylinder pressure and burn rate comparisons between CFD results and the current CI model available in GT-Power.

1.3 Brief Description of The Platform Used in This Study

In this study, GT-Suite and ConvergeCFD were utilized to conduct numerical simulations and to develop a combustion model. GT-Suite is a widely used system-level 0D/1D vehicle system simulation software which is capable of performing various engine simulations, including combustion, fuel injection strategies, and LP/HP EGR systems. GT-Suite also offers various aftertreatment models like TWC, DOC, DPF, and SCR, as well as vehicle models to estimate the tailpipe emissions on standard driving cycles. Figure 3 shows an example model of a complete vehicle system, including engine, driver, vehicle, and aftertreatment. In the engine sub-model, either a predicted or map-based model can be used, and the vehicle model calculates the dynamics of the vehicle on the given driving cycle. A driver sub-model provides accelerator and brake input based on the driving cycle. As shown in Figure 4, the aftertreatment system models include DOC, DPF, SCR, and so on, depending on the needs. The major species is extracted from the engine exhaust pipe and fed into each component of the aftertreatment system in sequence. For each component, a chemical reaction mechanism is needed to predict downstream tailpipe emissions accurately.

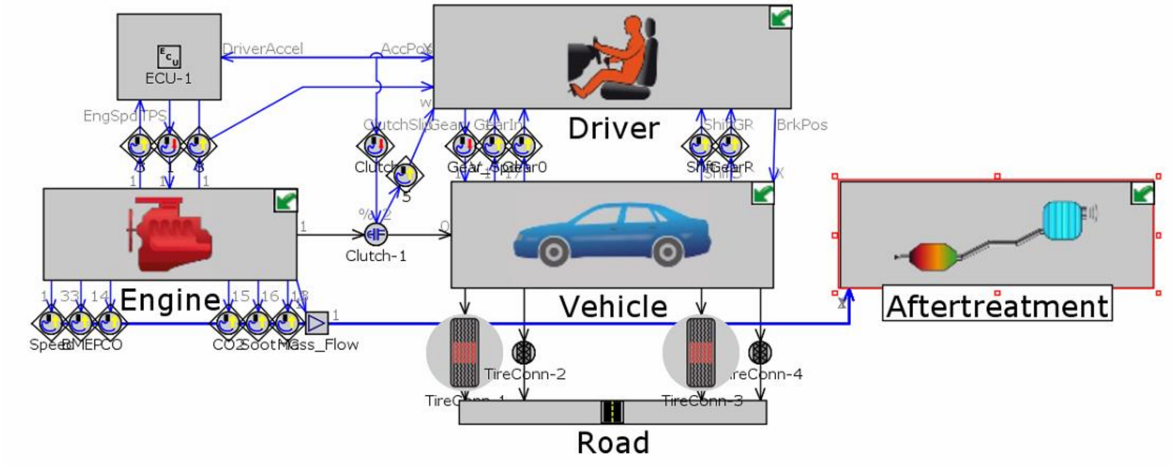

Figure 3 An example of GT-Power vehicle simulation configuration.

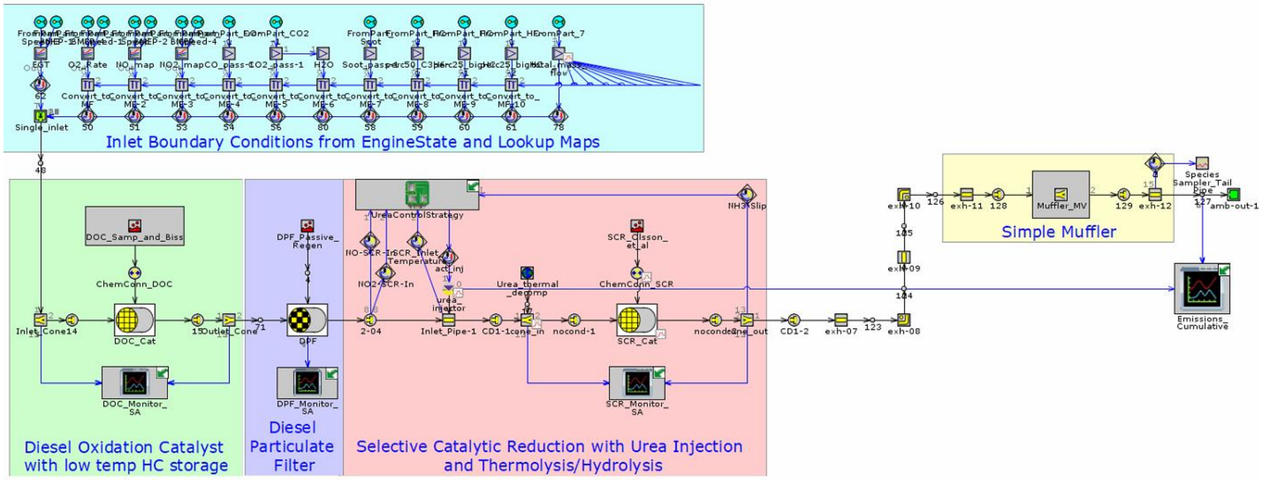

Figure 4 An example of an aftertreatment system for diesel engine system: DOC, DPF, and SCR.

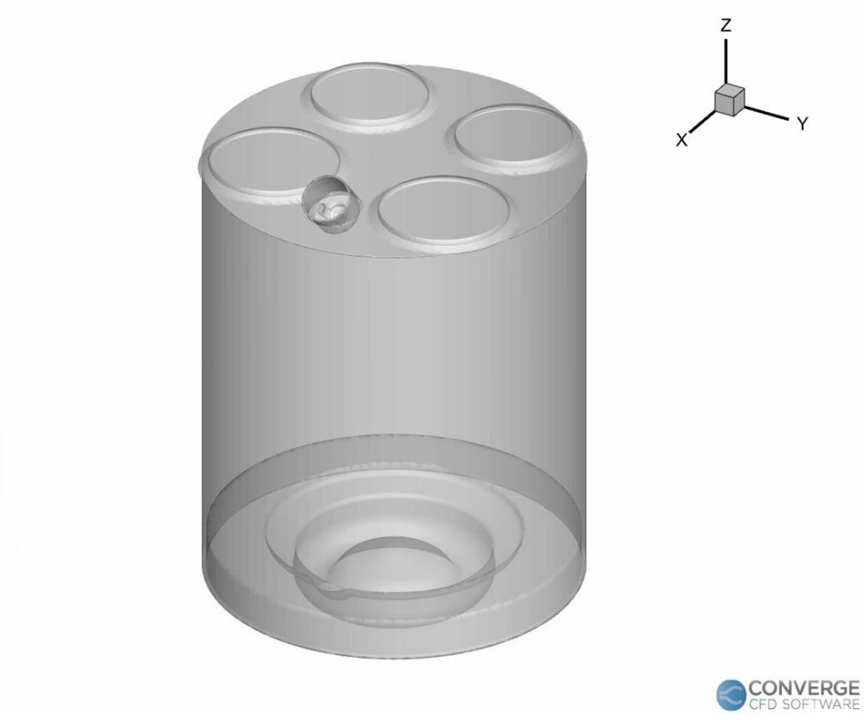

Figure 5 The cylinder CAD model used in CFD closed-cycle analysis.

Three-dimensional (3D) CFD tool has been widely used to simulate the combustion process and formation of pollutants and essential radicals. ConvergeCFD is one of the high-fidelity professional CFD tools specialized in combustion analysis using 3D CAD models, as shown in

Figure 5. It can simulate the details of turbulence flow, chemical reactions of the fuel, and the formation of pollutants within numerous mesh structures. It also includes models of fuel injection spray, break-up, and evaporation. However, despite its superiority, there is a drawback: it takes considerable time to conduct even one cycle. Therefore, running transient system simulation cases using 3D tools is nearly impossible. In addition, the 3D CFD model requires prior knowledge of the application to construct boundary conditions such as wall temperatures and composition for a combustion model to accurately evaluate the performance, formation of pollutants, and engine-out emissions.

1.4 Objective of Study

This study aimed to develop a combustion model for premixed and diffusion combustion strategy, which can be used to capture the combustion characteristics of GCI combustion. As such, the sub-models for fuel spray dynamics, ignition delay, and combustion heat release rate were developed. The models developed were integrated into a commercially available tool, GT-Suite, capable of analyzing a system-level engine with various sub-systems such as air handling, EGR, and after-treatment systems. To facilitate the development and validation of the combustion model, a CFD simulation using the ConvergeCFD platform was also carried out to capture the phenomena of the fuel spray, distribution, and combustion characteristics. This approach ensured the fidelity of the model with accuracy to some extent but with less computational time. This model can be applied to simulate and evaluate the combustion process and exhaust emissions from an internal combustion engine during its development stage. A numerical GCI combustion model will enable a GCI engine with an aftertreatment system to minimize tailpipe emissions and fuel consumption to be modeled, utilizing a system-level 0/1D simulation tool.

The objectives of this study are summarized as follows:

1. Analyze and identify the characteristics of PPCI-mixing controlled diffusion combustion in GCI engine using CFD tool after validation against engine testing results.
2. Identify and understand high-pressure fuel injection dynamics and air entrainment behavior using the CFD tool.
3. Improve a spray model which captures the important behavior of fuel spray selected engine operating conditions.
4. Develop and adopt the ignition delay model by directly solving the chemical kinetics using a multizone approach for partially premixed compression ignition combustion.
5. Improve and modify of a conventional quasi-dimensional phenomenological CI model with the improved spray model.
6. Validate of the developed model with different operating conditions against PPCI-diffusion CFD results.
7. Implement the PPCI-mixing controlled combustion model into a system-level simulation tool, GT-Suite, and investigation on effects of VVA on GCI combustion.

Chapter 2. Literature Reviews

2.1 Auto-Ignition Behavior

Auto-Ignition can be defined as the ignition of an air-fuel mixture due to the exothermic reaction under escalated thermal conditions without any external ignition source such as a spark. HCCI is one of the combustion types based on the auto-ignition process, and it can be realized by various fuel types. Several studies investigated the characteristics of PRF in HCCI combustion with different blending ratios of n-heptane, representing diesel-like fuel and iso-octane, representing gasoline-like fuel. Figure 6 shows the different auto-ignition behaviors of two PRF blends. PRF80 is a mixture of 80 % iso-octane and 20% n-heptane. It is known that lower octane fuel, like n-heptane, reveals two-stage ignition, while higher octane fuel exhibits single-stage ignition, as shown in Figure 6. In the case of PRF80, the ignition is divided into two regimes by a small NTC period. The first small heat release, known as low-temperature combustion or cool flame at 760 - 880 K, started at 340 degrees in the figure, and the time delay called NTC will be exhibited. The ignition process rate then gradually increases during ITHR, and main heat release will occur rapidly.

On the contrary, single-stage ignition by iso-octane does not show early heat release, unlike PRF80, but it slowly starts the ignition process. Once the favorable thermal condition is met at about 950-1050 K, the heat release rate increases. It can be concluded that two-stage ignition fuel requires lower thermal energy than single-state ignition due to the heat release during LTHR.

It is well documented that the pathways of combustion of hydrocarbon fuels are comprised of multiple chemical reactions: initiation, propagation, branching, and termination. The initiation step refers to the breakdown of the species into unstable radicals. Propagation is where the radicals

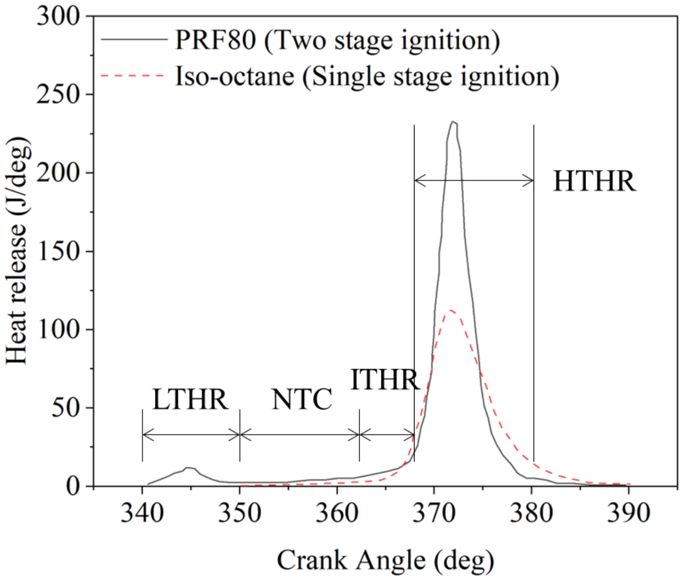

Figure 6 Auto-ignition heat release traces for PRF80 (two-stage ignition) and iso-octane (single-stage ignition) [16].

bring about other radicals, called chain propagation reactions, resulting in rapid heat release. Once all the reactants are consumed, the radicals combine with other radicals and terminate reactions [17]. Some of the important reactions are summarized at the end of this section.

As temperature increases by the piston movement towards the Top Dead Center (TDC), the first initial chemical reaction will generate small amounts of radicals, which abstract hydrogen atoms from fuel molecules at a temperature below 850 K. This will result in alkyl radicals (R·) by reaction R1 [18]. Different structures of paraffin lead to different types of alky radicals by hydrogen abstraction, and there are two possible pathways of alky radical consumption (R2) and (R3) reactions.

A conjugate olefin and hydroperoxy radical can be generated by the R2 reaction, or alternatively, alkyl peroxy radical (RO2·) can be produced by R3. The R3 is an essential reaction to account for the HCCI auto-ignition process. The forward and backward reaction rates are different due to the activation energy required for the reactions, and the backward reaction is faster at high temperatures. Consequently, the concentration of the alkyl peroxy radical (RO2·) decreases and causes the termination of the chain branching reaction. This is responsible for the NTC regime in the auto-ignition of HCCI with two-stage heat release fuels. Alkyl peroxy radical (RO2·) is then transferred into ·QOOH by oxygen abstraction from the C-H bond and oxygen molecule.

The reaction of ·QOOH has two paths, depending on its structure. 1) ·QOOH generates OH· during decomposition into a lower molecular weight alkene or forming a cyclic ether (R5). 2) ·QOOH undergoes oxygen addition and forms hydroperoxyalkylperoxy radical ($\cdot O_2QOOH$) (R6), internal hydrogen atom abstraction to form alkyl hydroperoxide (R7a), which is converted to an aldehyde and two OH· radicals (R7b). It is observed that R3 and R6 reactions are the most affecting mechanisms on LTC.

During the ITHR regime, the increases in temperature in a cylinder promote the generation of more HO2 radicals (R2), and HO_2 forms H_2O_2 by abstracting hydrogen atoms from fuel (R8). An additional increase in gas temperature results in further decomposition of the H_2O_2 into hydroxyl radicals (OH·) by reaction (R9), which accelerates the overall reaction rates. Consequently, the increased reaction rates lead to a higher temperature, thus causing the rapid decomposition of H_2O_2.

For the HTHR regime, the high temperature oxidation of the fuel can be described by three steps, as presented in (R10). The fuel is converted into lower hydrocarbons, and the intermediate species transforms into CO and H_2O. Then, CO is oxidized to CO_2, releasing a significant fraction of energy. (R11) ~ (R13) describe the critical reaction in a high-temperature regime, and OH, H, and O radicals are the carrying radicals in reactions, and they are highly reactive. As a result, the fuel oxidation process becomes extremely fast and releases rapid heat energy. The final step of the heat release can be described by the reactions (R14), (R15), and (R16). It is known that (R14) is the main pathway of CO oxidation. The reactions involved are listed as the following [19].

$$RH + OH\cdot \rightarrow R\cdot + H_2O \tag{R1}$$

$$R\cdot + O_2 \rightarrow \text{olefin} + HO_2\cdot \tag{R2}$$

$$R\cdot + O_2 \leftrightarrow RO_2\cdot \tag{R3}$$

$$RO_2\cdot \rightarrow \cdot QOOH \tag{R4}$$

$$\cdot QOOH \rightarrow CARBONYL + R'\cdot + OH\cdot \tag{R5}$$

$$\cdot QOOH + O_2 \leftrightarrow \cdot O_2QOOH \tag{R6}$$

$$\cdot O_2QOOH \rightarrow HOOROOH \tag{R7a}$$

$$HOOROOH \rightarrow RCHO + R'O + OH\cdot + OH\cdot \tag{R7b}$$

$$RH + HO_2\cdot \leftrightarrow R\cdot + H_2O_2 \tag{R8}$$

$$H_2O_2 + M \rightarrow OH\cdot + OH\cdot + M \tag{R9}$$

$$RH + OH\cdot \rightarrow R`\cdot R`\cdot + H2O \rightarrow CO + H_2O \rightarrow CO_2 + Heat \tag{R10}$$

$$H\cdot + O_2 \rightarrow OH\cdot O\cdot \tag{R11}$$

$$O\cdot + H_2 \rightarrow OH\cdot + H\cdot \tag{R12}$$

$$H_2O + O\cdot \rightarrow OH\cdot + OH\cdot \tag{R13}$$

$$CO + OH\cdot \rightarrow CO_2 + H\cdot \tag{R14}$$

$$CO + HO_2\cdot \rightarrow CO_2 + OH\cdot \tag{R15}$$

$$CO + O\cdot + M \rightarrow CO_2 + M \tag{R16}$$

2.2 Low Temperature Combustion

Low-temperature combustion strategies have been of industrial interest, demonstrated, and showed their potential to satisfy current stringent standards on harmful emissions and fuel consumption by highly diluted and premixed air-fuel charge. Various LTC concepts have been proposed, and the combustion strategies can be categorized by charge preparation: homogeneous and stratified. HCCI ideally has a homogenous premixed lean air-fuel mixture, and the mixture is ignited simultaneously once the autoignition temperature is reached. Because the HCCI engine runs on the premixed and global lean mixture with high dilution, the combustion temperature is lower than that of traditional combustion, such as SI and CI combustion. Consequently, less thermal NOx is formed, benefiting from the lower combustion temperature. The lean premixed charge also deteriorates the formation of PM. Guo et al. and Li et al. numerically investigated the HCCI combustion and validated their models against experimental results [20, 21]. Guo et al. used a multi-zone approach to study HCCI combustion by dividing the combustion chamber into eight sub-zones. It was reported that the model predicted pressure trace relatively well in various engine speeds and air-fuel ratios. In this study, the fuel mass distribution was assumed to be a normal distribution. Li et al. conducted preliminary research on different conditions, such as engine speed, Air-Fuel ratio (AFR), and cylinder pressure. Mass distribution was assumed to be uniform in this study. Combustion characteristics such as phasing and pressure trace were well predicted, and combustion was advanced with a higher compression ratio and intake pressure.

Stratified charge compression ignition (SCCI) can also be subdivided by stratifications: thermal stratification and fuel stratification. Thermal stratification always exists but is usually dominated by the thermal condition within a cylinder, and it is not easy to have direct control over the temperature distribution in the cylinder in various conditions. One of the methods proposed to create thermal stratification is to inject water into a cylinder. The evaporation of the water directly injected into the cylinder cools down the temperature of the cylinder and develops temperature stratification. Lawler et al. [22] investigated the effects of water injection into a cylinder on heat release in HCCI. It was stated that the direct water injection created thermal stratification by the latent heat of water evaporation. The start of combustion was retarded, and the combustion phasing was also closely related to the amount of water injected. Also, the combustion duration was prolonged up to 146 % compared with the water-free operation case. Boldaji et al. [23] also conducted a similar CFD analysis study. The cooling effect from water evaporation was clearly shown visually in a temperature contour plot. The most advanced water injection timing in their study was -60 °CA after TDC to maximize the cooling effect, leading to the most thermal stratification. Also, two water injection pressures of 20 and 160 bar were compared. The higher water injection pressure showed pronounced effects on combustion control, such as the start and duration of combustion.

The fuel stratification strategy has been investigated in detail using various configurations due to the ease of the active ignition timing control, as shown in Figure 7. Fuel stratification was usually achieved through varying fuel injection strategies such as injection timing and multiple injections to create inhomogeneity within the cylinder. This strategy results in spatially different fuel concentrations. Based on the concentration, the autoignition occurs in order, preventing excessive heat release. Depending on their purposes, the fuel stratification-based combustions are referred to by different names.

As forementioned, gasoline PPCI can be sub-grouped by the degree of fuel stratification: PFS, MFS, and HFS. PFS uses the highest partial premixed charge, leading to the lowest fuel stratification, while HFS uses less, resulting in higher fuel stratification. In PFS mode, the first injection occurs during the intake stroke to create a premixed charge, and the rest of the fuel can be injected during the compression stroke to obtain the desired level of fuel stratification. The amount of premixed charge created by the early injection is limited by the acceptable MPRR; thus, PFS is usually employed for low-load conditions. However, incomplete combustion can be a problem if the premixed charge is overmixed toward a very lean homogeneous air-fuel mixture.

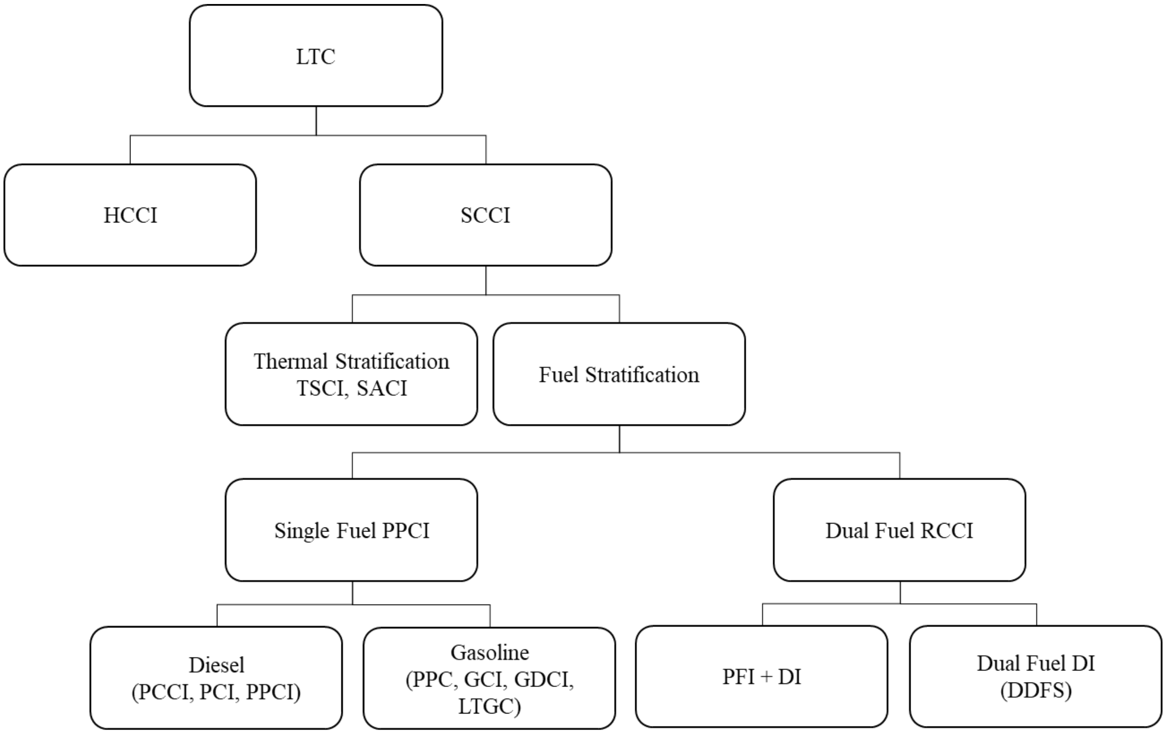

Figure 7 Various advanced combustion strategies in the LTC concept. [17]

In MFS, the amount of the premixed charge is relatively reduced compared to PFS, and the fuel injection takes place during the compression stroke. To initiate the combustion, the last injection (~15% of the total amount) occurs near the TDC [15]. In HFS mode, the fraction of premixed charge is small. All the injections occur during compression stroke near TDC, which usually operates at higher injection pressure so that the fuel injection process is completed before the start of ignition. The locally distributed fuel mixture resulting from the late direct injection can produce a high level of NOx; thus, a high level of EGR (~50 %) is usually required to mitigate the formation of excessive NOx and PRR.

Studies [24-27] showed that using various injection strategies, PCCI combustion achieved lower NOx and PM emissions than conventional diesel combustion. Nevertheless, they revealed the limitation that PCCI was not achieved in high load conditions as ignition delay became shorter, and a high level of EGR up to 70% was required to mitigate the rapid heat release.

Manente et al. [28] investigated numerous fuels, including gasoline, ethanol, and diesel. Gasoline partial premixed combustion achieved about 4 % improvement in fuel consumption with lower NOx and soot at 16 bar brake mean effective pressure (BMEP) under high load operating conditions. Delphi [29-34] developed and assessed the performance of gasoline direct injection compression ignition (GDCI) from low to high load conditions. Numerous configurations and strategies with different reactivity fuels were adopted to achieve stable combustion and reduce emissions and fuel consumption. For example, 43.5% of brake thermal efficiency was reported in recent research [35].

Similarly, the numerical and experimental studies [30, 36-39] conducted by Aramco demonstrated the advantages of the GCI engine. By adopting a double injection strategy, early pilot injection, and second injection near TDC, PPCI-diffusion combustion was realized. The pilot injection created the proper thermal condition before the main injection, and this strategy showed successful control over the combustion phasing and MPRR. Moreover, this PPCI-diffusion combustion strategy has shown encouraging results in various conditions. For example, a recent study [39] was carried out at full load condition (2000 rpm and 23.5 bar closed-cycle indicated mean effective pressure (IMEP), using 3D CFD analysis. Fuel injection parameters such as inclusion angle, nozzle hole, and total nozzle area were evaluated, tailored, and optimized for clean and efficient combustion. The optimized GCI results demonstrated a 5.1 % improvement in Indicated Specific Fuel Consumption (ISFC) and a 50 % drop in soot emissions compared to the conventional diesel engine operation.

2.3 Combustion Modeling Approaches

There have been many approaches and models to predict the performance of internal combustion engines by simulating thermodynamics, fluid flow, heat transfer, combustion process, and the formation of pollutants. Although thermodynamic combustion models (TCM) cannot provide as detailed information as CFD models, TCM can predict combustion with satisfactory accuracy. Moreover, the benefits of TCM, such as low computational cost, short running time, and capabilities under various operating conditions, are attractive to researchers, especially when high-performance computers are not available and affordable. For combustion modeling, which predicts and simulates the burning rate or chemical energy release rate, zone approaches have been successfully incorporated into engine modeling. Combustion modeling can be categorized into three groups: 1) zero-dimensional, 2) quasi-dimensional, and 3) multi-dimensional. A simple illustration is presented in Figure 8. Zero-dimensional combustion modeling is the simplest model among these models since it does not include the in-cylinder flow field. However, the accuracy and complexity of the model increase as more dimensions are considered. The zero-dimensional combustion model can further be divided depending on the number of zones, as shown in Figure 8. The simplest one is a single-zone model in which the combustion chamber is represented as a single homogeneous thermodynamic system. This single-zone model is often applied when a fast and preliminary analysis with an acceptable moderate level of accuracy is required. In a single-zone model, the in-cylinder charge is assumed to be homogenous. Because the combustion chamber is thought to be a single thermodynamic system, the averaged bulk gas temperature often results in a less accurate prediction of exhaust emissions. Based on the assumption, a system of three equations, energy conservation, ideal gas law, and mass conservation, are solved. Yıldız [40] compared the single and double Wiebe functions in simulating the combustion process of the methane-hydrogen mixture as fuel using a single-zone approach. It was shown that the double Wiebe function was able to achieve better prediction than the single Wiebe function because methane had a slower laminar flame speed than hydrogen. Awad et al. [41] predicted the combustion process of a diesel engine fueled by biodiesel using a single-zone model with a combustion process simulated using a triple Wiebe function. The maximum error in in-cylinder pressure prediction was 2.5%. Maroteaux et al. [42] developed and validated a single-zone diesel combustion model for hardware in-loop applications. Multi-mode Wiebe functions were used to represent the combustion process of a diesel engine with multiple injections [43]. The combustion parameters were calibrated using a regression model.

A two-zone model is a continuation of the single-zone model and a widely accepted approach for SI internal combustion engine modeling. Two zone approach divides the combustion chamber into two zones by a thin flame front: unburned and burned zones. Each zone has its thermal characteristics, such as temperature and bulk gas composition, but pressures for both zones are the same. Before the ignition, all the contents, including air-fuel mixture, residual gas, and EGR, are uniformly mixed within the unburned zone. When ignition occurs, some air-fuel mixture starts to burn, and the combustion products are considered the burned zone. The rate of heat release or fuel burn rate can be either predefined or predicted. One common way to approximate fuel burn rate in IC engines is to use a mathematical function such as the Wiebe function for its fast and low computational cost.

Direct injection compression ignition combustion, such as diesel fuel combustion, shows different phenomena from SI premixed combustion; thereby, the modeling approach is quite different. The two-zone model for SI combustion assumes that the air-fuel mixture in each zone is uniformly premixed and the combustion precedes by flame front. The diesel combustion model tracks fuels within small packets which contain fuel. Each packet is used to calculate air entrainment, fuel break-up, and evaporations. Figure 9 shows one of the CI combustion models, a

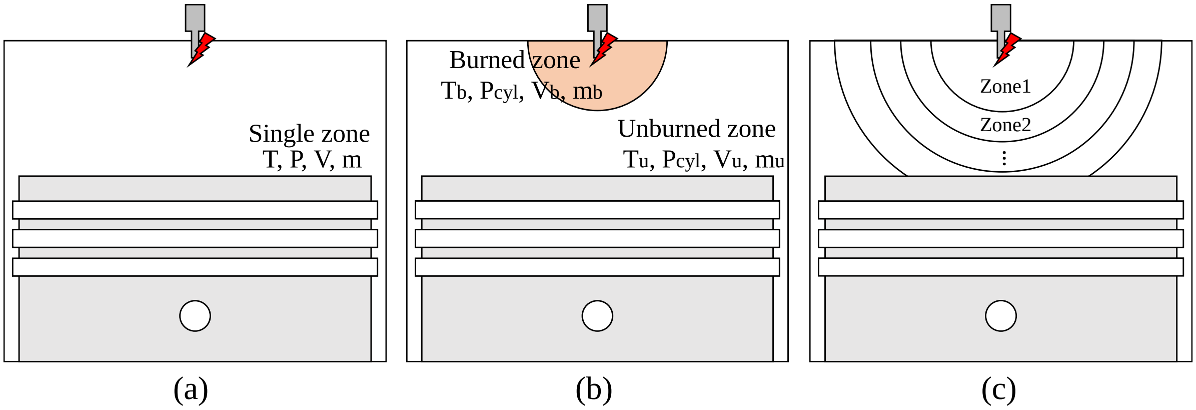

Figure 8 Combustion modeling approaches a) single zone, b) two-zone, and c) multi-zone model.

jet spray model. The fuel plume is divided into five radial zones and many axial zones, and each packet contains the same amount of fuel. As illustrated in Figure 9, the outer packet shows a shorter penetration due to slow velocity caused by air entrainment, and the center packet has the longest penetration. After the break-up, fuel evaporation is calculated based on Sauter Mean Diameter (SMD). The detailed air-fuel mixing process is presented in Figure 9 (b). At the end of the ignition delay period, the air-fuel mixture in each packet burns, which is defined as premixed combustion. The second combustion stage starts after the premixed combustion and is controlled by air entrainment or fuel evaporation. The fuel burn rate in premixed and diffusion combustions is predefined as follows.

$$\frac{dm}{dt} = gain * \emptyset * (3-\emptyset)^2 * p^{2.5} * e^{-\frac{4000}{T}} \qquad \text{Equation 2.1 [44]}$$

Where,

$\frac{dm}{dt}$ = Rate of combustion

Gain = Combustion rate multiplier

p = Pressure
T = Subzone Temperature
$\emptyset$ = Equivalence ratio

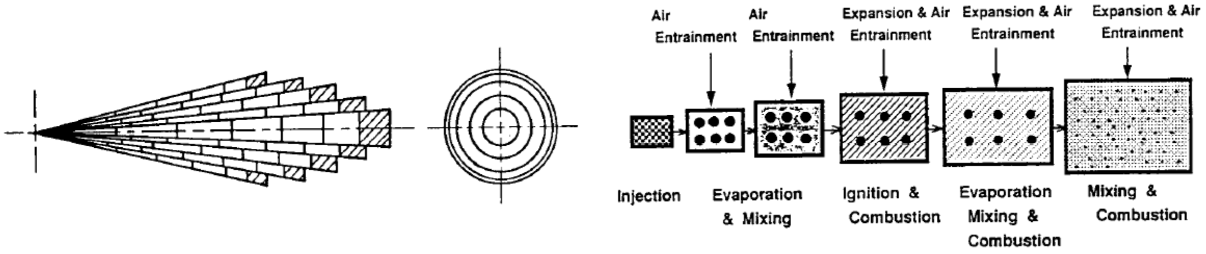

(a) (b)

Figure 9 a) Illustration of fuel injection in packets and b) air-fuel mixing process within a packet [45].

Jung et al. [46] developed a quasi-dimensional direct injection model based on Hiroyasu's work [47] for diesel spray combustion. Spray tip penetration correlation was modified based on experimental results, and at least five radial zones were recommended to predict NO and soot emissions accurately. Rakopoulos et al. [48] investigated the effects of EGR rate and temperature on diesel combustion over a wide range of injection timing. A two-zone approach was used to simulate the non-burning and burning zones, where fuel is entrained with the surrounding air. The model was calibrated with experimental data. The application of the cooled EGR was found to reduce cylinder pressure, temperature, NO emissions because the cold EGR lowered the mean gas temperature. However, the application of EGR deteriorated the thermal efficiency, but cold EGR showed lower drop (3.7 %) than hot EGR case (6.2 %). Li et al. [49] also utilized a chemical reaction based two-zone combustion model for SI engines. It was verified that the model was able to accurately predict the in-cylinder pressure, temperature, and heat release rate (HRR) with less than 6.2 % of maximum relative error in pressure prediction.

2.4 Multizone Combustion Model

In the multi-zone combustion approach, the in-cylinder volume is divided into several zones that have their own thermal conditions and compositions. Each zone is treated as a well-mixed reactor. One of the common approaches for the multi-zone model is to divide the entire combustion chamber by thermal stratification rather than the fuel distribution, as the HCCI assumes the homogeneity of fuel in the cylinder, and the fuel stratification is not significant. “Balloon-type” multi-zone configuration considers the zones deformable and fixed mass control volume. The heat and mass transfer between zones are usually ignored, yet the thermal stratification through the heat transfer to the walls is considered. “Onion-skin” multi-zone configuration divides the in-cylinder volume into concentric cylinder shapes [20, 50-52]. Much research is based on these configurations, and the difference is mainly the mass and heat transfer among zones [53].

2.5 1D/Phenomenological Spray Models.

Spray characteristics have been of interest to researchers over the decades due to their applicability across a wide range of industry machinery. Several aspects, such as the geometry of the nozzle, properties of the fuel, and spray dynamics, can be delineated by penetration length, dispersion angle, breakup, atomization, and the rate of injection, particularly within the context of internal combustion engine applications. The advent of a precise direct injection system, a common rail system in CI engines, is one of the key enablers in controlling the combustion process and its phasing for diesel engines to comply with emissions standards. As advanced combustion strategies often demand comprehensive optimization with precise injection events, tailored injection strategy, including injection timing, target, and multiple injections, is essential to achieve the desired local equivalence ratio, mixture formation, and lower emissions.

The complex phenomena of the spray can be simulated using a three-dimensional CFD analysis, and phenomenological models are the main approaches in engine simulation. CFD models are computationally expensive but provide a thorough analysis of both macroscopic and microscopic characteristics, such as droplet size and local equivalence ratio in temporal and spatial space. Phenomenological spray models are capable of predicting macroscopic behaviors to some degree with simplified physical processes and assumptions. In the thermodynamic combustion model, phenomenological models are widely employed due to the nature of the simpler combustion model.

There have been several studies on spray modeling with 1D, phenomenological multizone, and quasi-dimensional approaches, and they can be categorized into two: Lagrangian and Eulerian approaches. Some classical spray modeling research is introduced and summarized in [54] and [55].

Starting with the early spray models proposed and developed by Sass [56], Wakuri[57], and Dent[58] back in the 1920s and 70s, the modern spray jet model for diesel combustion was consolidated by Hiroyasu and Arai [59], based on Lagrangian approach. While other prior studies focused on spray development and penetration, Hiroyasu and Arai pointed out spray breakup and formulated semi-empirical correlations before and after the breakup period. This equation is widely adapted in both phenomenological models and CFD model. This spray jet model was further developed by Arai [59] and is widely used for combustion models. Naber and Siebers [60] modified the model [61] and considered a wide range of ambient conditions, mainly ambient gas density. Desantes et al. [62] made an assumption on the distribution of the fuel in the radial direction to calculate the spray penetration and velocity by correlating the momentum flux. All the works conducted by Hiroyasu and Arai, Naber and Siebers, and Desantes are based on the assumption that the injection rate is constant, which may not be realistic in engine applications.

Other researchers developed a spray model capable of predicting unstable initial spray evolution. Payri et al. [63] used a packet model to account for the momentum of the packets. When the momentum of the following packet penetrates the prior packets, the total momentum of both packets characterizes the combined packet until the following packet reaches the spray tip. Another spray model with Eulerian approach is a study from Musculus and co-workers [64]. The work by these researchers is an extension of the work from Naber and Siebers, and in this study, they discretized a conical shape spray zone, and the transient transport equation for mass and jet momentum was solved. It was stated that the rapid increase of air entrainment near the injector tip region at the end of injection was observed in experiments, and this air entrainment wave was focused and modeled. Other classical spray and improved spray models are well documented in reference [54].

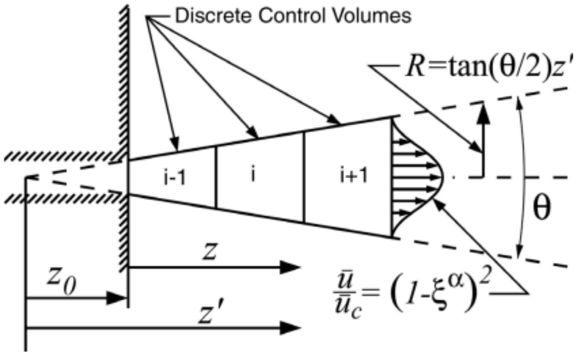

Figure 10 Schematic diagram of fuel injection model [65]

2.6 Limitation of the 0/1D combustion model

The existing 0/1D combustion models have been widely adapted in conventional SI and CI combustion engines due to their superior advantages in certain aspects over CFD analysis to predict and analyze the combustion process and engine systems. However, advanced combustion strategies such as premixed combustion for compression ignition engines have been proposed in the past decade, and the existing models cannot simulate the characteristics of new types of combustion accurately.

The conventional spray jet model proposed by Hiroyasu [47] is one of the widely used approaches based on the characteristics of high-pressure fuel spray. Although this model has been studied and improved by others, their research has focused on the dynamics of spray, such as penetration and velocity of the tip, and their validation against experiment results. Additionally, one of the assumptions made in the conventional spray model is that the injection pressure and velocity are constant throughout the injection period, which may not be actual in the real injection process. Therefore, it is essential to consider the rate of injection and fuel pressure while fuel is being introduced into a cylinder.

Secondly, the combustion mechanisms of the conventional CI combustion and the advanced partially premixed CI combustion are not identical. The conventional model cannot predict the premixed combustion by the first injection, featuring longer ignition delay during late compression stroke. CI combustion is characterized by two distinct combustion mechanisms: premixed combustion and mixing-controlled diffusion combustion. The premixed combustion process is initiated by the available fuel evaporated during the ignition delay, and the air-fuel mixture formed during the ignition delay starts to burn when the ignition delay ends. Highly reactive fuel, such as diesel fuel, shows a relatively short ignition delay, and the ignition starts before injection ends. One of the strategies controlling combustion phasing is to advance or retard injection timing. On the other hand, premixed combustion in advanced PPCI combustion is characterized by the prolonged ignition delay and mixing time, and the ignition is driven by chemical reactions. As a result, the thermal condition of the combustion chamber is essential, and the injection timing is not the only means for combustion phasing, unlike the CI combustion of conventional diesel engines.

Lastly, most of the early development stages in engine simulations heavily rely on CFD analysis. CFD is a high-fidelity analysis tool simulating various physical phenomena, such as turbulent flow and thermochemical reactions within highly discretized grids. However, its drawback, significant computational time, hinders the evaluation of the entire engine system. On top of that, considering the complexity of the recent engine systems comprised of many sub-systems such as EGR, turbocharger, variable valvetrain system, advanced fuel injection system, and aftertreatment system, the combustion optimization process often embraces extensive investigation of the interactions between each sub-system. Consequently, including these sub-systems to evaluate the entire engine system is critical.

Chapter 3. Simulation of GCI Combustion Using CFD

3.1 Gasoline Compression Ignition Engine

The GCI engine experiment was conducted at Aramco America, Novi, MI, and the engine was originally a four-cylinder 2.0 L diesel engine. The engine was modified accordingly for GCI combustion. The compression ratio of this engine was increased from 16 to 17 to promote the thermal condition necessary to initiate GCI combustion. Also, the swirl flap was removed to avoid extensive air-fuel mixing during prolonged ignition delay periods. The high-pressure common rail injection system was utilized with lubricant additives to prevent damage due to the lower viscosity of the gasoline fuel. The fuel used in this experiment was the pump E10 gasoline. Detailed information on the test engine is listed in Table 1. The GCI combustion was tested in the following operating conditions: 1) 2000 rpm 12 bar IMEP and 2) 2250 rpm 18 bar IMEP, which represent mid-load and high-efficiency operating conditions, respectively.

Table 1 Specification of the test engine in this study.

Engine speed [rpm]	2000 / 2250
Engine load [IMEP, bar]	12 / 18
Bore / Stroke [mm]	83 / 92
Connecting rod [mm]	142
Compression ratio	17
Displacement [Liter]	2
Number of valves	4
Number of injector nozzle holes	7
Nominal injector nozzle size [mm]	0.156
Intake valve opening timing @ 0.254mm [CAD]	360
Intake valve closing timing @ 0.254mm [CAD]	554
Exhaust valve opening timing @ 0.254mm [CAD]	154
Exhaust valve closing timing @ 0.254mm [CAD]	372

3.2 ConvergeCFD Model

A commercially available 3D CFD software, ConvergeCFD, was utilized in this study as a computational framework to simulate the fuel injection and combustion phenomena, such as fuel spray and distribution, within the cylinder. ConvergeCFD is a general-purpose tool to solve three-dimensional flow and chemical reactions with stationary and moving boundaries. Additionally, ConvergeCFD provides sub-models for turbulence, spray injection, droplet dynamics, and combustion. For turbulent flow modeling, the RNG $k - \varepsilon$ model [66] was utilized for combustion simulation. The RNG $k - \varepsilon$ model (Reynolds-Averaged Navier-Stokes $k - \varepsilon$) is the mostly used approach in CFD field to simulate the turbulence not only in I.C engines but also in other fluid flow applications. It is a two-equation model which describes the relationship between the turbulent viscosity and local turbulent kinetic energy k and dissipation ε [67]. As the name implies, the governing Navier-Stokes equations are averaged over time, and this model neglects small-scale and rapid turbulent motions. The turbulent kinetic energy, k, represents the energy associated with turbulence characteristics such as chaotic and vortex motion. The turbulent dissipation rate, ε, indicates how fast the turbulent kinetic energy is dissipated due to the internal viscosity forces of the fluid.

Accurate spray dynamics also need to be appropriately accounted for, and the blob injection method proposed by Reitz and Diwakar [68] was employed. This model introduces parcels, a group of droplets, into a cylinder to simulate an injector, and a parcel represents the droplets whose characteristics are identical, for example, the same size, velocity, and temperature. In this approach, the droplets equal the effective nozzle exit diameter. As the parcels enter the thermally elevated and dense ambient condition, they experience several physical processes: primary breakup, secondary breakup, evaporation, collision and coalescence. The primary breakup is the initial period of the breakup, where a continuous fuel stream breaks into larger droplets due to the interaction between jet and ambient gas. This gas-fuel interaction raises instability, called Rayleigh-Taylor (RT) instability, caused by the different properties of the two fluids, such as density, surface tension, and viscosity [69]. This instability results in the characteristic structure called fingers or spikes. This structure again enhances the mixing process. The secondary breakup follows the first breakup period, and the droplets further disintegrate into smaller ones. During this breakup, aerodynamic forces influence the droplet deformation, collision, and Kelvin-Helmholtz (KH) instability. KH instability is characterized by the wave-like patterns and resulted from the difference in the velocity of the fluid. This secondary breakup period creates a broader range of droplet distribution and enhances the mixing with the surrounding gas.

The computationally efficient model, the No Time Counter (NTC) method, was used to simulate droplet collision. In addition, drop drag and drop turbulent dispersion models are also used in this study. For droplet evaporation, the Frossling correlation was used, which estimates the change of drop size using the diffusivity, a mass transfer, and a Sherwood number [70-72].

The closed cycle combustion analysis, from intake valve closing (IVC) to exhaust valve opening (EVO), was conducted to minimize the computational time with reasonable accuracy. The full geometry of the combustion chamber was considered in this study. ConvergeCFD offers several combustion models, including a detailed chemistry solver and simplified combustion models for premixed and non-premixed combustion. SAGE detailed chemistry solver is the most predictive combustion model with the best accuracy among the models, and other combustion models such as Characteristic Time Combustion (CTC), shell ignition, and Representative Interactive Flamelet (RIF) are also available. The SAGE combustion model is adapted in this study. The available combustion models in ConvergeCFD are listed in Table 2.

Table 2 Combustion models available in ConvergeCFD.

Non-Premixed turbulent combustion models	Premixed turbulent combustion models
Characteristic Time Combustion (CTC)	Chemical Equilibrium (CEQ)
Shell Ignition	G-Equation
Chemical Equilibrium (CEQ)	Extended Coherent Flame Model (ECFM)
Representative Interactive Flamelet (RIF)	Flamelet Generated Manifold (FGM)
Extended Coherent Flame Model with the 3Zmixing model (ECFM3Z)	
Flamelet Generated Manifold (FGM)	

This SAGE solver calculates the chemical reaction rates at each cell based on the local conditions and the given chemistry reaction mechanism; thus, it requires detailed information such as the chemistry mechanism in Chemkin format for combustion and thermodynamic properties of species to solve chemical reactions. It would be ideal to use a large, detailed chemistry mechanism which consisted of hundreds of species and thousands of reactions for accurate results. However, it is practically impossible to employ such a large mechanism in a CFD model due to the computation resource limit. Therefore, a reduced gasoline surrogate, composed of toluene, n-heptane, iso-octane, and ethanol, mechanism from a study conducted by Li et al. [73], was employed to simulate combustion characteristics of E10 gasoline combustion. This reduced Toluene Primary Reference Fuel and Ethanol (TPRFE) chemical mechanism includes 59 species and 270 reactions and has been validated against experiments from various studies and showed good agreement in the oxygenated gasoline ignition delay and flame propagation speed under various dilution levels and equivalence ratio. The composition of the surrogate fuel to represent E10 gasoline in this study is listed in Table 3.

Table 3 Composition of TPRFE surrogate fuel used in this study.

Species	Mass fraction
C_2H_5OH	0.0868
$C_6H_5CH_3$	0.3202
C_8H_{18}	0.4094
C_7H_{16}	0.1836
Sum	1

Table 4 List of sub-models in ConvergeCFD case setup.

Spray model	
Injection	Blob
Evaporation / Collision	Frossling / NTC
Spray breakup	KH-RT
Combustion and emissions model	
Combustion solver	SAGE
Gas-Phase fuel surrogate	Reduced gasoline surrogate
Chemical kinetic mechanism	Li, et al. TPRFE mechanism [73]
NOx chemical mechanism	A reduced 4 species and 13 reactions [74]
Soot model	Hiroyasu-NSC
Turbulence	RNG $k - \varepsilon$
Wall heat transfer	O'Rourke & Amsden
Grid size	
Base grid	1.4 mm
Smallest grid	0.35 mm

The mesh size is one of the significant factors affecting the analysis's accuracy. 1.4 mm base grid size was chosen based on prior studies [22], and the adaptive mesh refinement (AMR) and fixed nozzle embedding features offered by ConvergeCFD were utilized, as shown in Figure 11, to increase the local resolution of the mesh grid at critical regions. A good compromise between accuracy and computational time can be achieved by adding an extra fine grid at critical and complex regions and keeping less critical regions with a relatively coarse grid. Based on prior research [22], 0.35mm mesh size by AMR showed a good balance between computational time and the fidelity of the predicted results, so 0.35 mm was selected for the model. A reduced NOx mechanism, consisting of 4 species and 13 reactions by [30, 31], was also implemented to predict NOx.

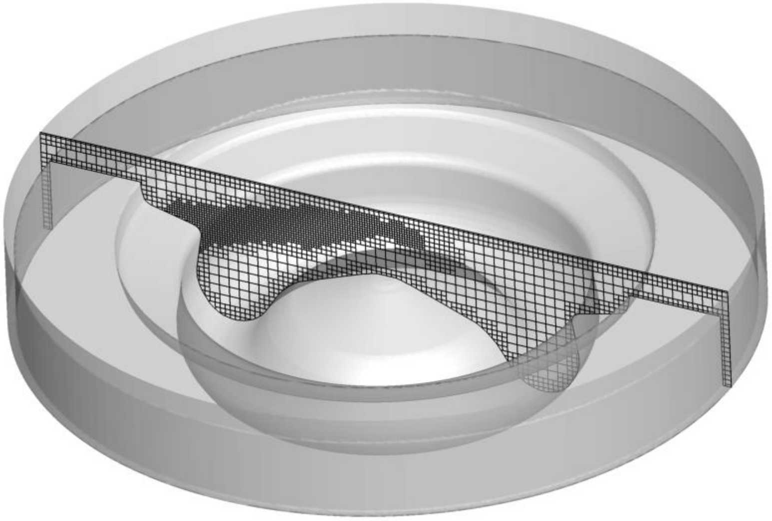

Figure 11 CFD mesh setup with the adapted mesh refinement.

It should be stated that some parameters were adjusted accordingly due to the uncertainties during experiments. The temperature at IVC was adjusted to consider the heat transfer from the cylinder wall and the presence of residual gas in the cylinder. The fuel injection timing in the CFD model was adjusted by 1~3 ^{o}CA because there will be some dwell time between the injection pulse signal and the actual moment of a needle when the fuel is injected into the cylinder. Also, the cylinder has some internal residual burned gas fractions, but the internal residual gas was not considered in modeling to minimize uncertainties.

3.3 CFD Model Validation Against Experimental Data

In this study, the CFD model was validated against experimental data. Figure 12 compares the motoring in-cylinder pressure at 1500 rpm simulated by CFD with experiment data. Overall,

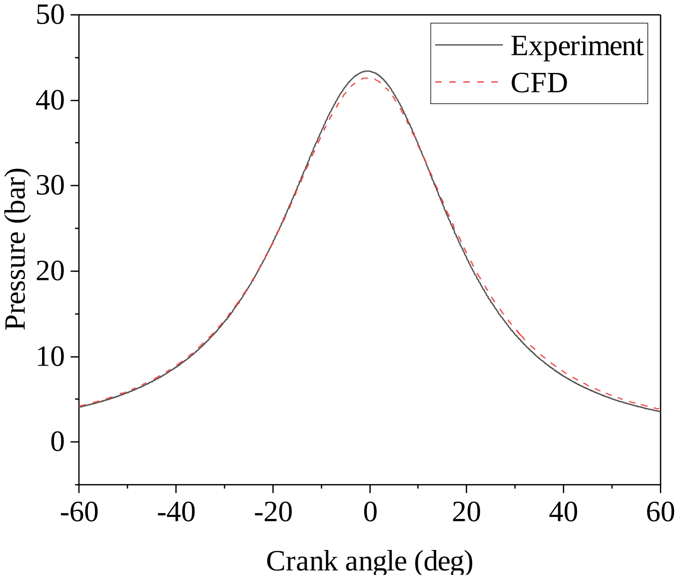

Figure 12 Motoring in-cylinder pressure comparison between experiment and CFD results.

the cylinder pressure simulated using CFD was consistent with experimental data, with a slight difference at the TDC. After motoring pressure was validated against experimental results, the simulated peak cylinder pressure, heat release process, combustion phasing represented by CA 10, CA 50, and CA 90, and engine-out emissions of CO and NOx simulated by ConvergeCFD were compared with experimental data.

Validation at 2000 rpm / 12 bar IMEP

The in-cylinder pressure and heat release are presented in Figure 13. The detailed operating conditions are listed in Table 5. The first fuel injection was at -23 °CA ATDC, followed by a clear separation between the end of injection and the start of ignition. This indicates that the lower reactivity of the gasoline has a prolonged ignition delay, which creates a partially premixed air-fuel mixture. The further movement of the piston towards TDC, thermally promoted condition of the cylinder initiated the chemical reaction of the fuel, resulting in a single-stage autoignition. As described in the previous chapter, the fuel oxidation was initially slow during ITHR, and after reaching the self-sustainable point, a rapid temperature increase representing the HTHR was observed. This is a typical premixed combustion process of gasoline-like fuels featured with lower reactivity. The chemical reaction of the mixture drives the combustion. The second injection occurred after TDC, followed by the mixing-controlled diffusion combustion represented by the second heat release process.

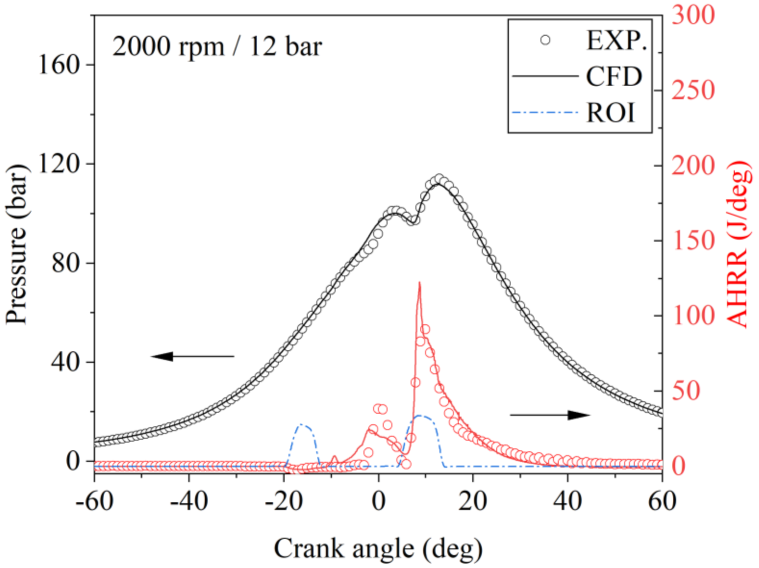

Figure 13 Comparison of the CFD simulated In-cylinder pressure and heat release rate with experimental data at 2000 rpm and 12 bar IMEP.

Table 5 Engine test operating condition at 2000 rpm and 12 bar IMEP.

	Experiment	CFD
Engine speed [rpm]	2000	←
Engine load, IMEP [bar]	12	←
Intake manifold pressure [bar]	1.85	1.87 at TIVC
Intake manifold temperature [K]	333	360 at TIVC
Exhaust manifold pressure [bar]	2.27	←
Exhaust manifold temperature [K]	773	←
Injection pressure [bar]	1400	←
Injection timing [ºCA ATDC]	-23 / 1	-21 / 2
Split ratio	0.37 / 0.63	←
EGR rate [%]	20	←

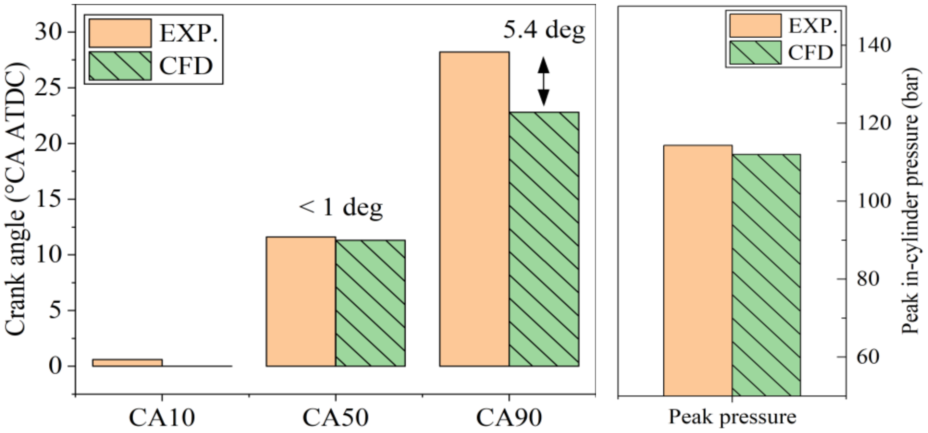

Figure 14 Comparison of CFD simulated combustion phasing and peak in-cylinder pressure with experimental data at 2000 rpm and 12 bar IMEP

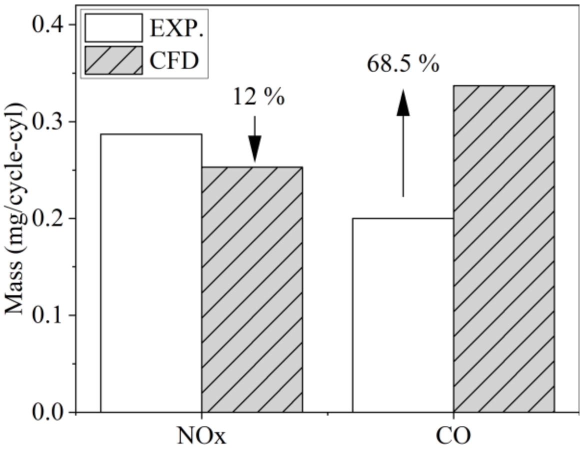

Figure 15 Comparison of CFD simulated engine out NOx and CO emissions with experimental data at 2000 rpm and 12 bar IMEP.

As shown in Figure 13, the CFD simulation results were found to agree reasonably well with experimental results despite the under-prediction at the premixed combustion period near TDC. In CFD simulation, the two-stage combustion with NTC region was observed due to the presence of about 18% n-heptane in the surrogate fuel used in CFD simulation. Figure 14 and Figure 15 present the combustion phasing (CA10, CA50, and CA90) and the engine-out NOx and CO emissions per cycle. CA10 and CA50 revealed less than a 1 ˚CA difference between CFD and test, and CA90 showed less than 6 ˚CA. The discrepancy in peak in-cylinder pressure was about 2 %. NOx (-12 %) and CO (+68.5 %) showed reasonable validation results even though CO was overestimated.

There are two pathways of CO formation in premixed combustion: 1) incomplete combustion due to the global lean air-fuel mixture and 2) lower combustion temperature at diluted conditions. CO cannot be oxidized to CO2 at lower gas temperatures, resulting in high CO emissions, as shown in Figure 16. The NOx generation rate also decreased as the main combustion ended, and gas temperature decreased due to the expansion cooling and heat loss from cylinder to coolant. Meanwhile, the rate of CO conversion to CO_2 also becomes weaker. The combustion phasing was well agreed during the early and middle development, indicated by CA10 and CA50, with marginal error in the CA90. However, the engine-out CO emission was overpredicted in the CFD simulation. It can be concluded that the early termination of heat release in CFD resulted in a shorter oxidation time of CO at the end of combustion. The combustion process and NOx emissions simulated using the CFD model generally agreed well with experimental data, but CFD simulation over-predicted CO emissions.

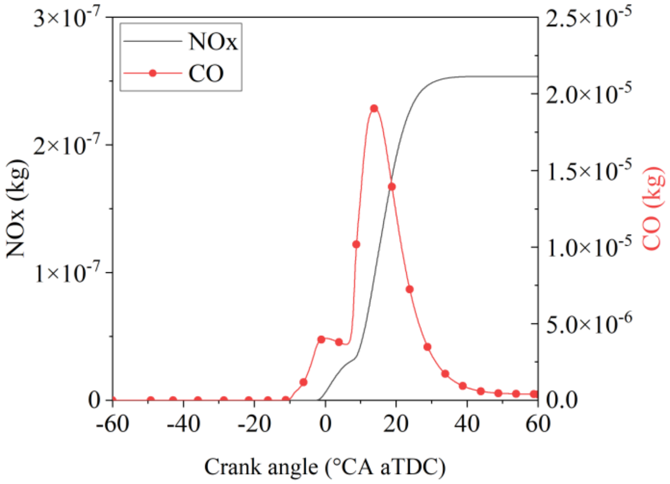

Figure 16 Variation of NOx and CO simulated using CFD at 2000 rpm / 12 bar IMEP.

Validation at 2250 rpm / 18 bar IMEP

Figure 17 compares the CFD simulated in-cylinder pressure and heat release rate with experimental data measured at 2250 rpm and 18 bar IMEP.

Table 6 presents the engine test operation condition. Overall, the CFD simulation results were found to agree well with experimental data. However, as previously discussed, CFD simulation underestimates partially premixed combustion, showing slower combustion with less peak heat release yet earlier ignition start. Figure 18 and Figure 19 present combustion phasing, NOx, and CO emissions from the experiment and CFD. The CA90 in CFD simulation was ~ 6 °CA earlier than the experiment result, but CA10 and CA50 exhibited comparable results (~2.5 deg). The discrepancy in peak in-cylinder pressure was about 1.5 %. NOx emissions were slightly underestimated (by ~21 %) due to the lower charge temperature; thus, CO was not effectively oxidized and overestimated by 200 % due to the shorter combustion and lower in-cylinder temperature, as shown in Figure 20. It can be concluded that NOx and CO generally reveal a trade-off relationship.

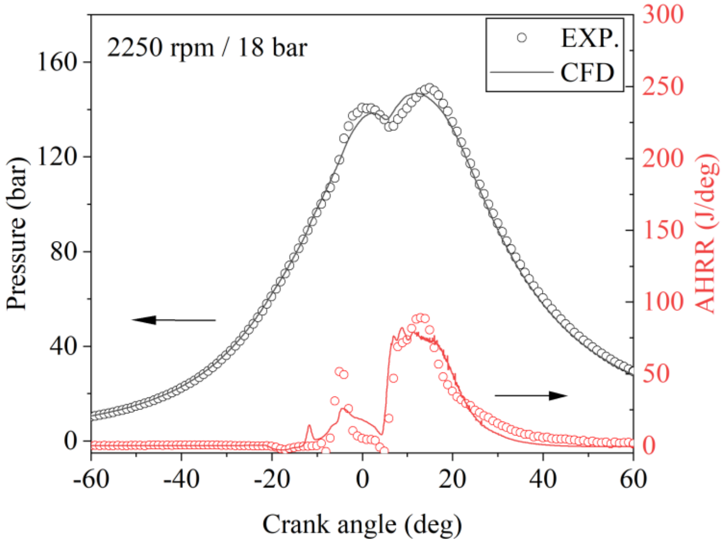

Figure 17 Comparison of the CFD simulated In-cylinder pressure and heat release rate with experimental data at 2250 rpm and 18 bar IMEP.

Table 6 Engine test operating condition at 2250 rpm and 18 bar IMEP.

Engine speed [rpm]	2250
Engine load, IMEP [bar]	18
Intake manifold pressure [bar]	2.67
Intake manifold temperature [K]	334
Exhaust manifold pressure [bar]	2.67
Exhaust manifold temperature [K]	828
Injection pressure [bar]	1600
Injection timing [ºCA ATDC]	-23 / 0
Split ratio	0.32 / 0.68
EGR ratio [%]	18.5

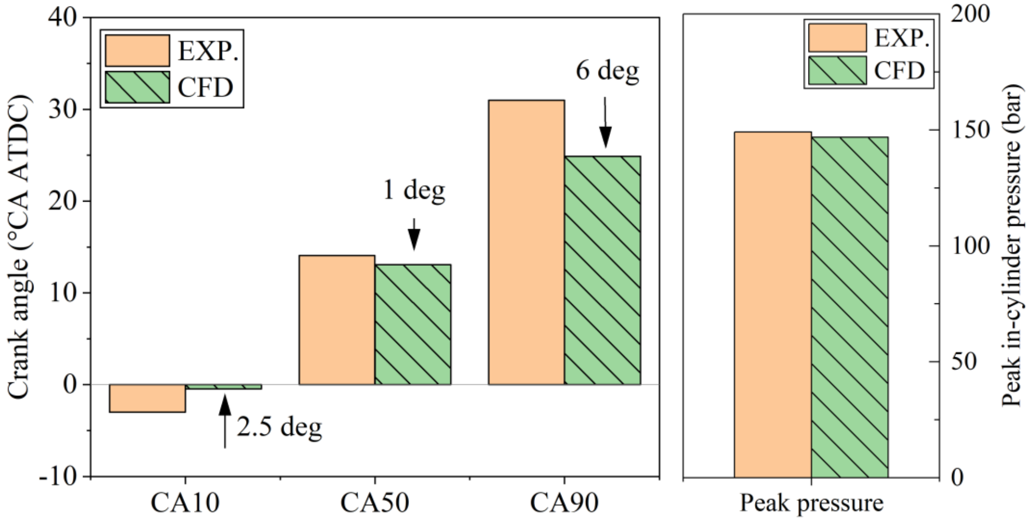

Figure 18 Comparison of CFD simulated combustion phasing and peak in-cylinder pressure with experimental data at 2250 rpm and 18 bar IMEP.

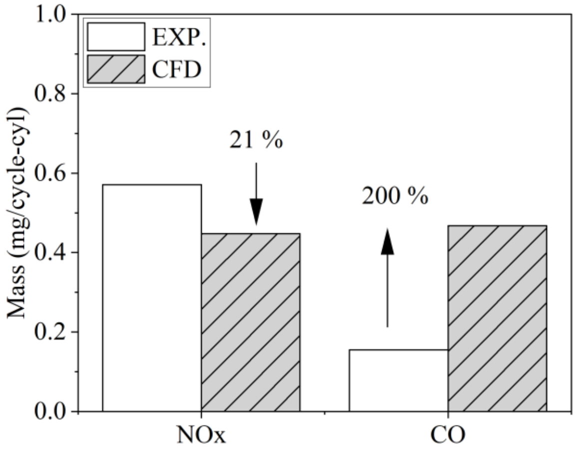

Figure 19 Comparison of the NOx and CO engine-out emissions from experiment and CFD simulation at 2250 rpm and 18 bar IMEP condition.

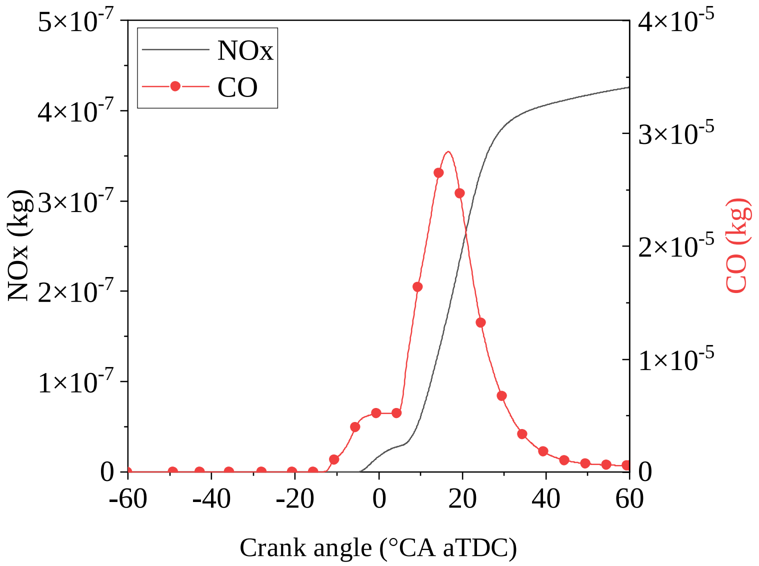

Figure 20 Variation of NOx and CO simulated using CFD at 2250 rpm / 18 bar IMEP.

3.4 Examination of Factors Affecting GCI Combustion Using CFD

Numerical model simulations often require extensive validation based on experiment results for their fidelity and accuracy. However, the GCI engine testing data available was very limited. Additional CFD simulations were conducted based on the available testing results for quasi-dimensional combustion model validation purposes. Although engine out exhaust emissions, usually measured at the exhaust pipe and tailpipe, are often made available through experiments, it is not straightforward to investigate the physical phenomena within the cylinder, such as spray and equivalence ratio distribution. In this research, more CFD simulations were conducted to examine combustion performance under various thermal boundary conditions relevant to engine operating conditions necessary for engine model development and system optimization.

Effect of the Temperatures at IVC on Combustion and Emissions

In this study, the effects of the bulk gas temperature at IVC (TIVC) on the combustion process were numerically investigated using the ConvergeCFD tool. The detailed operating conditions are listed in Table 7. With fixed pressure at IVC, the temperature was varied from 360 K to 400 K, which represented the elevated thermal boundary conditions. Various temperatures can be realized by various strategies, such as an electrical heater and VVA. For low-load conditions, a fixed 8 mg of TPRF-E fuel was injected into the cylinder by a single injection strategy at 200 bar. The injection timing was set at -28 °CA ATDC to create a locally stoichiometric air-fuel mixture. The initial composition of gases in the cylinder was made available through 1D system analysis, which represents 30 % EGR of the dilution level within the cylinder.

Table 7 Operating condition and species composition employed in this simulation.

Operating condition parameters	
Engine speed [rpm]	1250
Engine load, IMEP [bar]	3
Pressure at IVC [bar]	1.05
Temperature at IVC [K]	360 / 380 / 400
Injection pressure [bar]	200
Injection timing [°CA ATDC]	-28
Injection quantity [mg]	8
Initial in-cylinder gas species composition	
O_2	0.2089
CO_2	0.0211
H_2O	0.0082
N_2	0.7618

The overall GCI combustion at 1250 rpm 3 bar IMEP condition was plotted in Figure 21. The ignition delay period from the end of injection to the onset of ignition was observed, indicating partial premixed combustion. As expected, the higher temperature revealed a shorter ignition delay, indicated by CA10, and a rapid combustion process, indicated by CA90 - CA10. This is because the auto-ignition process was kinetically controlled, and the higher thermal energy in the cylinder led to faster chemical reactions. However, when the TIVC was 360 K, the auto-ignition process was not very efficient, as represented by the high CO and HC emissions, which were indicators of incomplete combustion.

The auto-ignition process can be represented by the formation of hydrogen peroxide (H_2O_2) and its decomposition to hydroxyl (OH) radical. At an intermediate temperature regime (>850K), the H_2O_2 formation significantly increases, and H_2O_2 decomposes into OH when the temperature reaches above 1000 K. As shown in Figure 21, the intermediate temperature heat release (-15 ~ -10 °CA ATDC) in the TIVC 400 K case was not pronounced compared with other cases, resulting in a lower level of H_2O_2, as shown in Figure 22. This could be due to the higher in-cylinder temperature, which promoted the high-temperature heat release regime due to the faster kinetics reaction. On the other hand, H_2O_2 in the 360 K case showed the highest level among the three cases, indicating that the lower and intermediate heat releases were very active. The low and intermediate heat release observed at 360 K TIVC was more significant than the other cases, as shown in Figure 21.

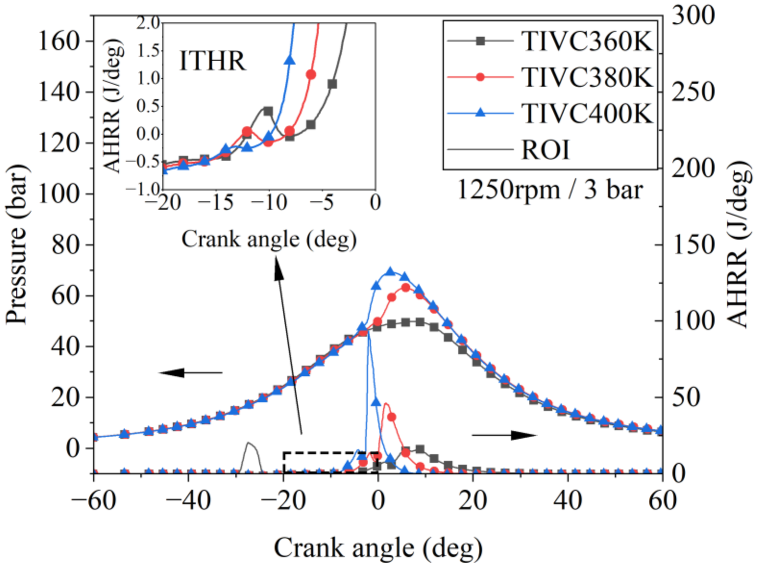

Figure 21 Effect of intake temperature on GCI combustion at 1250 rpm 3 bar IMEP.

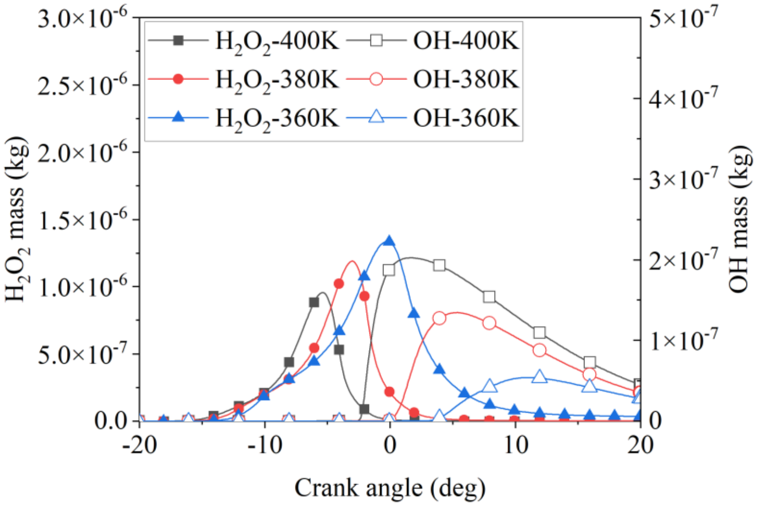

Figure 22 Mass species of H_2O_2 and OH as a function of CAD in 360, 380, and 400 K cases.

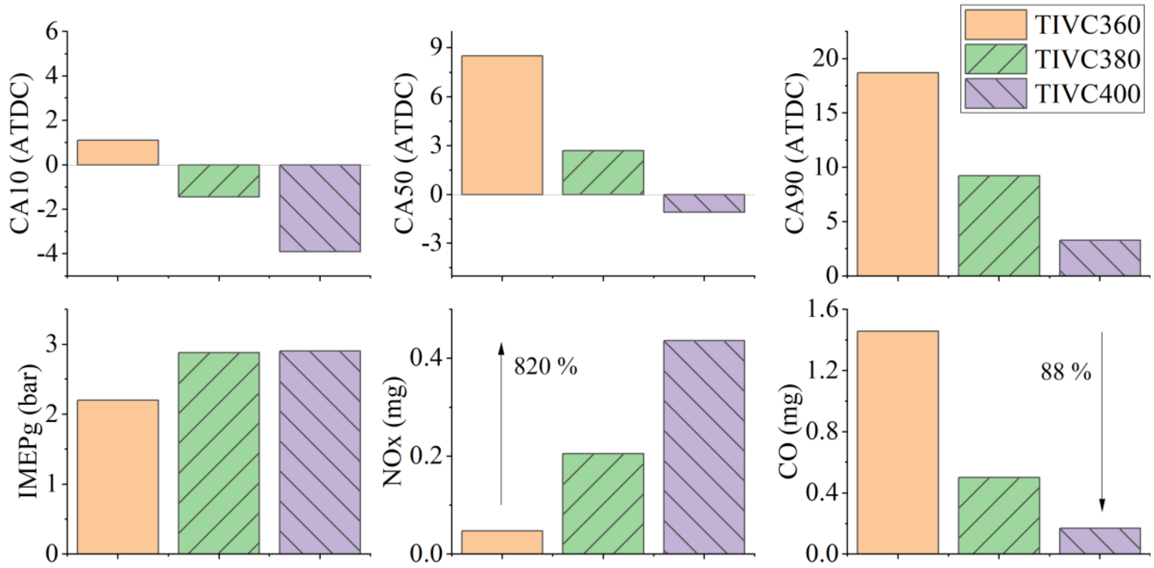

Figure 23 Effect of TIVC on combustion phasing, IMEP, and engine out CO and NOx emissions at 1250 rpm 3 bar IMEP.

When the in-cylinder temperature further increases, the H_2O_2 breaks down into OH radicals (above 1000 K), and the species mass of OH is shown in Figure 22. The highest OH was observed at 400 K, even though H_2O_2 was not the highest level. This reveals that the conversion rate of H_2O_2 into OH at high temperatures is considerably high. The formation of OH radicals promoted chain reactions, and this decomposition produced a significant amount of heat release, leading to the accelerated decomposition of H_2O_2 again and rapid heat release. During the final stage of the high-temperature combustion process, the oxidation of CO to CO_2 consumes OH and produces more heat. The low temperature and the OH content in the cylinder in the 360 K case showed the highest CO emissions, as shown in Figure 23. It is evident that increasing TIVC increased NOx emissions but decreased CO emissions.

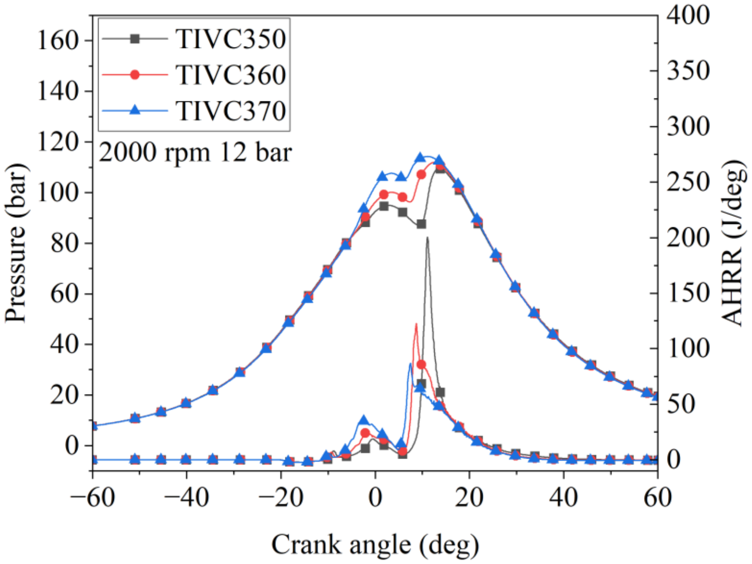

Figure 24 Effect of TIVC on cylinder pressure and apparent heat release rate at 2000 rpm, 12 bar IMEP, and 360 K TIVC.

The analogous observation was made for 2000 rpm, 12 bar IMEP and 2250 rpm, 18 bar IMEP. With thermally elevated conditions, the PPCI combustion showed faster and higher heat release, producing a considerable amount of combustion products. Nevertheless, the heat release from the diffusion combustion in the 370 K case exhibited a shorter ignition delay owing to the high temperature but lower peak heat release rate, as shown in Figure 24. For the 350 K case, it was shown that PPCI combustion was not very active, yet the second heat release peak from the second injection was observed due to the fuel left from 1st injection added to the premixed period of the second injection. This greater amount of fuel during the ignition delay causes abrupt auto ignition and spiky heat release. As indicated in CA10, CA50, and CA90 in Figure 25, the combustion was advanced when TIVC was increased. For example, increasing TIVC from 350 K to 370 K advanced the CA 50 from 12.5 to 10.4 °CA ATDC.

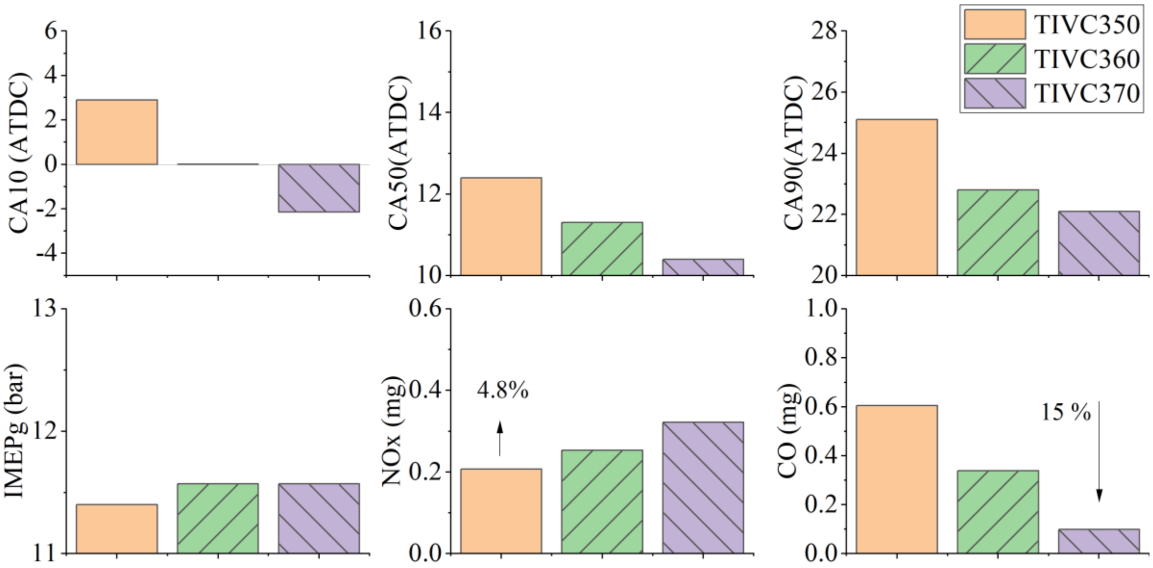

Figure 25 Effect of TIVC on combustion phasing, IMEP, and engine out CO and NOx emissions at 2000 rpm 12 bar IMEP.

Under the higher load condition at 2250 rpm / 18 bar IMEP, there was no significant difference between the three cases during diffusion combustion, meaning there was almost no premixed period of the diffusion combustion by the second injection. This also aligns with the same ignition delay. The heat release was controlled by the mixing phenomenon of the fuel spray and ambient gas available within the cylinder. The engine out NOx and CO emissions showed a trade-off relationship in Figure 27. The high temperature promotes the formation of NOx and oxidation of CO to CO_2, which reduces CO emissions. As expected, the combustion was also advanced as TIVC increased, as shown by CA10, 50, and 90.

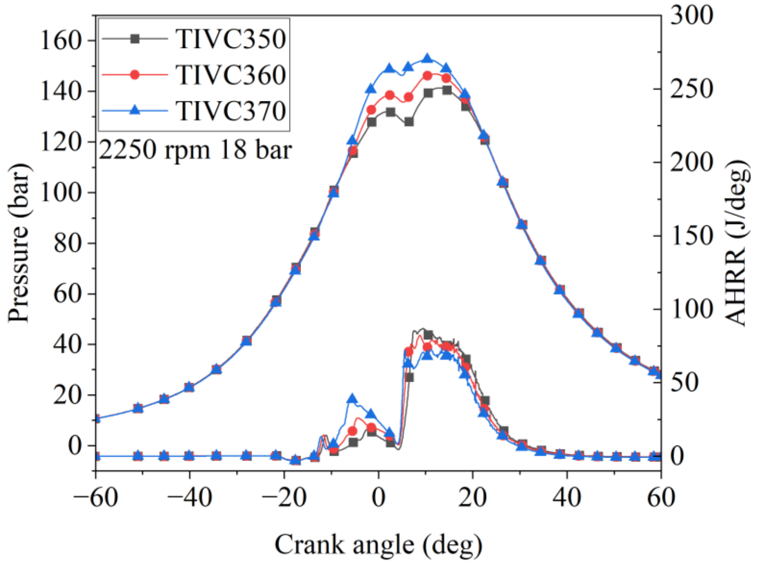

Figure 26 Effect of TIVC on in-cylinder pressure and apparent heat release process at 2250 rpm and 18 bar IMEP in CFD simulation.

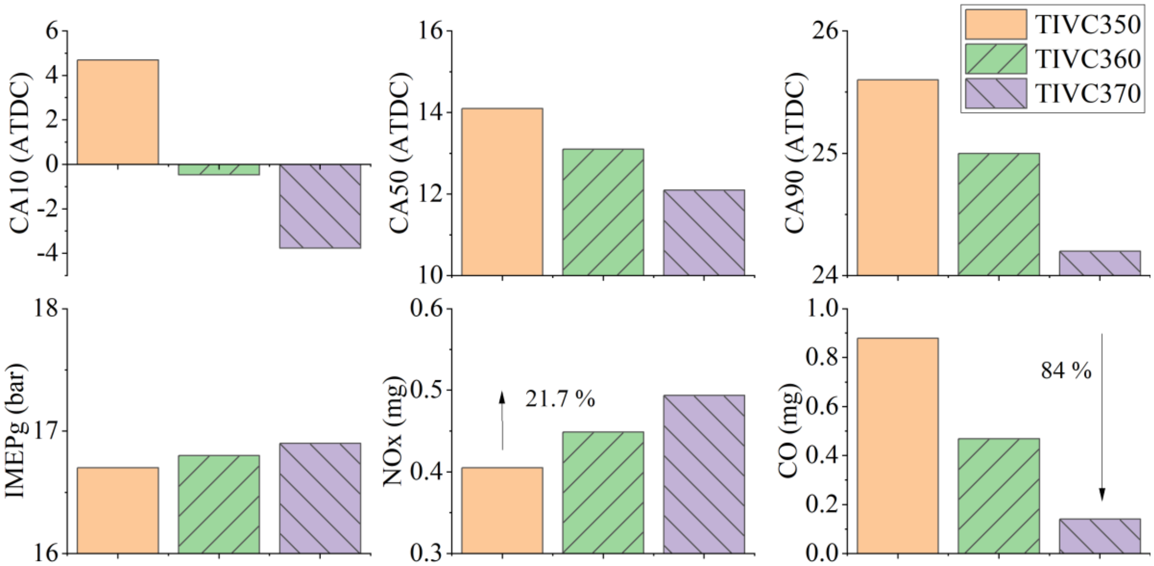

Figure 27 Effect of TIVC on combustion phasing, IMEP, and Engine out CO and NOx emissions at 2250 rpm 18 bar IMEP.

Effects of Intake Pressures on Combustion and Emissions

The effect of intake pressure at IVC (PIVC) on combustion and emissions was insignificant compared to the intake temperature effects, as shown in Figure 28 ~ Figure 31. Combustion phasing represented by CA10, 50, and 90 was generally advanced with higher PIVC due to the increased in-cylinder charge density, resulting in higher temperature during compression stroke. The change was less than 2 ˚CA in both 2000 rpm 12 bar IMEP and 2250 rpm 18 bar IMEP. The impact of intake pressure on the heat release rate was also relatively weak, as shown in Figure 28 and Figure 30.

The pressure at IVC also displayed a minor impact on engine-out NOx and CO emissions and IMEP across the cases, as shown in Figure 29 and Figure 31. It can be concluded that the pressure did not reveal considerable impacts on GCI combustion, but PIVC is generally modulated by a turbocharger, which has a significant impact on pumping losses.

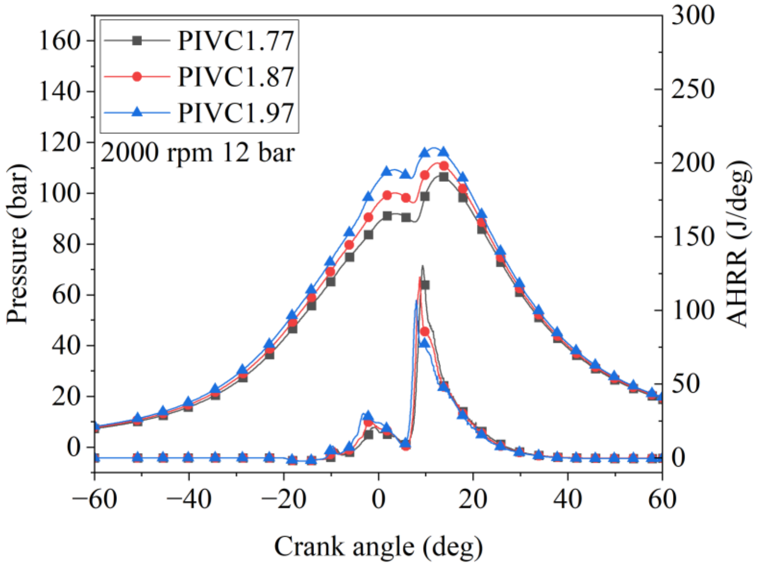

Figure 28 Effect of PIVC on in-cylinder pressure and apparent heat release process at 2000 rpm and 12 bar IMEP in CFD simulation.

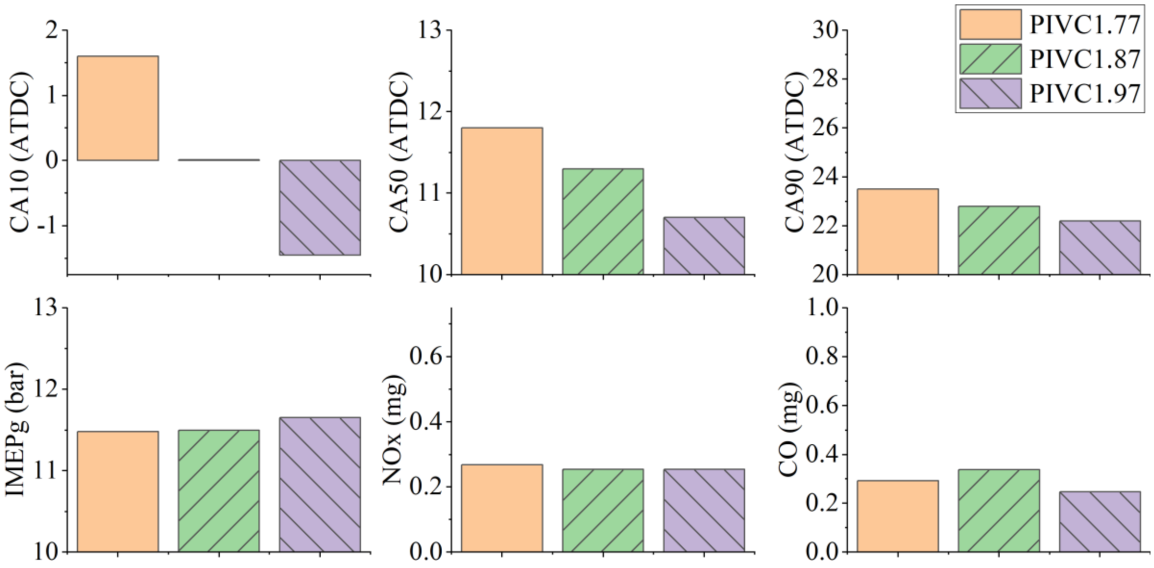

Figure 29 Effect of PIVC on IMEP, combustion phasing, engine out NOx and CO emissions at 2000 rpm 12 bar IMEP.

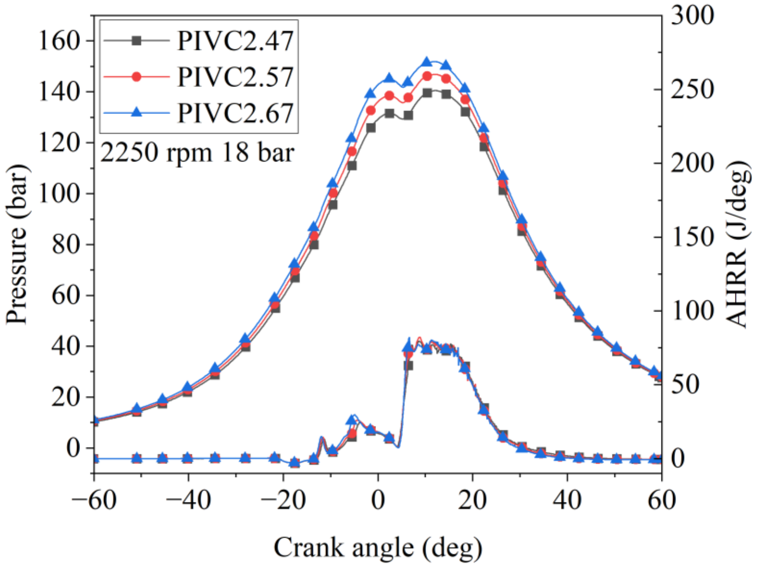

Figure 30 Effect of PIVC on in-cylinder pressure and apparent heat release process at 2250 rpm and 18 bar IMEP in CFD simulation.

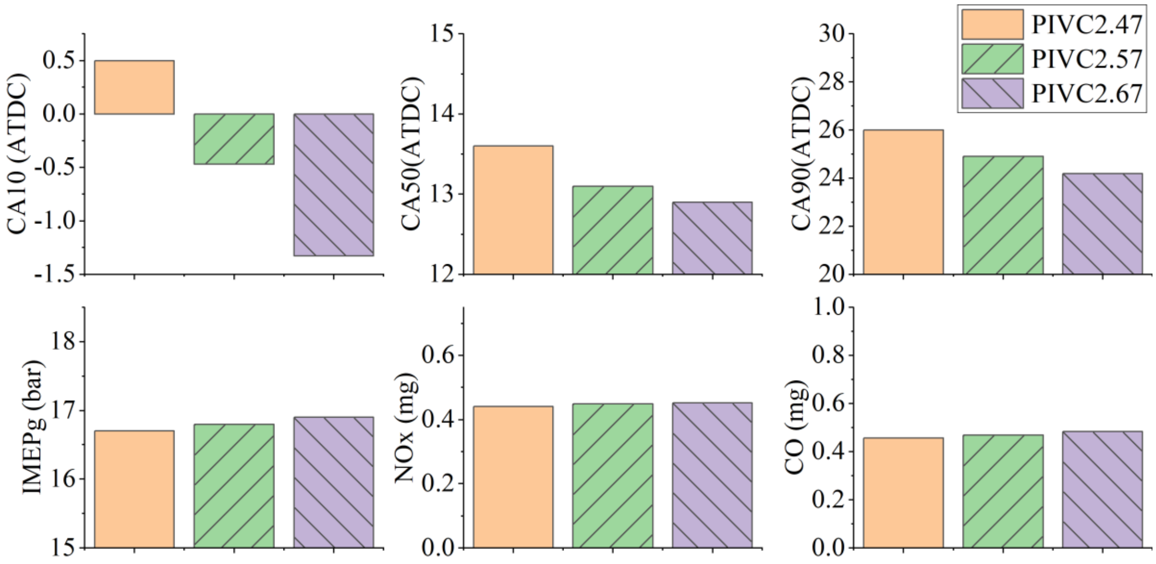

Figure 31 Effect of PIVC on IMEP, combustion phasing, engine out NOx and CO emissions at 2250 rpm and 18 bar IMEP.

Effect of EGR Rate on Combustion and Emissions

The effect of EGR on the combustion process and engine out NOx and CO emissions were numerically investigated at 1250 rpm, 3 bar IMEP, and 380 K TIVC. As shown in Figure 32, adding more EGR retarded the start of combustion and slightly reduced the peak heat release rate. As shown in Figure 33, adding more EGR retarded the formation of H_2O_2 and its decomposition to OH by about 2 ^{0}CA but had a very mild impact on maximum H_2O_2 and HO mass observed. This may be due to the fact that the TIVC was kept constant. This early production of H_2O_2 and its decomposition to OH contributed to the advanced and higher heat release during PPCI combustion.

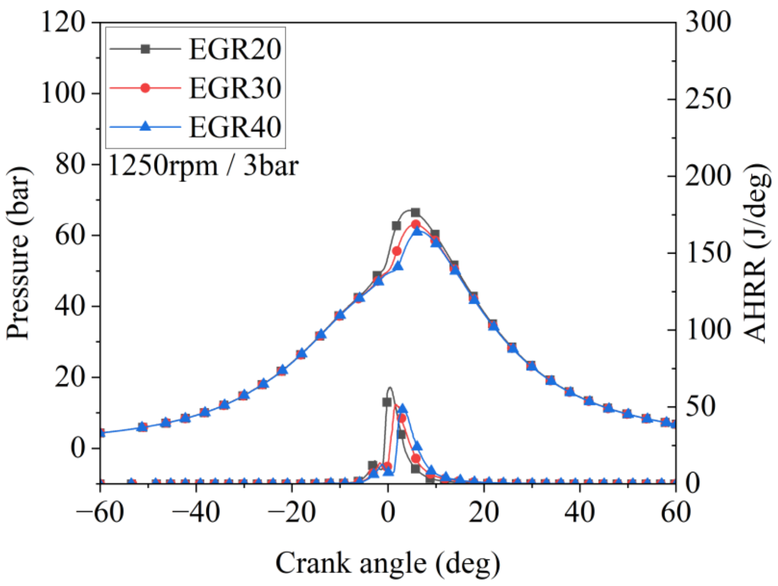

Figure 32 Effect of EGR rate on cylinder pressure and apparent heat release rate at 1250 rpm 3 bar IMEP, and 380 K TIVC.

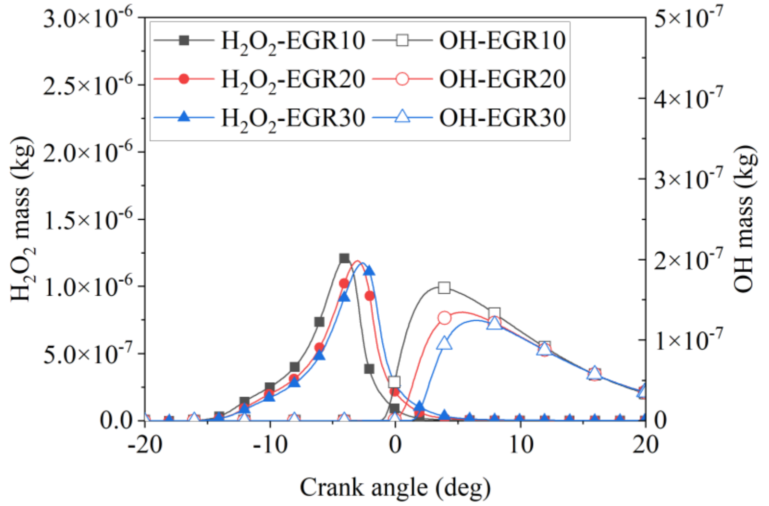

Figure 33 Effect of EGR on the formation of H_2O_2 and OH at 1250 rpm, 3 bar IMEP, 380 K TIVC.

Under the globally lean in-cylinder condition, CO is produced due to the incomplete oxidation of the fuel to CO_2. Increasing the EGR rate was found to dramatically decrease the NOx emissions due to the reduced temperature of the combustion. The reduced combustion temperature is due to the retarded combustion phasing and reduced chemical reaction rate. The increased composition of CO_2 has higher specific heat, and it will also dilute O_2 content, reduce combustion temperature, retard combustion phasing, and decrease NO formation rate.

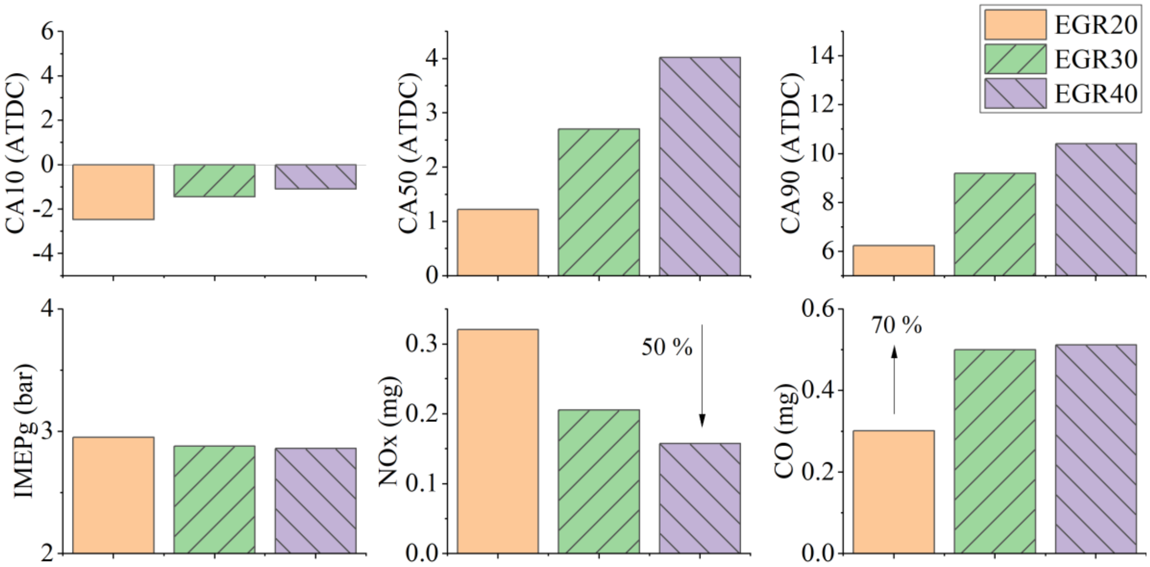

Figure 34 Effect of EGR on IMEP, combustion phasing, engine out NOx and CO emissions at 1250 rpm 3 bar IMEP, 380 K TIVC.

The effect of the EGR rate on PPCI-diffusion combustion at 2000 rpm 12 bar IMEP was more prominent than in the low load operating condition. As shown in Figure 35, increasing the EGR rate decreased the peak heat release of PPCI combustion and left more unburned fuel in the cylinder. This unburned fuel from the 1st injection pulse participated in the diffusion combustion initiated by the second injection event, and it increased the diffusion heat release rate and the prolonged ignition delay, as shown in Figure 35.

Figure 36 shows the effect of the EGR rate on H_2O_2 and OH at 2000 rpm 12 bar IMEP. Adding more EGR retarded the formation of H_2O_2 but had a negligible impact on peak H_2O_2.

However, the addition of more EGR showed significant differences in the second peak of H_2O_2. The highest peak H_2O_2 was observed at EGR30, while the lowest H_2O_2 was at EGR10. This is due to the relatively lower temperature accompanied by the lower heat release during the PPCI combustion period, which promoted the production of H_2O_2 in the intermediate temperature regime. In addition, the unburned hydrocarbon that survived in the first injection event also participated in the production of H_2O_2. Consequently, the second peak of the H_2O_2 observed at 30 % EGR case revealed the highest level.

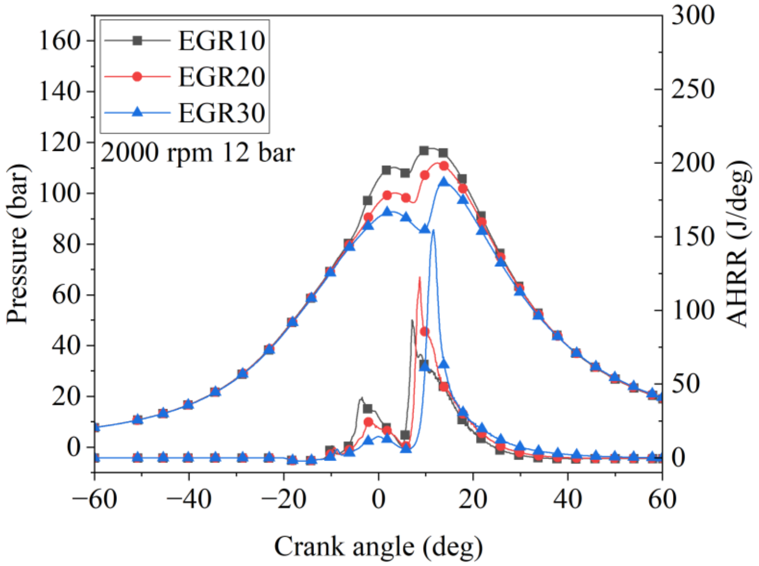

Figure 35 Effect of EGR rate on cylinder pressure and apparent heat release rate at 2000 rpm 12 bar IMEP, and 360 K TIVC.

On the contrary, the thermally elevated condition of EGR10 enabled the decomposition of H_2O_2 into OH immediately, so the level of H_2O_2 was shown to be lowest at the second peak induced by the second injection. In comparison, the peak OH was observed during the expansion stroke in the EGR10 case due to the faster decomposition of H_2O_2 under high temperature. A higher mass of OH was consumed by the CO oxidation into CO_2, releasing heat. The longer ignition delay of EGR30 increased the premixed combustion associated with the second injection, leading to an increased peak heat release rate. As shown in Figure 37, NOx was higher due to the higher combustion temperature with a lower EGR level, and the high temperature, indicated by the high level of OH, successfully oxidized CO to CO_2.

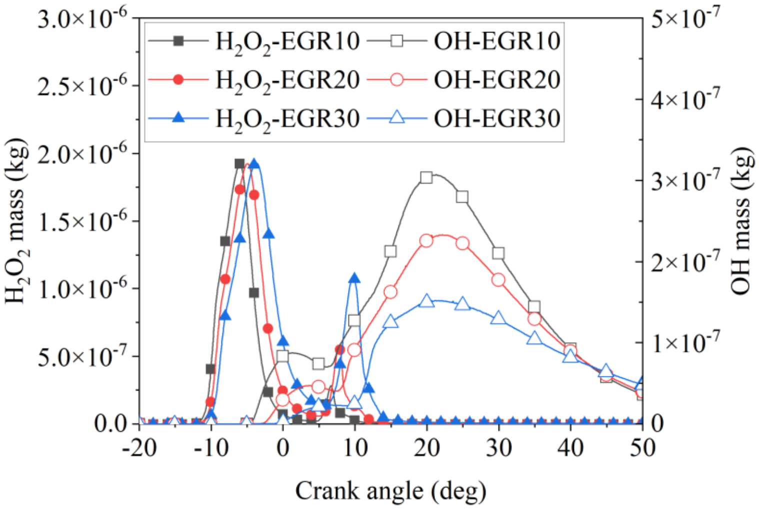

Figure 36 Effect of EGR rate on the formation of H_2O_2 and OH 2000 rpm, 12 bar IMEP, and 360 K TIVC.

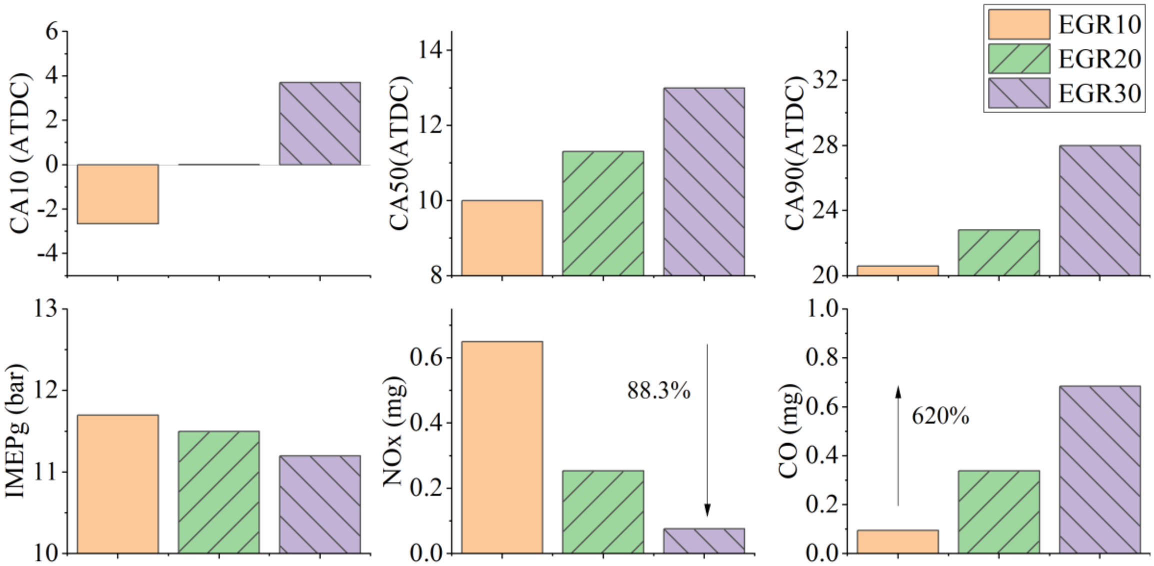

Figure 37 Effect of EGR on IMEP, combustion phasing, engine out NOx and CO emissions at 2000 rpm 12 bar IMEP, and 360 K TIVC.

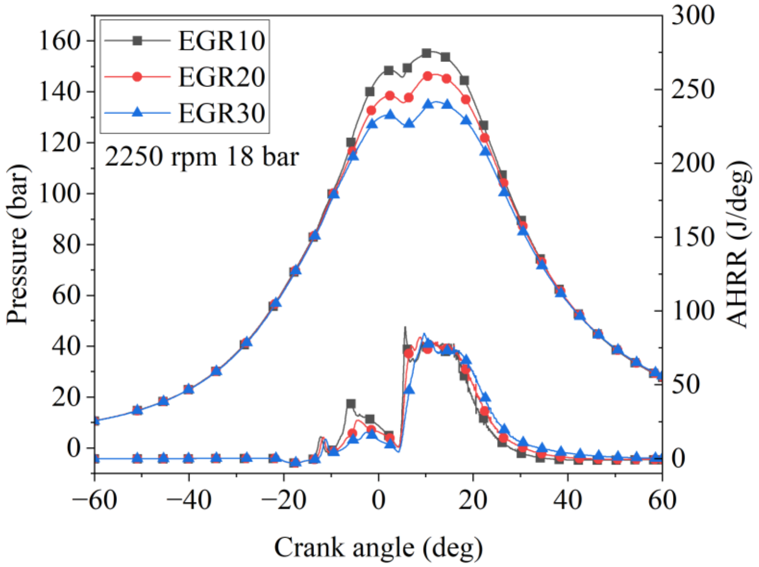

Figure 38 Effect of EGR on cylinder pressure and apparent heat release rate at 2250 rpm 18 bar IMEP, and 360 K TIVC.

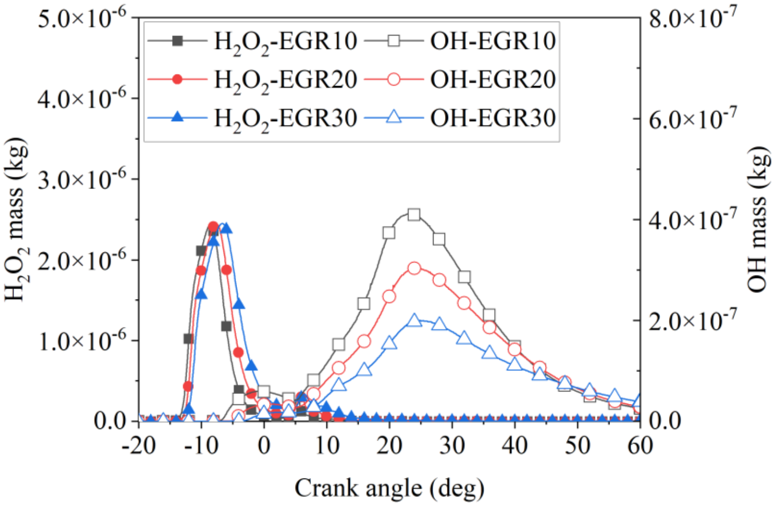

Figure 39 Effect of EGR rate on H_2O_2 and OH at 2250 rpm, 18 bar IMEP, and 360 K TIVC.

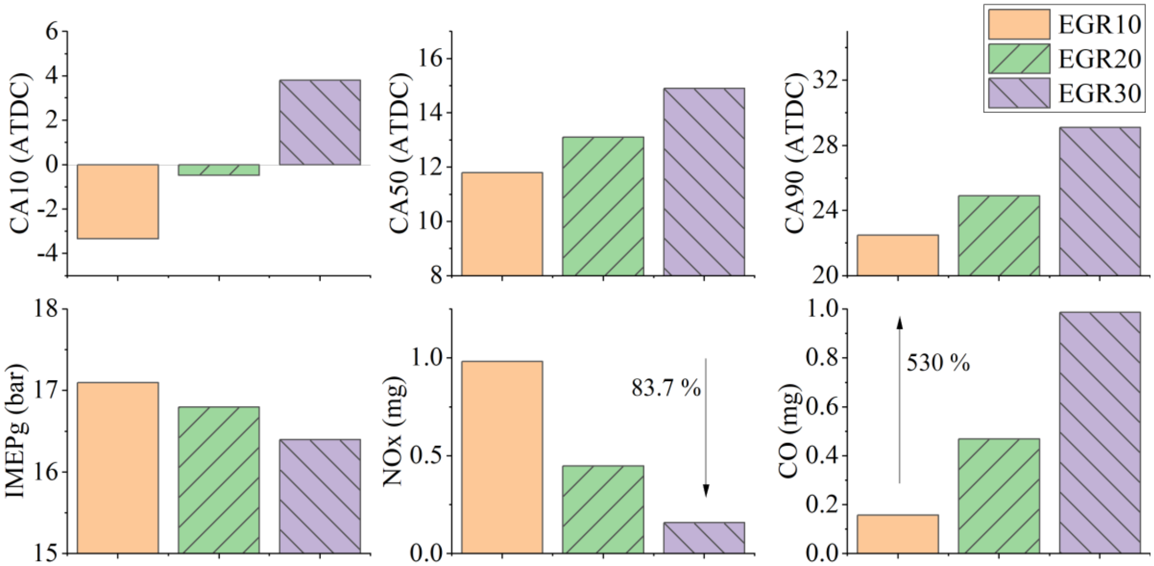

Figure 40 Effect of EGR on IMEP, combustion phasing, engine out NOx and CO emissions at 2250 rpm, 18 bar IMEP, and 360 K TIVC.

Overall combustion behaved as expected at higher load operation such as 2250 rpm 18 bar IMEP. The addition of EGR reduced and retarded the heat release rate during PPCI combustion, as depicted in Figure 38. The difference in the H_2O_2 (at -10 °CA ATDC) among the cases was insignificant during the PPCI. However, the higher in-cylinder gas temperature led to higher OH level and heat release, as shown in Figure 39. At this operating condition, the second peak of OH, observed at 2000 rpm and 12 bar IMEP with EGR30, was not observed at a high load. It can be concluded that the in-cylinder temperature during PPCI with EGR30 was already high enough to support the dissociation of H_2O_2 to OH. NOx decreased by about 84 % with the EGR rate increase, but CO increased by over five times, as shown in Figure 40.

3.5 Summary

In this chapter, the ConvergeCFD model was developed and validated against GCI combustion test results. TPRFE mechanism, consisting of 59 species and 270 reactions, was utilized to simulate the combustion process of E10 pump gasoline used in the engine test. The CFD model showed good agreement with GCI engine testing results under two operating conditions: 2000 rpm, 12 bar IMEP and 2250 rpm, 18 bar IMEP. The heat release rate and in-cylinder pressure from PPCI and diffusion combustion were well captured. The simulated combustion phasing represented by CA10, CA50, and CA90 were found to agree well with experimental data. The peak in-cylinder pressure showed less than 3 % discrepancy. NOx was slightly underestimated compared with testing data. The combustion characteristics of PPCI-diffusion combustion were well captured by the CFD model.

The effects of temperature, pressure, and EGR rate at IVC on GCI engine cylinder pressure, heat release rate, and exhaust emissions were numerically examined using the validated CFD model to support combustion model development. Thermally enhanced boundary conditions with higher temperatures had significant impacts on the PPCI combustion. Increased EGR effectively mitigated the auto-ignition process with prolonged ignition delay, leading to lower engine-out NOx and increased CO emissions. The TIVC and EGR rates at IVC play important roles in optimizing GCI combustion.

Chapter 4. Development of a Quasi-dimension PPCI-Diffusion Combustion Model and its Validation

This chapter describes the details of the quasi-dimension PPCI-diffusion model development and its validation against the experimental data. The model is developed based on the traditional combustion modeling approaches commonly employed for SI and CI models. Figure 41 presents the overall structure of the model. The model is initiated by the start of the fuel injection. The fuel is introduced as a form of packets into the cylinder at each time step. Next, spray dynamics such as penetration length, velocity, and SMD are calculated, and the amount of air entrained into the packets is also calculated.

For the combustion sub-model, if it is the first injection during the compression stroke, an ignition delay model for PPCI combustion will be developed based on the multizone approach, and the flame propagation will be estimated. If the injection event is the second pulse near TDC, the diffusion combustion ignition delay will be estimated based on the Arrhenius type of model. Heat release from each model is combined, and the new pressure and temperature are calculated at each time step. After that, the composition of new species and the formation of pollutants in the cylinder are updated and calculated. Once the calculation is finished, the next iteration is activated with the same procedure repeated until the calculation time step reaches the exhaust valve opening timing, where the majority of the fuel oxidation is assumed to be completed. The detailed description of each model is presented in the following sections.

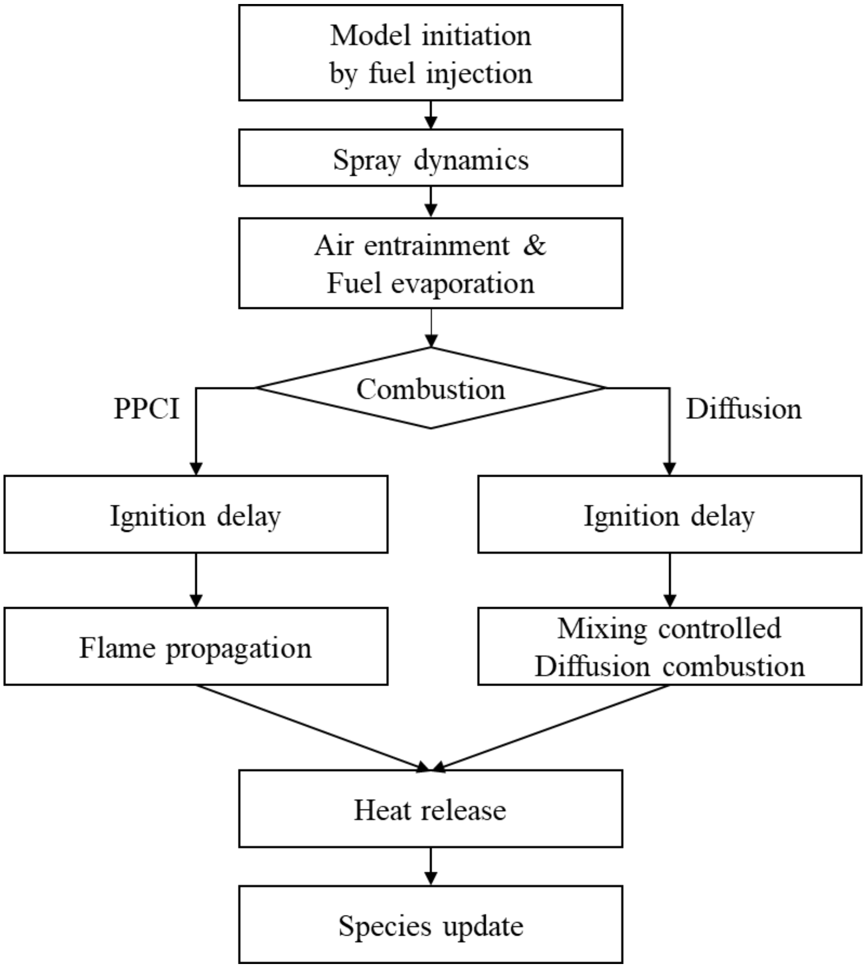

Figure 41 Overall structure of the PPCI–diffusion combustion model.

4.1 Spray Dynamics

Spray Penetration

The spray tip penetration length correlation used in this study is based on the research work by Hiroyasu et al. [47]. This spray sub-model relies on an empirical equation based on experimental data. It was commonly found from experiments that the penetration of the spray and the time showed a linear relationship before the breakup time, and the penetration length became a function of the square root of time after the breakup time, as shown in Eq. 4.1, Eq. 4.2 and Eq. 4.3.

The original correlation was calibrated against a mechanical fuel injector with relatively larger injector holes and lower injection pressure. With recent improvements in high-pressure injection systems, the models have been modified accordingly. The following is one group of the improved equations [75] referenced in this study.

$$t_b = 38.57\left(\frac{\rho_a}{\rho_0}\right)^{0.15}\frac{\rho_l d_0}{(2\rho_a \Delta P)^{0.5}} \qquad \text{Eq. 4.1}$$

$$S = 0.7\left(\frac{\rho_a}{\rho_0}\right)^{-0.25}\sqrt{\frac{2\Delta P}{\rho_l}}\,t, \qquad 0 < t < t_b \qquad \text{Eq. 4.2}$$

$$S = 4.347\left(\frac{\rho_a}{\rho_0}\right)^{-0.175}\left(\frac{2\Delta P}{\rho_a}\right)^{0.25}\sqrt{d_0 t}, \qquad t_b \leq t \qquad \text{Eq. 4.3}$$

Where, *S* is a spray tip penetration length, t_b is breakup time, ρ_a is in-cylinder air density, ρ_0 is the reference density of air at standard ambient temperature and pressure, which corresponds to 25 °C and 1 atm. ρ_l is liquid fuel density, d_0 is the diameter of the injector nozzle hole, and ΔP is the pressure difference between ambient and fuel injection pressure. The multipliers and power terms are adjustable gains for calibration in Eq. 4.1, Eq. 4.2 and Eq. 4.3.

Before spray breakup, penetration length linearly increases, and then the spray tip penetration length is proportional to $\sqrt{t}$. This model assumes that the center spray packet has the furthest penetration, and the outer packets will have less penetration length due to the higher interaction of fuel droplets with ambient gas. This can be expressed below [75]:

$$E_x = 0.5\sqrt{1 - x_s} + 0.5 \qquad \text{Eq. 4.4}$$

$$t_{bx} = E_x t_b, \qquad S_x = \sqrt{E_x S} \qquad \text{Eq. 4.5}$$

Where, E_x is a weighting factor to account for the radial deviation, x_s is non dimensional radial distance from the centerline. The center packet has 0 and the outer packet has 1. t_{bx} and S_x are weighted spray breakup time and penetration length. The model described above was at first validated against gasoline testing results from a recent study with gasoline fuel injected at high pressure [76]. The parameters tested are listed in Table 8. As shown in the table, the charge temperature was between 800 K and 1200 K, and the pressure and density were 60 bar and 23 kg/m^3, which are compatible with the engine operating condition. Therefore, these testing results were adapted as a reference for spray model validation.

Table 8 Experimental test conditions for vaporizing spray [76].

Parameter	Range
Fuels	RON92
Charge temperature [K]	800 - 1200
Charge pressure [bar]	60
Charge density [kg/m3]	23
Injection pressure [bar]	1500
Number of holes	1 (single hole)
Hole nominal diameter [mm]	0.176
Hole angular position	Axial

It was observed that the predictions from both the traditional [47] and improved model [75] from reference overpredicted the penetration compared to the testing results, as shown in Figure

42. This may be because the models were validated against diesel fuel under non-vaporizing spray conditions. This condition may not be able to represent the in-cylinder environment, where the gas temperature is much higher than the ambient temperature. In addition, the high density of the gas in the cylinder will hinder the longer development of the fuel spray penetration. Penetration length was expressed in a log scale graph, as shown in Figure 43. The modified correlations with modified gains used in this study are Eq. 4.6, Eq. 4.7, and Eq. 4.8.

$$t_b = 10.0\left(\frac{\rho_a}{\rho_0}\right)^{0.1} \frac{\rho_l d_0}{(2\rho_a \Delta P)^{0.5}} \qquad \text{Eq. 4.6}$$

$$S = 0.5\left(\frac{\rho_a}{\rho_0}\right)^{-0.3} \sqrt{\frac{2\Delta P}{\rho_l}}\, t, \qquad 0 < t < t_b \qquad \text{Eq. 4.7}$$

$$S = 5.1\left(\frac{\rho_a}{\rho_0}\right)^{-0.28} \left(\frac{2\Delta P}{\rho_a}\right)^{0.25} \sqrt{d_0 t}, \qquad t_b \le t \qquad \text{Eq. 4.8}$$

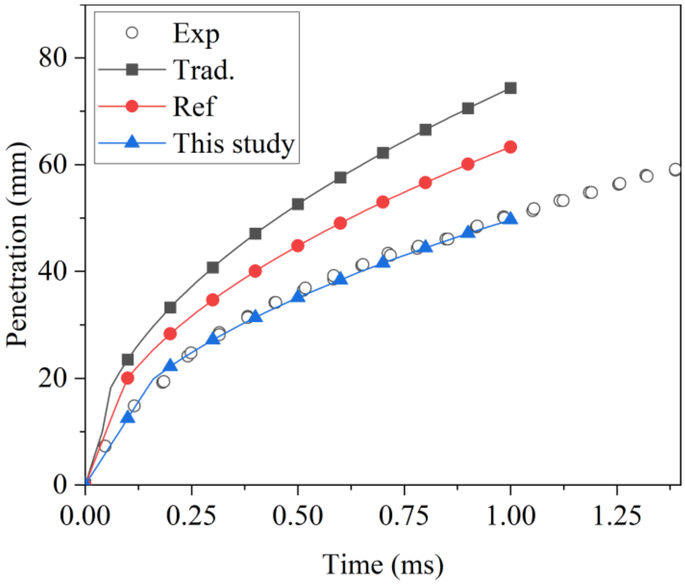

Figure 42 Variation of high-pressure gasoline spray penetration length with change in time. High-pressure gasoline fuel injection penetration experiment [76].

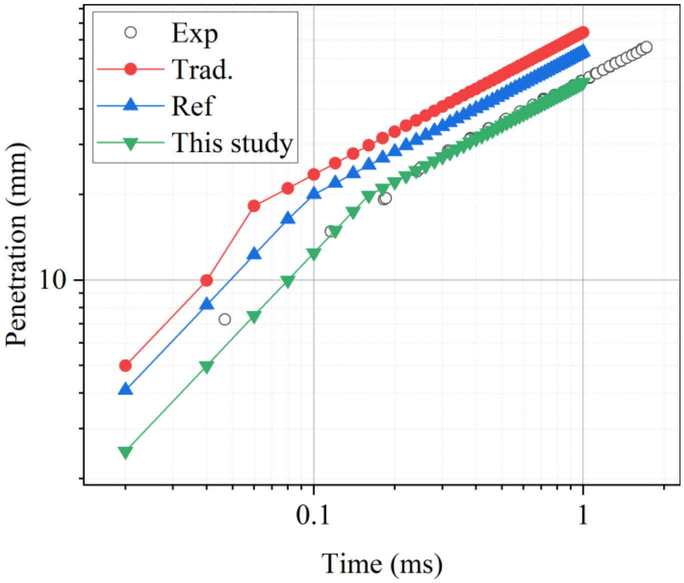

Figure 43 Comparison of variation of spray penetration measured in [76] with that predicted by the traditional penetration model [47], reference [75], and the modified model developed in this research.

The spray penetration length calculated using the revised model was found to agree well with the experiment results, as shown in Figure 42 and Figure 43. This correlation was used for the development of the combustion model. However, the traditional model still has limitations where the injection pressure at the nozzle is assumed to be constant and equal to the rail pressure, which may not always be accurate. Fuel injection results from the injection needle movements, and there exists ramp-up and ramp-down period. This should be taken into consideration, especially for short duration of injection. Therefore, injection pressure at the nozzle tip was varied to match the rate of injection profile shown in Figure 44 (b). Figure 44 compares the improved spray model with the traditional spray jet model. As shown in Figure 44 (a), the first packet will always be located at the tip of the spray plume, and the last packet is always the last packet within the spray cloud. Moreover, the fuel distribution within the cloud will be directly affected by the shape of the injection rate. For instance, the packet at the middle of the injection process will have a higher concentration for two reasons: 1) the typical rate of injection has the maximum rate at the middle of duration, and 2) the last packet will be injected at a lower pressure during ramp-down period thus has short penetration.

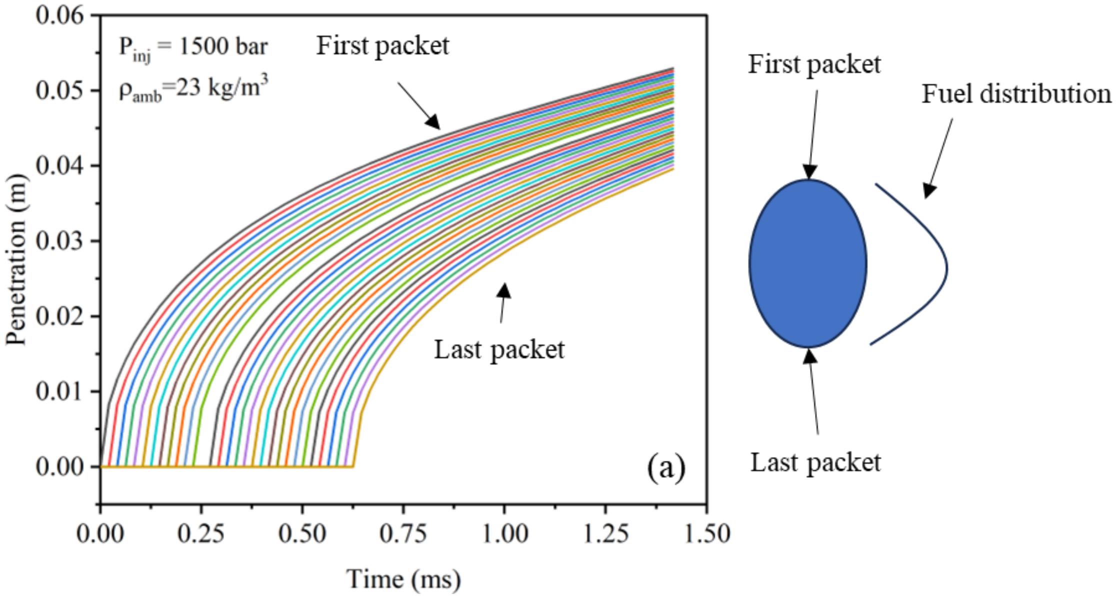

(a) Penetration length estimation from the traditional model

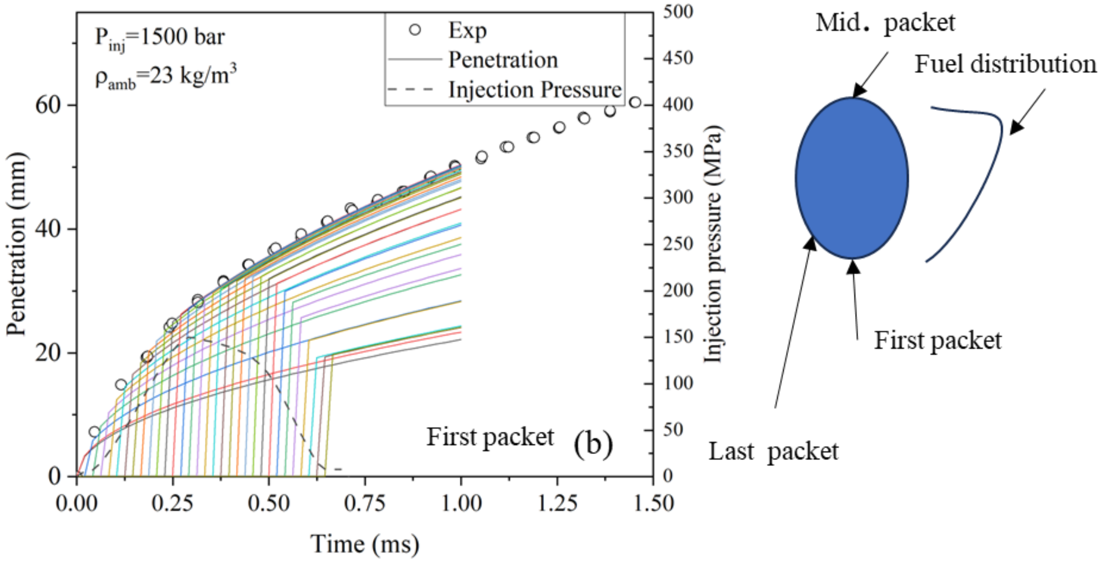

(b) Penetration length estimation from the improved model

Figure 44 Comparison between traditional model (a) and improved model (b).

The improved spray model indicated in Figure 44 (b) presents quite different behaviors from the traditional spray model shown in Figure 44 (a). Considering the transient rate of injection, the location of the first packet eventually becomes the tail of the fuel cloud, and the middle packet becomes the leading tip of the entire spray. A high concentration of the fuel is present near the tip of the spray, according to the improved model, whereas the traditional spray shows a high concentration in the middle of the spray plume.

This phenomenon is also demonstrated by CFD analysis, as depicted in Figure 45 and Figure 46. A CFD simulation was carried out in this study to understand and support the improved spray model. As shown in Figure 45, the spray tip generally had a higher equivalence ratio than the middle plume of the spray. It can be seen that the drag force slows down the spray due to the friction at the tip, and the momentum due to the injection pressure pushes the spray forward. Consequently, these two opposite forces create higher fuel concentration near the spray tip. This behavior of the spay is well described in Figure 46 and Figure 47. These two figures present the equivalence ratio distribution at the center line at -6 °CA ATDC and the spray model prediction at -6 °CA ATDC. Overall, spray behavior was reasonably captured by the improved spray model in a way that the spray tip showed the highest equivalent ratio, and the middle part of the spray plume exhibited a lower equivalence ratio. On the contrary, the traditional model shown in Figure 47 (b) was not able to capture this observation. The distribution of equivalence ratios appeared to be fairly uniform across the entire penetration length, compared to the improved model.

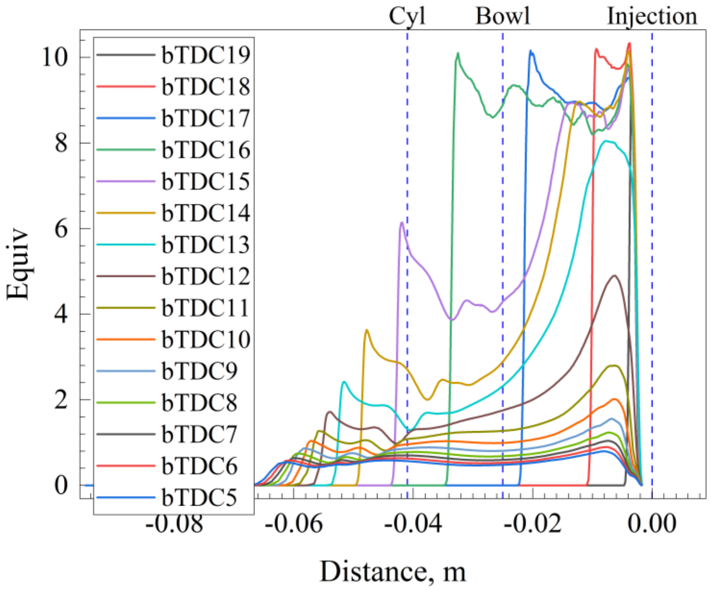

Figure 45 History of the equivalence ratio at the center line of the fuel spray from CFD simulation. Start of injection was set at -20 °CA ATDC with 1500 bar injection pressure.

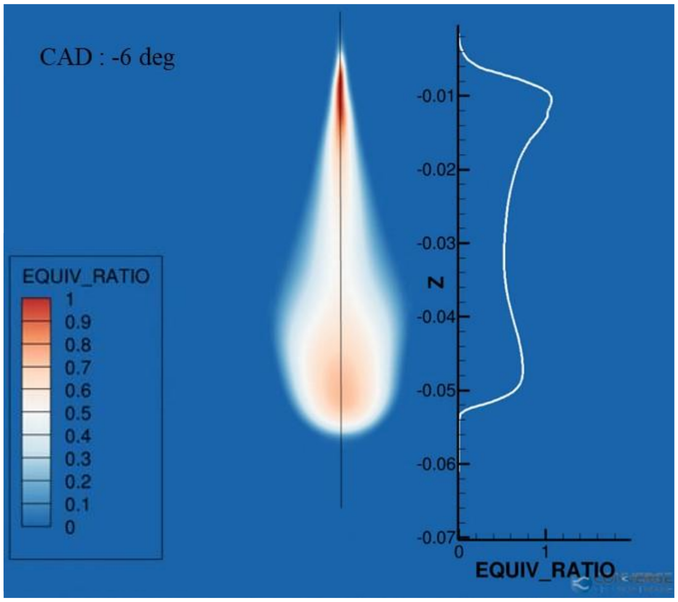

Figure 46 Equivalence ratio distribution at -6 °CA ATDC simulated using CFD model analysis.

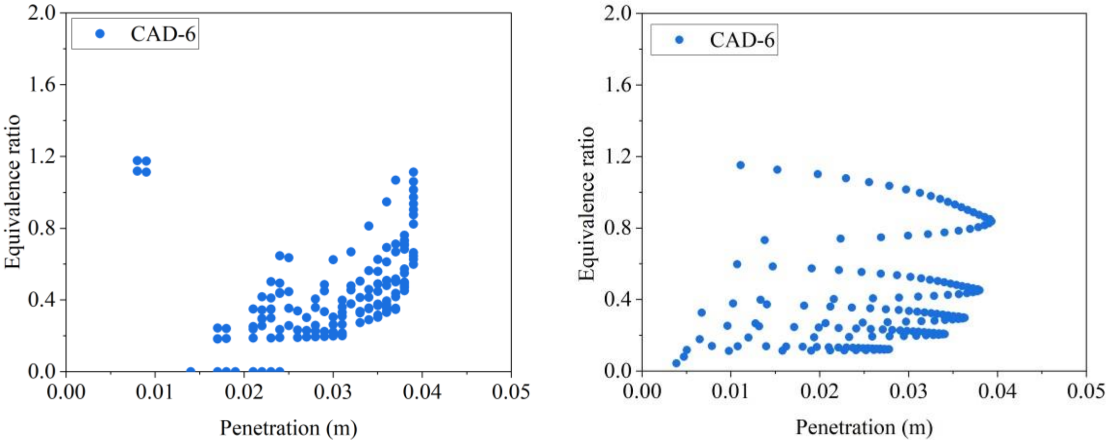

(a) Improved spray model (b) Traditional spray model

Figure 47 Simulated distribution of the equivalence ratio vs penetration length at -6 °CA ATDC estimated by (a) improved spray model, (b) traditional spray model.

In this study, five radial zones are considered for the computational efficiency and accuracy of the model. Periphery zones also showed a lower equivalence ratio than the center zone. As shown in Figure 47 (b), the equivalence ratio was more dispersed, and a relatively higher equivalence ratio was observed at 50 % of maximum penetration as opposed to the improved model. Additionally, the rate of injection was directly reflected in equivalence ratio distribution in the traditional spray model, which may not necessarily always be observed. Moreover, another vital aspect of spray models is to consider the wall impingement. The spray plume is likely to impinge the combustion chamber or intentionally make the use of spray impingement on the combustion chamber to maximize air utilization. As shown in Figure 48, the equivalence ratio at the tip of the spray plume was still higher than that observed at the main spray plume.

According to an experimental study from [77], it was stated that the wall spray loses 50 % of momentum at the wall, and the friction had less effect on spray development in the following zones. In this spray model, the diameter of the combustion chamber (~0.03 m) was considered as a wall impingement location, and it was assumed that the spray momentum was reduced by 50 %

at the wall location. It should be noted that once the fuel spray loses its momentum, mass diffusion will occur due to the concentration difference within a highly stratified environment. In this study, mass diffusion due to impingement was not considered for simplicity.

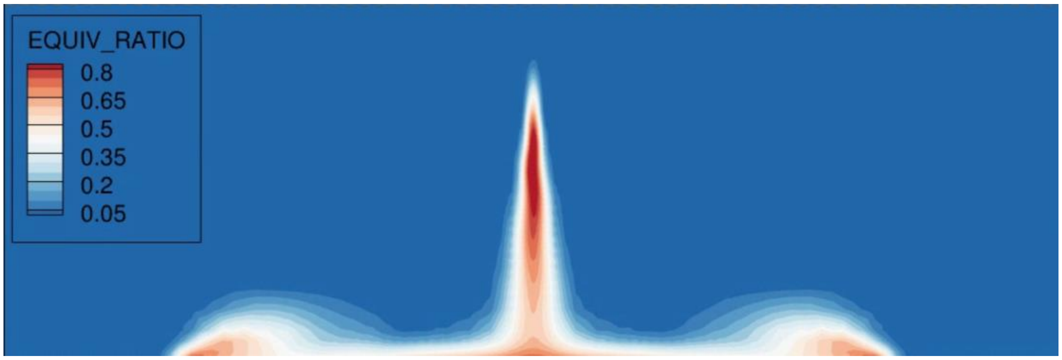

Figure 48 Equivalence ratio distribution under spray wall impingement condition. The wall location was 20 mm.

Spray Angle Estimation

Spray angle was estimated using a commonly used correlation developed by Reitz [78].

$$\tan(\theta) = \frac{1}{A} 4\pi \left(\frac{\rho_a}{\rho_l}\right)^{0.5} \frac{\sqrt{3}}{6} \qquad \text{Eq. 4.9}$$

$$A = 3.0 + 0.28\left(\frac{l_n}{d_n}\right) \qquad \text{Eq. 4.10}$$

Where, θ is spray angle, ρ_a is the density of air, ρ_l is liquid fuel density, d_n is injection nozzle hole diameter, and l_n is the length of the hole.

Droplet Diameter

It is assumed that all the droplets have the same diameter after the breakup period. The distribution of droplet size can be ignored. The SMD, d_{32}, is calculated using the following equations.

$$\frac{d_{32}}{d_n} = MAX\left(\frac{d_{32}^{LS}}{d_n}, \frac{d_{32}^{HS}}{d_n}\right) \qquad \text{Eq. 4.11}$$

$$\frac{d_{32}^{LS}}{d_n} = 4.12 Re_i^{0.12} We_i^{-0.75} \left(\frac{\mu_l}{\mu_a}\right)^{0.54} \left(\frac{\rho_l}{\rho_a}\right)^{0.18} \qquad \text{Eq. 4.12}$$

$$\frac{d_{32}^{HS}}{d_n} = 0.38 Re_i^{0.25} We_i^{-0.32} \left(\frac{\mu_l}{\mu_a}\right)^{0.37} \left(\frac{\rho_l}{\rho_a}\right)^{-0.47} \qquad \text{Eq. 4.13}$$

$$Re_i = \frac{\rho_i u_i d_n}{\mu_l} \qquad \text{Eq. 4.14}$$

$$We_i = \frac{u_i^2 d_n \rho_l}{\sigma} \qquad \text{Eq. 4.15}$$

Where, d_{32}^{LS} is incomplete spray SMD, d_{32}^{HS} is complete spray SMD, d_n is nozzle hole diameter, μ_l is the viscosity of the liquid fuel, μ_a is the viscosity of air, σ is the surface tension, ρ_l and ρ_a are density of fuel and air, Re and We are Reynolds and Weber number of fuel. i indicates index of the packets. Using these correlations, SMD can be calculated. Once the initial diameter of droplets is known, the number of droplets can also be estimated.

Fuel Evaporation

Provided that initial droplet size and fuel mass are available in each packet, the number of droplets, N, can be calculated using [46]:

$$N = \frac{6 m_{l,i}}{\pi d_{32}^3 \rho_l} \qquad \text{Eq. 4.16}$$

It is assumed that the total number of droplets doesn’t change throughout the simulation, but as liquid fuel droplets evaporate, their diameter will be reduced. The droplet size can be expressed as

$$d_l = \left[\frac{6\left(m_{l,i} - \int dm_{fg}\right)}{\pi N \rho_l}\right]^{1/3} \quad \text{Eq. 4.17}$$

$$\frac{dm_{fg}}{dt} = -\frac{dm_l}{dt} \quad \text{Eq. 4.18}$$

$$= \pi d_i N D_v Sh \frac{P_t}{R_v T_m} \ln\left(\frac{P_t}{P_t - P_{v,surf}}\right) \quad \text{Eq. 4.19}$$

$$T_m = \frac{T_a + T_l}{2} \quad \text{Eq. 4.20}$$

$$k_m = \left(1 - \frac{P_{v,surf}}{2P_t}\right) k_a + \left(\frac{P_{v,surf}}{2P_t}\right) k_v \quad \text{Eq. 4.21}$$

$$M_m = \left(1 - \frac{P_{v,surf}}{2P_t}\right) M_a + \left(\frac{P_{v,surf}}{2P_t}\right) M_v \quad \text{Eq. 4.22}$$

$$\mu_m = \left(1 - \frac{P_{v,surf}}{2P_t}\right) \mu_a + \left(\frac{P_{v,surf}}{2P_t}\right) \mu_v \quad \text{Eq. 4.23}$$

$$C_{p_m} = \left(1 - \frac{P_{v,surf}}{2P_t}\right) C_{p_a} + \left(\frac{P_{v,surf}}{2P_t}\right) C_{p_v} \quad \text{Eq. 4.24}$$

$$\rho_m = \frac{P_t M_m}{R T_m} \quad \text{Eq. 4.25}$$

$$Re_d = \frac{\rho_m u d_l}{\mu_m} \quad \text{Eq. 4.26}$$

$$Pr = \frac{C_{pm} \mu_m}{k_m} \quad \text{Eq. 4.27}$$

$$Sc = \frac{\mu_m}{\rho_m D_v} \quad \text{Eq. 4.28}$$

$$Nu = 2 + 0.6\, Re_d^{0.5}\, Pr^{\frac{1}{3}} \quad \text{Eq. 4.29}$$

$$\mathrm{Sh} = 2 + 0.6\, \mathrm{Re}_{\mathrm{d}}^{1/2} \mathrm{Sc}^{1/3} \quad \text{Eq. 4.30}$$

$$z = \frac{C_{pv} \frac{dm_{fg}}{dt}}{\pi d_l N k_m Nu} \quad \text{Eq. 4.31}$$

$$\frac{DT_l}{dt} = \frac{1}{m_l C_{pl}}\left(q - \lambda \frac{dm_{fg}}{dt}\right) \qquad \text{Eq. 4.32}$$

$$q = \pi d_l N k_m (T_g - T_l) Nu \left(\frac{z}{e^z - 1}\right) \qquad \text{Eq. 4.33}$$

Where, d_l is droplet diameter, $m_{l,i}$ is fuel mass, m_{fg} is gas-phase fuel mass, D_v is mass diffusivity, Sh is the Sherwood number, P_t is total pressure, R_v is gas constant, T_a is ambient temperature, T_l is bulk temperature of droplet. $P_{v,surf}$ is saturation pressure at the droplet temperature. $T_m, k_m, M_m, \mu_m, and\ C_{p\,m}$ are the mean temperature, conductivity, molar weight, viscosity, specific heat at the fuel droplet film. a and v denote ambient air and vapor phase of the fuel. $Re_d, Pr, Sc, Nu,$ Sh are Reynold, Prandtl, Schmidt, Nusselt, and Sherwood numbers. z is the correction factor due to the thickened boundary layer caused by mass transfer. q is convective heat transfer to the droplet, and λ is specific heat capacity of the fuel.

At each time step, the temperatures of liquid fuel droplets as well as the vaporized fuel are calculated and updated. The vaporized fuel is considered combustible and forms an air-fuel mixture. However, for the GCI combustion model, the gasoline fuel droplet evaporation occurs almost instantaneously. Gasoline's fast evaporation is also shown in other numerical studies. For example, gasoline evaporates up to 20 times faster than diesel when evaluated at 600 K and 55 bar conditions [79].

4.2 Multizone Model

The multizone model approach is utilized for ignition delay during PPCI combustion, and the ignition delay was determined by the temperature and equivalence ratio of each zone. Spray packets described in the previous section are considered imaginary zones. The composition of each zone is derived from the spray dynamics and air-entrained sub-models. Five packets from the spray model were selected based on the equivalence ratio ranging from 1.2 to 0.5 and considered for ignition delay estimation. The descriptions of the model calculation are presented in the below section.

Conservation of Species Mass

Based on the conservation of mass, the variation rate of species mass fraction in a gas mixture can be stated as

$$\frac{dY_{k,i}}{dt} = \frac{\omega_{k,i} M_i}{\rho_k} + \frac{1}{\rho_k v_k}\sum_{j}^{JJ} me_j\left(y_i^j - Y_{k,i}\right) \qquad \text{Eq. 4.34}$$

Where i and k represent the species and zone number, respectively, and j indicates the mass exchange port number in a system. Y is species mass fraction, ω is species production rate (mole/cm^3), M is the molar weight (g/mole), ρ is the density in g/cm^3, v is the volume of the zone, and *me* is the mass flow rate (g/s) via intake or exhaust ports. In this study, each zone is considered as closed volume, so *me* can be ignored. Using the first law of thermodynamics, one can obtain the temperature of a zone as follows [20]:

$$\frac{dT_k}{dt} = \frac{\frac{1}{m_k}\frac{dQ_k}{dt} - \sum_{i=1}^{KK}\frac{h_{k,i}}{M_i}\frac{dT_{k,i}}{dt} + \frac{RT_k}{M_k}\left(\frac{\sum_{l\neq k}^{N}\frac{m_l}{M_l}\frac{dT_l}{dt}}{\sum_{l=1}^{N}\frac{m_l}{M_l}T_l} - \frac{1}{V}\frac{dV}{dt} - \frac{\sum_{l=1}^{N}\frac{m_l}{M_l^2}T_l\frac{dM_l}{dt}}{\sum_{l}^{N}\frac{m_l}{M_l}T_l}\right)}{\left(\sum_{i}^{KK}\frac{Y_{k,i}}{M_i}C_{p,k,i} - \frac{R}{M_k^2}\frac{m_k T_k}{\sum_{l=1}^{N}\frac{m_l}{M_l}T_l}\right)} \qquad \text{Eq. 4.35}$$

Where, T_k *and* T_l is the temperature of the zones, $h_{k,i}$ is the specific enthalpy of species i in zone k, m_i and m_k are the mass of the zone, R is the universal gas constant, N is the number of the zone used, KK is number of species, $C_{p,k,i}$ is the specific heat of the species i in zone k, M_l is the mean molar weight of the zone l, and V is the volume of the combustion chamber.

The change of pressure in a cylinder with time can be calculated by solving,

$$\frac{dp}{dt} = \frac{R}{V}\sum_{k=1}^{N}\frac{m_k}{M_k}\frac{dT_k}{dt} - \frac{p}{V}\frac{dV}{dt} - \frac{R}{V}\sum_{k=1}^{N}\frac{m_k}{M_k^2}T_k\frac{dM_k}{dt} \qquad \text{Eq. 4.36}$$

4.3 Phenomenological Model.

Thermodynamic combustion models are widely used due to their superior advantages of relatively low computational burden and easy of handling. Therefore, some physical phenomena are often absent and replaced by empirical correlation to meet various research objectives. However, combustion is a highly complex physical and chemical phenomenon, including thermochemical reactions and turbulent flow within a cylinder. As a result, thermodynamic models may not be suitable to predict reliable estimations when the thermodynamic conditions and boundary conditions vary. On the other hand, a 3D CFD model discretizes the control volume into numerous local sub-spaces, called mesh, and solves governing equations at each space to explain the detailed physical phenomena. Although CFD analysis can provide very detailed information, its drawback is that it is computationally expensive. In addition, CFD often requires a better understanding to set up the model and to interpret the results. Consequently, there has been a need for an intermediate and balanced approach that addresses the primary physical characteristics with less computational burden.

Phenomenological Flame Propagation Model

The flame propagation model during PPCI was based on conventional SI combustion approach, and it can be briefly described as follows: The combustion is initiated by the ignition initiated by auto ignition instead of a spark. The ignition will initiate a small flame kernel, and the flame then rapidly grows and propagates within a turbulent space at a certain flame propagation speed. At the end of combustion, the flame will be terminated upon the depletion of the available fuel, or the flame front will be gradually terminated when approaching the wall.

Some parts of the phenomenological SI combustion model were employed in this study to mimic these fundamental observations after replacing the source of ignition from a spark to auto ignition. Unlike the thermodynamic model described in previous sections, in which the combustion process is replaced with a pre-determined finite heat release, the phenomenological SI combustion model is derived from the coupled analysis of the turbulent flow characteristics and flame development with some of the following assumptions. The below description of the SI model is the well-known two-zone combustion model from a reference [80].

- In-cylinder flow is characterized by length scales and turbulent intensity.
- Turbulent flow is assumed to be isotropic and homogeneous.
- Dissipation of turbulent kinetic energy in large eddies can be negligible.
- Macroscale and turbulent intensity after ignition are evaluated by assuming the conservation of angular momentum for the large eddies.
- Combustion contains two processes: flame entrainment and burnup process.

According to a study [80], the mass entrainment rate into the burned zone can be expressed as

$$\frac{dm_e}{dt} = \rho_u A_f (S_L + u') \qquad \text{Eq. 4.37}$$

Where m_e is the mass entrained into the burned zone, ρ_u is the density of the unburned zone, A_f is the flame front area, S_L is laminar flame speed, and u' is turbulent intensity, which is root mean square of turbulent flow fluctuation. This intensity is assumed to be turbulent flame speed ($u' = u_T$) [81]. An illustration of flame propagation is shown in Figure 49. Burned and unburned zones are divided by the flame front in red in Figure 49, and the flame front will diffuse to the unburned zone at a laminar flame speed S_L. Also, unburned mixture will enter at a characteristic velocity u_T due to turbulent convection. The flame front area is assumed to be spherical during initial development but will deform to adapt to the combustion domain as the front approaches the cold walls.

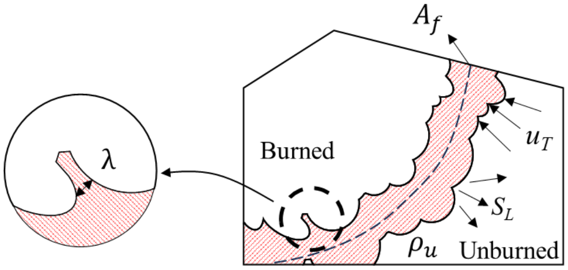

Figure 49 Illustration of turbulent flame propagation [81]

After the mixture is entrained into the burned zone, the entrained gas burning rate can be expressed as

$$\frac{dm_b}{dt} = \frac{m_e - m_b}{\tau} \qquad \text{Eq. 4.38}$$

Where, m_b is the mass of the burn mixture, and τ is the burning characteristic time, which is defined as

$$\tau = \frac{\lambda}{S_L} \qquad \text{Eq. 4.39}$$

Where, λ is the Taylor microscale which represents the distance between Kolmogorov vortices, and τ is the time for flame to travel the distance λ at speed S_L.

The differential equation of burning mass rate will replace the finite heat release explained in the thermodynamic model, and by applying the same equation, temperatures of zones can be obtained.

The laminar flame speed S_L is

$$S_L = S_{L0}\left(\frac{T_u}{T_0}\right)^{\alpha}\left(\frac{p}{p_0}\right)^{\beta}\left(1 - 2.06\tilde{x}_b{}^{0.77}\right) \qquad \text{Eq. 4.40}$$

$$S_{L0} = B_m + B_\phi(\phi - \phi_m)^2 \qquad \text{Eq. 4.41}$$

Where, $\alpha = 0.68\phi^2 - 1.7 + 3.18$

$\beta = -0.52\phi^2 + 1.18\phi - 1.08$

Where, S_{L0}, α and $\beta$are constants. T_0= 297 K and P_0 = 101,325 Pa. For gasoline fuel, B_m is 0.35 m/s, B_ϕ is -0.549 m/s, and ϕ_m is 1.1.

$$\frac{\lambda}{L} = \left(\frac{15}{A}\right)^{0.5}\left(\frac{u'L}{v}\right)^{-0.5} \qquad \text{Eq. 4.42}$$

Where, λ is the Taylor microscale, L is integral length scale, A is unity due to the isotropic assumption, and v is a kinetic viscosity of the unburned gas mixture. This can be obtained by correlation with unburned gas temperature T_u and density ρ_u As shown below.

$$v = 3.3 \times 10^{-7}\frac{T_u^{0.7}}{\rho_u} \qquad \text{Eq. 4.43}$$

The integral length scale L in Eq. 4.42 before combustion can be assumed to be the distance from the piston top to the head since the smallest spatial distance will constrain the largest turbulent eddy size.

$$L = \frac{4V}{\pi B^2} \qquad \text{Eq. 4.44}$$

Where, V is the cylinder volume, and B is the cylinder bore. Turbulence intensity u' can be estimated from the energy cascade model, $k - \varepsilon$ model, during compressions stroke. K is mean kinetic energy, and k is kinetic turbulent energy. Based on this $k - \varepsilon$ model, *K* is converted into *k*, and *k* is dissipated on the Kolmogorov scale. U is the mean flow velocity. Also, the rate of mean kinetic energy and turbulent energy are presented below.

$$K = \frac{1}{2} m U^2 \qquad \text{Eq. 4.45}$$

$$k = \frac{3}{2} m u'^2 \qquad \text{Eq. 4.46}$$

$$\frac{dK}{dt} = \frac{1}{2}\dot{m}_i v_i^2 - P_i - K\frac{\dot{m}_e}{m} \qquad \text{Eq. 4.47}$$

$$\frac{dk}{dt} = P_t - m\varepsilon - k\frac{\dot{m}_e}{m} \qquad \text{Eq. 4.48}$$

Where m is mass, $\dot{m}_i$ and $\dot{m}_e$ are the mass flow rates of in and out flow and v_i is the speed of the flow. P_t and ε are the production and dissipation rate of the turbulent kinetic energy. They are defined as below.

$$P_t = 0.3307 c_\beta \left(\frac{K}{L}\right)\left(\frac{k}{m}\right)^{0.5} \qquad \text{Eq. 4.49}$$

$$\varepsilon = \frac{u'^3}{L} = \frac{(2k/3m)^{1.5}}{L} \qquad \text{Eq. 4.50}$$

Where, c_β is a adjustable multiplier.

During combustion, the turbulence intensity and integral length scale are governed by the conservation of angular momentum of large eddies. L_0, u', and ρ_{u0} are integral length scale, turbulence intensity, and unburned gas density, respectively, at the start of combustion.

$$\frac{L}{L_0} = \left(\frac{\rho_{u0}}{\rho_u}\right)^{1/3} \quad \text{Eq. 4.51}$$

$$\frac{u'}{u'_0} = \left(\frac{\rho_u}{\rho_{u0}}\right)^{1/3} \quad \text{Eq. 4.52}$$

Phenomenological CI Combustion Model

One of the widely used CI combustion models is a jet model developed by Hiroyasu [47]. This phenomenological model framework is adapted throughout this research to develop the PPCI and diffusion combustion model. This phenomenological combustion model introduces complex sub-models to account for complex liquid jet phenomena: atomization, droplet evaporation, air entrainment, ignition, and heat release process. Although all the fundamentals of physics haven't been fully understood, major characteristics of jet spray have been modeled at a certain level of accuracy and utilized for direct injection diesel engines for decades.

Figure 50 and Figure 51 illustrate the overall structure of the jet model, including sub-models. This combustion model begins with a fuel injection event. At each time step, fuel packets are radially and axially distributed. Spray dynamics such as penetration tip length, velocity, and acceleration rate are estimated using fuel injector specifications. In this framework, ambient air entrainment into spray plum affects many aspects of the prediction throughout the models because air available within a packet determines thermodynamic state, air/fuel ratio, etc., which play a significant role for the rest of the sub-models, including heat release and emissions estimation. The detailed description of each model is presented in a later section.

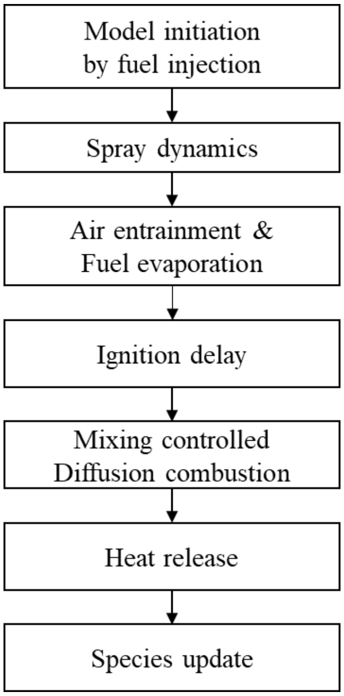

Figure 50 Flow chart of phenomenological CI combustion model in this study.

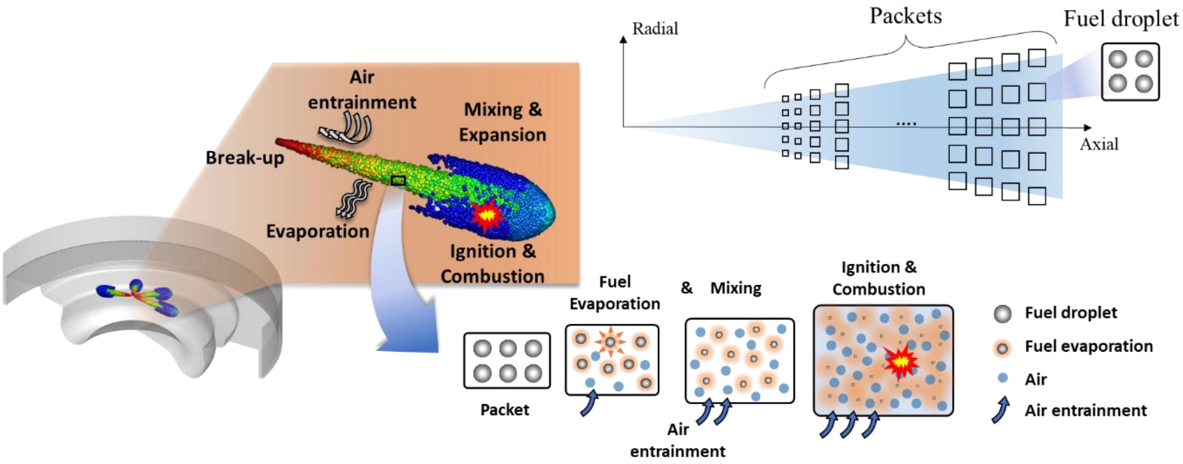

Figure 51 Illustration of direct fuel injection and phenomenological spray jet model.

Air Entrainment Model

As illustrated in Figure 51, the ambient gas in a cylinder will entrain into each packet as the spray develops. The air entrainment can be estimated by the conservation of momentum as presented in Eq. 4.53. Each packet exits the injector nozzle with an initial velocity, and it is assumed that the initial momentum is conserved at each time step. With this approach, the air entrained into each packet can be obtained. At each time step, this first-order ordinary differential equation (ODE) in Eq. 4.53 is solved to update the amount of air.

$$\frac{dm_a}{dt} = \frac{2m_{f0}^2 v_0^2}{\sqrt{v_0}\left(\frac{\rho_l}{\rho_a}\right)^{\frac{1}{4}}\sqrt{\alpha_b E_x d_0}\left(m_a + m_{f0}\right)} \qquad \text{Eq. 4.53}$$

$$v_0 = 0.70\left(\frac{\rho_a}{\rho_0}\right)^{-0.25}\sqrt{\frac{2\Delta P}{\rho_l}} \qquad \text{Eq. 4.54}$$

Where m_a is mass of the entrained air, m_{f0} is the fuel mass in a packet, v_0 is the initial velocity of the packet at the start of injection, $p_a\ and\ \rho_l$ are the density of air and liquid fuel, respectively. d_0 is the nozzle diameter. E_x is the weighting factor which compensates for the distribution of the fuel in a radial direction, and ΔP is the pressure difference between injection pressure and ambient pressure.

Ignition Delay Model

Ignition delay is defined as the time duration from the start of injection to the start of ignition. In the original spray jet model framework, an Arrhenius form of ignition delay model is commonly employed and has shown satisfactory estimation. In this PPCI-diffusion combustion modeling for GCI, both chemical kinetics and Arrhenius-type correlation are employed. For PPCI combustion featured with the distinct separation between the end of injection and the start of ignition, the packets are sorted out with respect to the equivalence ratio. It is assumed that there are virtual tiny homogeneous zones with different equivalence ratios. Chemistry kinetics are then directly solved in each zone to estimate the ignition delay. This methodology ensures the accurate estimation of the prolonged ignition delay caused by the lower reactivity of the gasoline fuel. Ideally, solving chemistry kinetics at all the packets would produce the most accurate ignition delay. However, considering the objectives of this study and the computational burden, a second-order polynomial ignition delay correlation with respect to the equivalence ratio was constructed at every cycle when the first injection pulse ends. Afterward, the ignition delay for each packet is evaluated at each time step. Once the ignition delay period meets, ignition occurs.

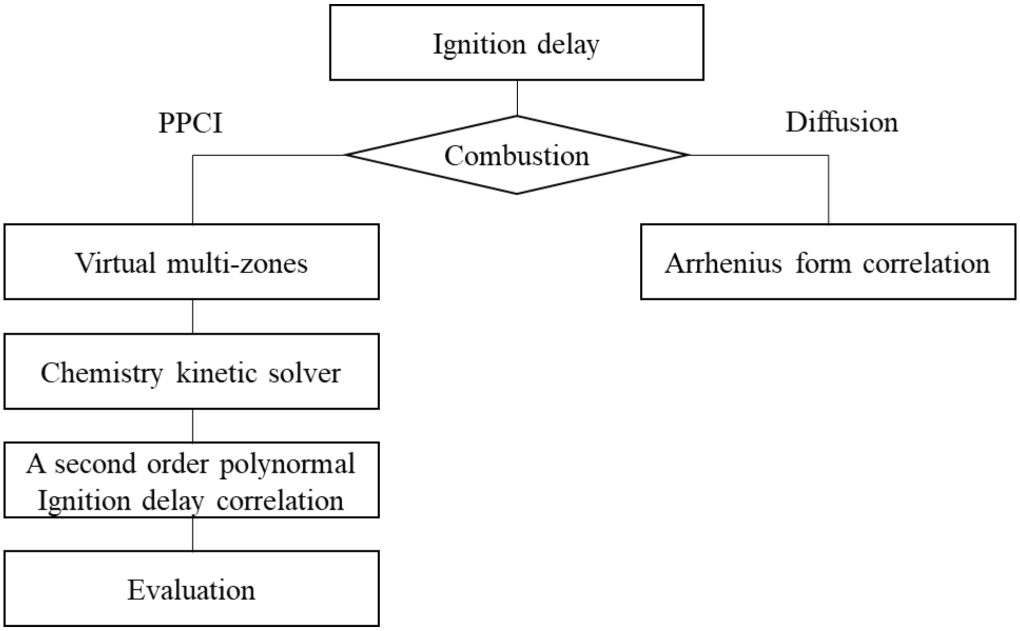

Figure 52 Flow chart of the ignition delay sub-model.

For mixing controlled diffusion combustion strategy, an Arrhenius form of ignition delay equation developed by DelVescovo et al. [82] was employed. For this model, extensive numerical simulations were performed to develop the correlation for PRF blends. Ignition delay simulation using constant volume was carried out with a range of PRF0~100, initial temperatures from 570 to 1860 K, initial pressures from 10 to 100 atm, oxygen molar fraction from 12.6 to 21 %, and equivalence ratio from 0.3 to 1.5. In total, 6,480 cases were simulated, coupled with 323 species, to develop this ignition delay correlation. The ignition delay of PRF88 used in this study was calculated by the following equations [82], and Table 9 lists the parameters used in the equations.

$$\tau = A\phi^{\alpha} p^{\beta} x_{O_2}^{\gamma} \exp(\lambda) \tag{Eq. 4.55}$$

$$\alpha = \alpha' + \left(\sum_{i=0}^{3} a_i T^{*i}\right) \exp\left\{-\left[\frac{T^*}{(T^*_{\alpha} + dT^*_{\alpha} \times PRF)}\right]^{(n_{\alpha} + dn_{\alpha} \times PRF)}\right\} \tag{Eq. 4.56}$$

$$\beta = \beta' + \left(\sum_{i=0}^{3} b_i T^{*i}\right) \exp\left\{-\left[\frac{T^*}{\left(T^*_{\beta} + dT^*_{\beta} \times PRF\right)}\right]^{(n_{\beta} + dn_{\beta} \times PRF)}\right\} \tag{Eq. 4.57}$$

$$\gamma = \gamma' + \left(\sum_{i=0}^{3} c_i T^{*i}\right) \exp\left\{-\left[\frac{T^*}{\left(T^*_{\gamma} + dT^*_{\gamma} \times PRF\right)}\right]^{(n_{\gamma} + dn_{\gamma} \times PRF)}\right\} \tag{Eq. 4.58}$$

$$\begin{aligned} \lambda = \sum_{i=0}^{2} d_i T^{*i} - \Bigg[\sum_{i=0}^{2} d_i T^{*i} \\ - \sum_{i=0}^{3} e_i T^{*i}\Bigg] \exp\left\{-\left[\frac{T^*}{\left(T^*_{\lambda} + \sum_i^2 dT^*_{\lambda i} \times PRF^i\right)}\right]^{(n_{\lambda} + \sum_{i=1}^{2} dn_{\lambda i} \times PRF^i)}\right\} \end{aligned} \tag{Eq. 4.59}$$

$T^* = 1000/T$, and the parameter values for $\alpha, \beta, \gamma, and\ \lambda$ are listed.

Table 9 List parameters and values used in Eq. 4.55 to Eq. 4.59

Parameter	Value	Parameter	Value
A	1.0	γ'	-0.2956
α'	-0.1301	γ_0	16.78
a0	2.228	γ_1	-65.79
a1	-3.123	γ_2	80.55
A2	0.1977	γ_3	-32.57

A3	0.1887	T_{γ}^{*}	1.276
T_{α}^{*}	1.334	dT_{γ}^{*}	0.0001591
dT_{α}^{*}	0.001179	n_{γ}	12.53
n_{α}	9.495	dn_{γ}	-0.05869
dn_{α}	-0.01916	d_0	9.314
β'	-0.1896	d_1	-19.54
B0	10.53	d_2	10.67
B1	-42.87	e_0	132.2
B2	55.54	e_1	-454.4
B3	-24.35	e_2	528.4
T_{β}^{*}	1.199	e_3	-215.2
dT_{β}^{*}	0.0003184	T_{λ}^{*}	1.196
n_{β}	10.27	$dT_{\lambda 1}^{*}$	9.683e-6
dn_{β}	-0.04541	$dT_{\lambda 2}^{*}$	4.592e-6
		n_{λ}	8.538
		$dn_{\lambda 1}$	-0.02678
		$dn_{\lambda 2}$	-2.063e-5

Ignition delay is calculated at each time step for a given equivalence ratio and the instantaneously varying thermal conditions. The autoignition integral approach developed by Livengood and Wu [83] is used to determine the ignition timing.

Eq. 4.60

$$\int_{t=0}^{t_i} \frac{1}{\tau} = 1$$

Where τ is the induction time obtained from the ignition delay model, and t is the elapsed time from the start of injection. The integration is performed for each packet at each time step, and when the integration reaches unity, the ignition delay period ends upon the start of combustion. This approach is based on the assumption that the species only rely on the gas state and that the concentration of the species doesn’t change in each step during the ignition delay period.

Heat Release

After the ignition delay period, a rapid exothermic chemical reaction occurs while hydrocarbons break down into smaller hydrocarbon molecules. For PPCI combustion initiated by the first injection at the end of the compression stroke, air-fuel mixture mass in a packet will be transferred to the burned zone once ignition delay is determined. Since PPCI combustion is characterized by both spontaneous ignition at multiple points and flame propagation to some degree, both phenomena are accounted for in this research.

Starting from the injection, the location of packets within the cylinder is tracked, with the ignition point identified by the ignition delay model. Knowing the location of the packet just ignited, the relative distance, R_f, between all the packets and the ignition point, are calculated, and the packets within the flame front are considered as burned mass, as shown in Figure 53. In addition, if a packet reaches the Livengood and Wu autoignition integral before the flame front, the mass of the packet is considered a burned mixture, which is burned through auto-ignition. Applying these two criteria ensures that the PPCI characteristics of having multiple ignition points accompanying flame propagation will be modeled.

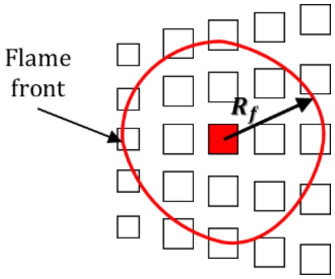

Figure 53 Illustration of ignition location and flame radius.

The radius of the flame front, R_f, is calculated at each calculation as

$$\frac{dR_f}{dt} = (S_L + u') \qquad \text{Eq. 4.61}$$

Where, S_L is the laminar flame speed, and u' is turbulent intensity.

For mixing controlled combustion by the consecutive injection events, the heat release is controlled by the availability of the fuel and entrained air. It is assumed that the liquid phase fuel left in the packet doesn't participate in the combustion process and that the burned air-fuel mixture mass is determined by stoichiometry, as proposed by Hiroyasu [84].

$$\Delta m_{fuel} = \frac{m_a}{AFR_{stoich}} \quad \emptyset > 1 \qquad \text{Eq. 4.62}$$

$$\Delta m_{fuel} = m_{fg} \quad \emptyset < 1 \qquad \text{Eq. 4.63}$$

When the available air-fuel mixture in a packet is rich, the fuel to be burned is dominated by the availability of the air in the packet. When the mixture is lean, which means there is enough air available, the evaporated fuel will be burned. Any remining air or fuel will be consumed in the same manner at the next calculation step. It should be stated that, with this method, the burning rate cannot be accurately estimated when EGR is present. In fact, the burned gas will be entrained into packets because of the PCCI combustion from the first injection. Less oxygen content and the presence of burned gases will slow down the burning speed. This characteristic cannot be captured with the method shown above. Therefore, another criterion, $\dot{m}_{chem}$, is employed to limit the burn rate by the chemical reaction [85].

$$\Delta m_{fuel} = \dot{m}_{chem} \times \Delta t \qquad \text{Eq. 4.64}$$

$$\dot{m}_{chem} = A_d \exp\left(-\frac{E_a}{RT}\right) [fuel]^{0.25} [O_2]^{1.5} V_{pac} \times M_{fuel} \qquad \text{Eq. 4.65}$$

A_d is a gain, E_a is activation energy, which is assumed as 30 kcal/mol, R is gas constant, T is gas temperature, bracket denotes the molar concentration of species in mole/cm^3. V_{pac} is the volume of the packet, and M_{fuel} is the molar weight of the fuel.

The following can be used for in-cylinder pressure and temperature calculation [81].

For the closed system, the differential energy equation can be presented as

$$\delta Q - \delta W = dU \qquad \text{Eq. 4.66}$$

Since $\delta W = PdV$ and $dU = mc_v dT$,

$$\delta Q - PdV = mc_v dT \qquad \text{Eq. 4.67}$$

Assuming ideal gas behavior and using the ideal gas equation

$$mdT = \frac{1}{R}(PdV + VdP) \qquad \text{Eq. 4.68}$$

Therefore,

$$\delta Q - PdV = \frac{c_v}{R}(PdV + VdP) \qquad \text{Eq. 4.69}$$

$$Q_{in}\frac{dx}{dt} - P\frac{dV}{dt} = \frac{c_v}{R}\left(P\frac{dV}{dt} + V\frac{dP}{dt}\right) \qquad \text{Eq. 4.70}$$

Solving for P,

$$\frac{dP}{dt} = -\gamma\frac{P}{V}\frac{dV}{dt} + (\gamma - 1)\frac{Q_{in}}{V}\frac{dx}{dt} \qquad \text{Eq. 4.71}$$

Where, P is pressure, V is cylinder volume, γ is specific heat ratio, R is gas constant, c_v is specific heat, Q_{in} is total heat input, and x is normalized cumulative heat release.

In-cylinder pressure at each time step can be calculated by solving this first-order differential equation. γ is also evaluated by gas composition and temperature, and the volume change rate, dV/dt can be analytically obtained using engine geometry information. Pressure is uniform throughout the zone. The heat release rate, dx/dt, can be imposed using heat release models. The heat loss to the wall can be included in this equation if needed.

Using energy conservation equation, the temperature of the cylinder, T, can be obtained as

$$\dot{T} = \frac{B'}{A'}\left[\frac{\dot{m}}{m}\left(1 - \frac{h}{B'}\right) - \frac{\dot{V}}{V} - \frac{C'}{B'}\dot{\phi} + \frac{1}{B'm}\left(\sum_j \dot{m}_j h_j - \dot{Q}_w\right)\right] \qquad \text{Eq. 4.72}$$

Where,

$$A' = \frac{\partial h}{\partial T} + \frac{\partial \rho/\partial T}{\partial \rho/\partial p}\left(\frac{1}{\rho} - \frac{\partial h}{\partial p}\right) \qquad \text{Eq. 4.73}$$

$$B' = \frac{1 - \rho(\partial h/\partial p)}{\partial \rho \,/\, \partial p}, and\ C' = \frac{\partial h}{\partial \phi} + \frac{\partial \rho/\partial \phi}{\partial \rho/\partial p}\left(\frac{1}{\rho} - \frac{\partial h}{\partial p}\right) \qquad \text{Eq. 4.74}$$

m is mass, $\dot{m}$ is changes in mass, h is specific enthalpy, V is volume, $\dot{Q}_w$ is the total heat transfer rate into the control volume, ϕ is equivalence ratio, and $\dot{m}_j h_j$ represents enthalpy transfer into the volume [81].

It should be stated that the above equations can be simplified for certain conditions. For example, during compression stroke, the effects of dissociation terms $\partial u/\partial p\,, \partial h/\partial p\,, and\ \partial R/\partial p$ can be ignored. A detailed flowchart of the GCI combustion model, including main variables and equations, is presented in Figure 54.

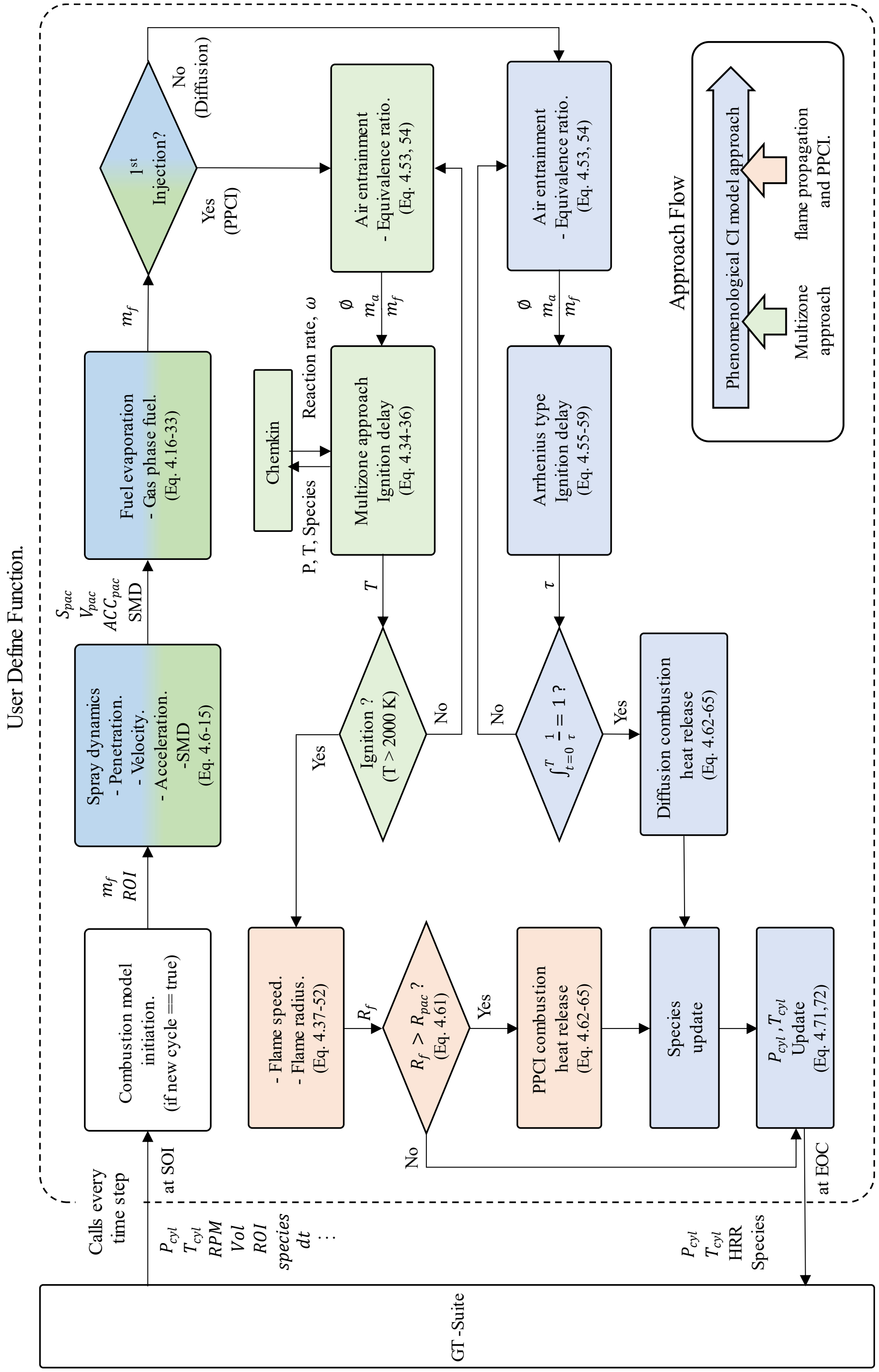

Figure 54 A detailed flowchart of GCI model.

4.4 Quasi-Dimensional GCI Combustion Model Validation and Results

This section presents the prediction results from the developed PPCI and diffusion combustion model under the operating conditions employed for CFD simulation, including different TIVC, PIVC, and EGR rates.

Model Validation Against Testing Results

The developed phenomenological combustion model was first validated against the available GCI engine testing results. As shown in Figure 55 and Figure 56, the in-cylinder pressure predicted by the model showed good agreement with experimental data at two operating conditions. It was observed that the PPCI combustion, represented by the first peak of the heat release of GCI combustion, was successfully captured with minor variation. The CA10, at which the burned fraction is 10 % of the total fuel, and CA50, 50 % of the total burned fuel, showed reasonable agreement. The differences between the simulated CA10 and CA50 with experimental data were about 2 °CA. However, the diffusion combustion, indicated by the second peak of the heat release, was overpredicted in the 2000 rpm 12 bar IMEP condition. In contrast, the 2250 rpm 18 bar IMEP condition revealed good validation results against testing results. It was identified that the final stage of oxidation was underpredicted for both cases. Due to the elevated thermal condition in the cylinder, unburned fuel and intermediate species such as CO constantly oxidized during the expansion stroke.

The underprediction during expansion stroke can be seen as a limitation of the developed combustion model due to the fact that only the fuel cloud was considered in heat release, and the overly lean air-fuel mixture and intermediate species throughout the cylinder were not considered in heat release calculation. As a result, CA90, at which the burned fraction is 90 % of the total fuel, showed some discrepancy, and the predicted peak cylinder pressure was lower than in the experimental data.

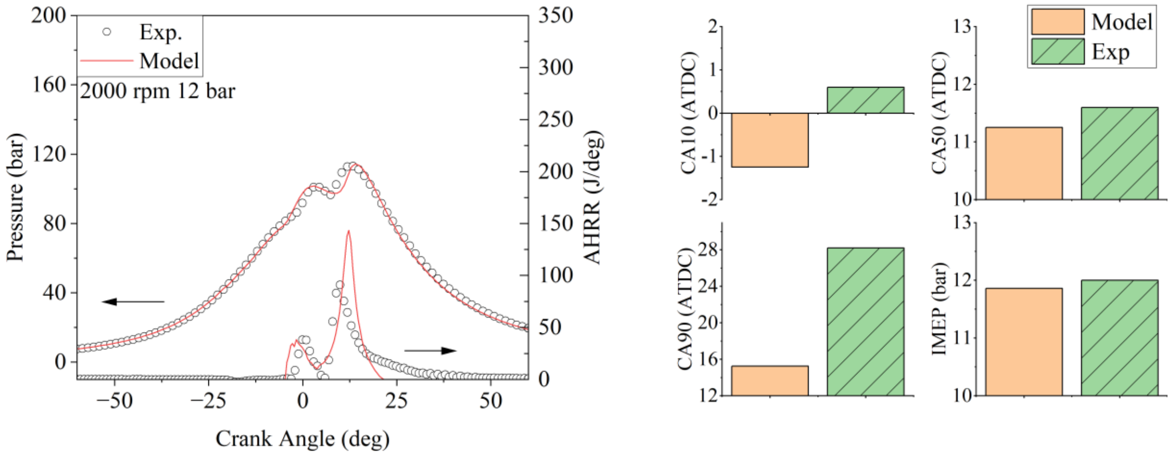

Figure 55 GCI model validation against experimental data at 2000 rpm, 12 bar IMEP

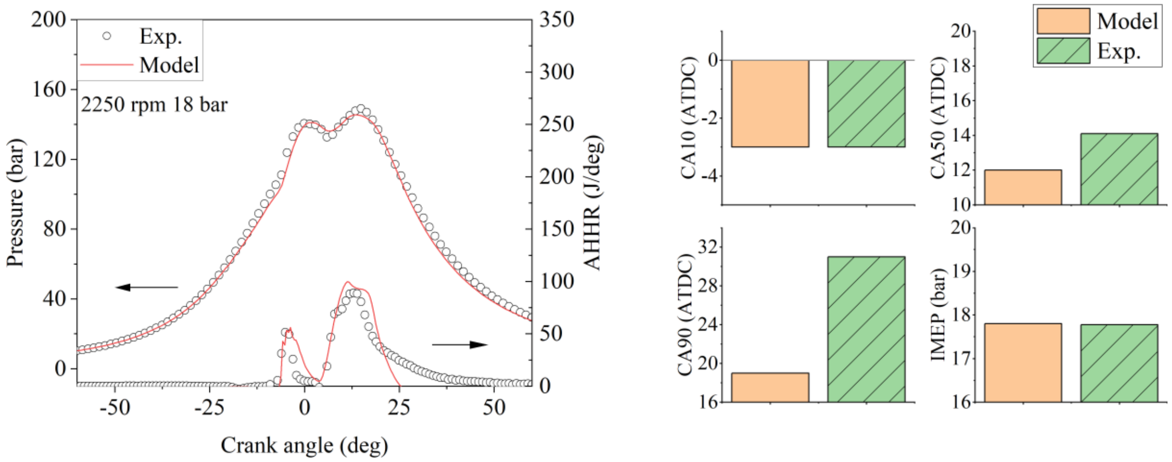

Figure 56 GCI model validation results against experimental data at 2250 rpm, 18 bar IMEP

Using this validated model, the effects of thermal conditions, including temperature, pressure, and EGR rate at IVC, on combustion were investigated in the following section. Due to the limited testing results available, CFD simulation results were referenced to evaluate the quasi-dimensional GCI model prediction result and fidelity in the following sections. In this section, the impact of intake temperature, pressure, and EGR rate on GCI combustion was numerically simulated using the CFD model and GCI model developed in this research.

Intake Temperature Variation

One of the main challenges in GCI combustion is minimizing the incomplete combustion or misfire of GCI engines under low load conditions and cold start operations due to the lower reactivity, high fuel latent heat, and low engine operation temperature. Consequently, it is necessary for the combustion model to estimate not only the successful combustion process under warmed-up conditions but also incomplete combustion behavior under thermally undesired conditions. To promote the chemical reaction and auto ignition of the fuel by overcoming activation energy effectively, different levels of temperatures at IVC were considered in this study to examine the combustion characteristics. It should be noted that various system-level approaches, such as an electric heater and valvetrain actuation, can be utilized to realize the higher temperature in-cylinder ambient conditions. The effects of temperatures on GCI combustion are presented in Figure 57, Figure 58, and Figure 59, as well as Table 10, Table 11, and Table 12.

In this study, 360 K, 380 K, and 400 K were imposed as initial conditions at IVC for 1250 rpm 3 bar IMEP. These temperatures are significantly higher than that in the intake manifold due to the heat convection from the hot cylinder wall, intake heating, and the residual gas fraction. As shown in Figure 57, higher temperatures resulted in higher and more advanced development in-cylinder pressure and heat release. The higher temperature of the air-fuel mixture effectively promoted the chemical reactions and showed pronounced combustion behavior. Moreover, it was clearly observed that the GCI combustion under a lower initial temperature (360 K) showed abnormal combustion (misfire and incomplete combustion), whereas the 400 K case showed an active combustion process. The 360 K case showed ~ 2 bar IMEP, much lower than the other two cases because of the misfire. Overall, the peak heat release of the developed model was underestimated compared to CFD results. Summary of engine performance from the developed model and CFD simulation are listed in Table 10.

The PPCI combustion was also generally promoted under 2000 rpm 12 bar IMEP conditions and 2250 rpm 18 bar IMEP conditions with higher temperatures. The hotter in-cylinder gas promoted the chemical kinetics during PPCI, showing higher heat release and in-cylinder pressure. It was also observed that the second peak of the heat release was lower when the temperature at IVC was higher. This is because more combustion products were attained during the first heat release of PPCI when the initial gas temperature was higher, and they diluted the air-fuel charge and mitigated rapid heat release during the second stage heat release. In addition, the more fuel participated in the PPCI combustion with higher temperature, consequently, the less unburned fuel participated in the diffusion combustion. Nevertheless, the ignition delay was advanced owing to the promoted in-cylinder gas temperature when the second injection occurred. A summary of engine performance from the developed model and CFD simulation is listed in Table 11 and Table 12. It can be concluded that overall model predictions were reasonable compared to engine test data and CFD, although the tail of the heat release was underpredicted, as indicated in CA90. The average discrepancy of CA10, CA 50, CA 90, and IMEP across operating conditions with different TIVC in this study were about 2.9 deg, 1.9 deg, 6.6 deg, and 0.4 bar.

It is evident that the GCI combustion model can be used to replace the CFD model in GCI simulation. The integration of the GCI model into the GT-suite will enable the simulation of the GCI engine system operated under transient conditions, as opposed to CFD simulations.

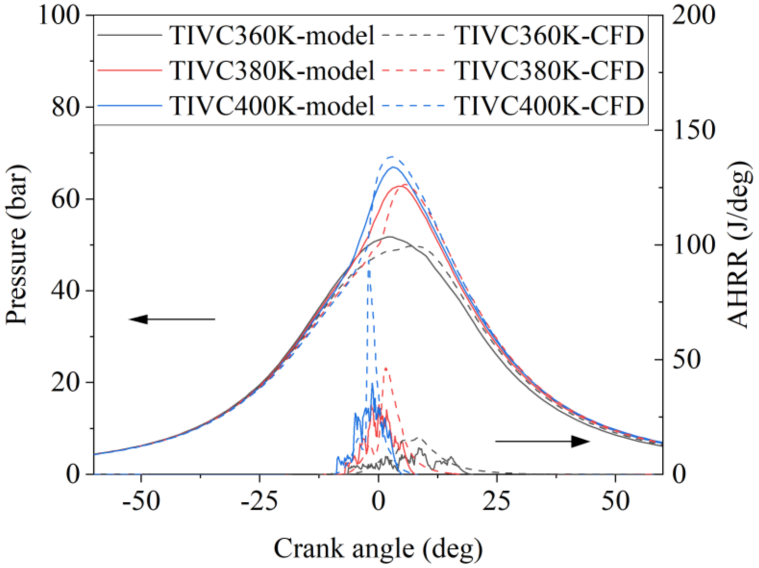

Figure 57 Validation of GCI model against CFD simulation data at 360, 380, and 400 K at IVC at 1250 rpm and 3 bar IMEP.

Table 10 Summary of TIVC impact on GCI combustion characteristics simulated by GCI model and CFD model at 1250 rpm 3 bar IMEP.

TIVC, K	Parameters	GCI Model, ˚CA ATDC	CFD, ˚CA ATDC	|Diff|
360	CA10	-4.1	1.1	5.2
	CA50	4.7	8.5	3.8
	CA90	12.3	18.7	6.4
	IMEP	2.0	2.2	0.2
380	CA10	-5.1	-1.5	3.6
	CA50	-1.5	2.7	4.2
	CA90	1.9	9.2	7.3
	IMEP	2.7	2.9	0.2
400	CA10	-6.9	-3.9	3.0
	CA50	-3.1	-1.1	2.0
	CA90	-0.1	3.3	3.31
	IMEP	2.9	2.9	0.0

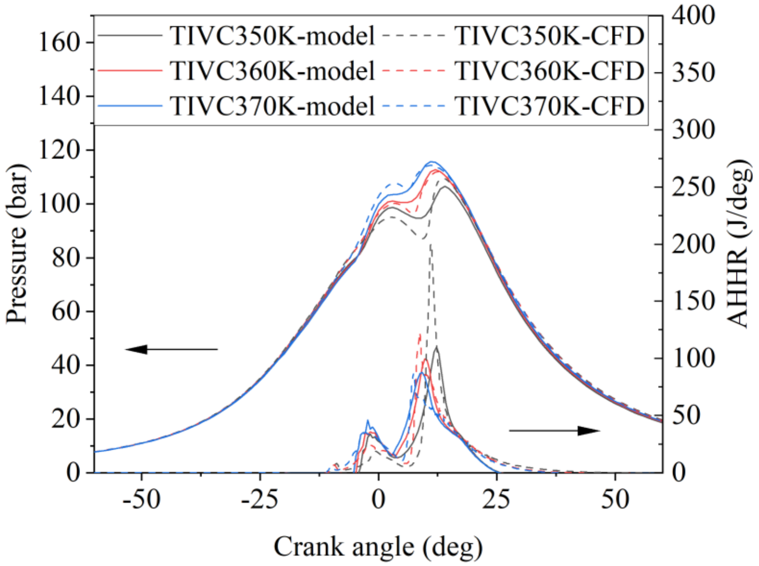

Figure 58 Validation of GCI model against CFD simulation data at 350, 360, and 370 K at IVC at 2000 rpm and 12 bar IMEP.

Table 11 Summary of TIVC impact on GCI combustion characteristics simulated by GCI model and CFD model at 2000 rpm 12 bar IMEP.

TIVC, K	Parameters	GCI Model, ˚CA ATDC	CFD, ˚CA ATDC	|Diff|
350	CA10	-0.25	2.9	3.2
	CA50	14.25	12.4	1.9
	CA90	16.75	25.1	8.4
	IMEP	11.2	11.4	0.2
360	CA10	-1.25	0.01	1.3
	CA50	11.25	11.3	0.1
	CA90	15.25	22.8	7.6
	IMEP	11.9	11.5	0.4
370	CA10	-1.25	-2.15	0.9
	CA50	9.75	10.4	0.7
	CA90	15.25	22.1	6.9
	IMEP	12.4	11.6	0.8

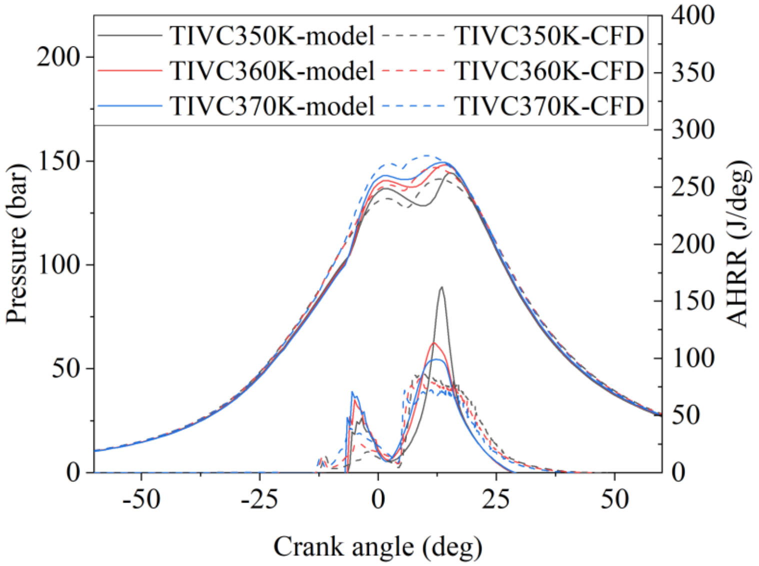

Figure 59 Validation of GCI model against CFD simulation data at 350, 360, and 370 K at IVC at 2250 rpm and 18 bar IMEP.

Table 12 Summary of TIVC impact on GCI combustion characteristics simulated by GCI model and CFD model at 2250 rpm 18 bar IMEP.

TIVC, K	Parameters	GCI Model, ˚CA ATDC	CFD, ˚CA ATDC	|Diff|
350	CA10	-2.0	4.7	6.7
	CA50	13.0	14.1	1.1
	CA90	19.5	25.7	6.2
	IMEP	17.0	16.7	0.3
360	CA10	-3.0	-0.5	2.5
	CA50	11.0	13.1	2.1
	CA90	18.5	25.0	6.5
	IMEP	17.63	16.9	0.73
370	CA10	-4.0	-3.8	0.2
	CA50	10.5	12.1	1.6
	CA90	17.5	24.2	6.7
	IMEP	17.9	16.9	1

Intake Pressure Variation

Intake pressure is also examined because it is related to overall thermal efficiency, turbocharging system, and pumping loss. In particular, pumping and friction loss under low load conditions play a significant role while evaluating the entire engine system due to relatively lower gross work from combustion. In this study, the amount of fuel injected into the cylinder was maintained constant while the intake pressure was varied. The effects of different intake pressures at IVC on combustion characteristics are shown in Figure 60, Figure 61, and Figure 62, and a summary is listed in Table 13, Table 14, and Table 15.

For the 1250 rpm 3 bar IMEP condition, the in-cylinder pressure from the model and CFD showed reasonable agreement with advanced ignition as indicated by CA10. Higher intake pressure at IVC strongly influences charge temperature, resulting in a faster ignition start due to the enhanced chemical kinetics. At 2000 rpm 12 bar IMEP, where a split injection strategy was employed, PPCI and diffusion combustions were comparable with each other. Even though the early stage of PPCI, representing low-temperature combustion, was not effectively shown in the developed model, the peak heat release of PPCI was generally well-matched, and the diffusion combustion also showed reasonable accuracy. A similar trend was observed for the 2250 rpm 18 bar IMEP case as in the previous cases. It is evident that the GCI model and CFD presented reasonable agreements.

It can be concluded that the overall combustion process was not significantly affected by the different pressure levels at IVC timing, as shown in the heat release rate in Figure 60, Figure 61, and Figure 62. However, the high level of pressure increased charge temperature during compression stroke due to the increased charge density. Consequently, the increased temperature advanced PPCI combustion slightly up to 2 ˚CA based on model prediction. With marginal discrepancy, model prediction and CFD results agreed well with the range of pressure variation simulated in this study.

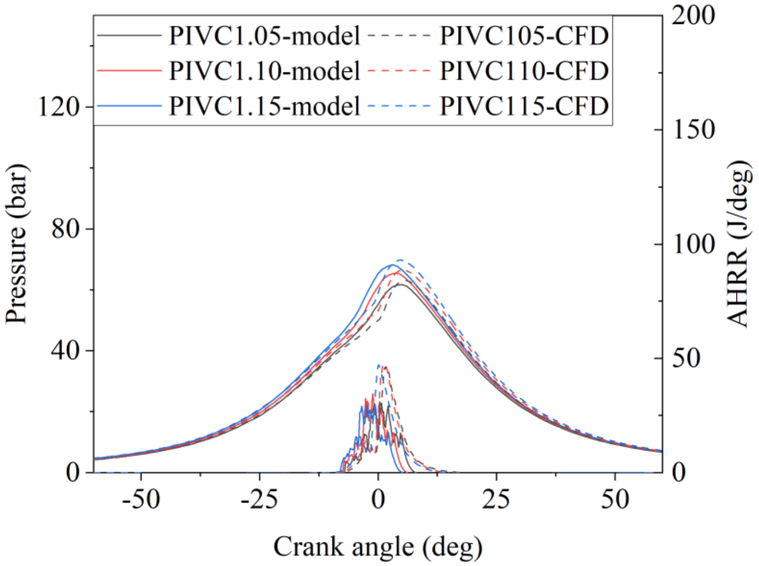

Figure 60 Validation of GCI model against CFD simulation data at 1.05, 1.1, and 1.15 bar at IVC at 1250 rpm and 3 bar IMEP, TIVC 380 K.

Table 13 Summary of PIVC impact on GCI combustion characteristics simulated by GCI model and CFD model at 1250 rpm 3 bar IMEP.

PIVC, bar	Parameters	GCI Model, ˚CA ATDC	CFD, ˚CA ATDC	|Diff|
1.05	CA10	-4.1	-1.4	2.7
	CA50	0.1	2.7	2.6
	CA90	3.9	9.2	5.3
	IMEP	2.7	2.88	0.18
1.10	CA10	-5.1	-2.3	2.8
	CA50	-1.3	2.2	3.5
	CA90	2.5	8.1	5.6
	IMEP	2.64	2.90	0.26
1.15	CA10	-6.1	-3.1	3.0
	CA50	-2.5	1.3	3.8
	CA90	1.5	7.4	5.9
	IMEP	2.55	2.91	0.36

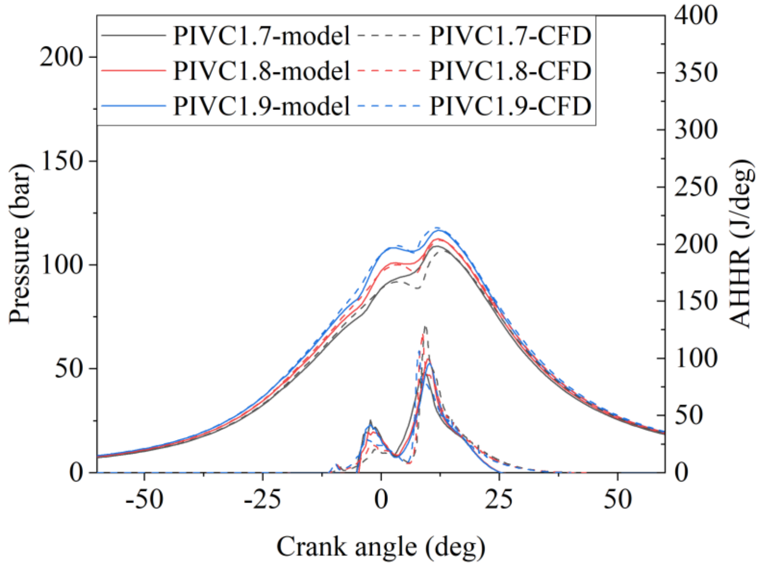

Figure 61 Validation of GCI model against CFD simulation data at 1.7, 1.8, and 1.9 bar at IVC at 2000 rpm and 12 bar IMEP, TIVC 360 K.

Table 14 Summary of PIVC impact on GCI combustion characteristics simulated by GCI model and CFD model at 2000 rpm 12 bar IMEP.

PIVC, bar	Parameters	GCI Model, ˚CA ATDC	CFD, ˚CA ATDC	|Diff|
1.7	CA10	0.25	1.6	1.35
	CA50	9.75	11.8	2.05
	CA90	17.75	23.5	5.75
	IMEP	11.8	11.5	0.30
1.8	CA10	-0.75	0.01	0.76
	CA50	9.75	11.3	1.55
	CA90	17.75	22.8	5.05
	IMEP	11.85	11.5	0.35
1.9	CA10	-1.75	-1.5	0.25
	CA50	9.75	10.7	0.95
	CA90	17.75	22.2	4.45
	IMEP	12.0	11.7	0.30

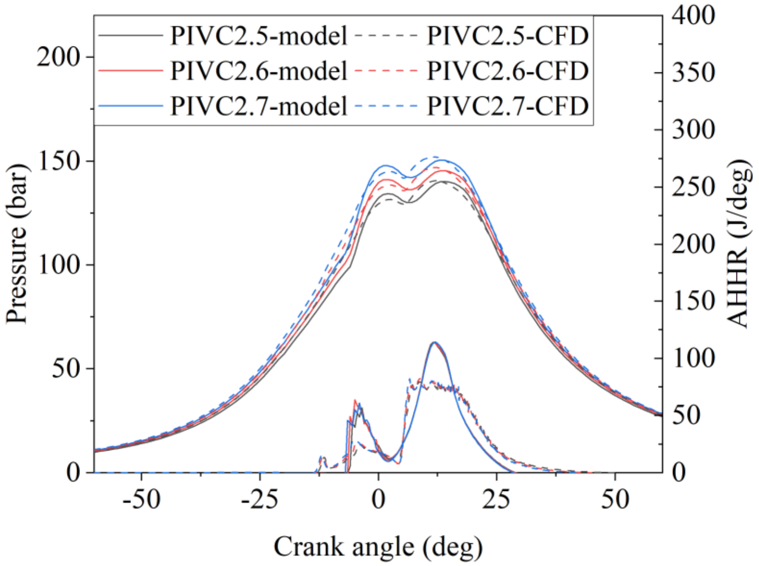

Figure 62 Validation of GCI model against CFD simulation data at 2.5, 2.6, and 2.7 bar at IVC at 2250 rpm and 18 bar IMEP, TIVC 360 K.

Table 15 Summary of PIVC impact on GCI combustion characteristics simulated by GCI model and CFD model at 2250 rpm 18 bar IMEP.

PIVC, bar	Parameters	GCI Model, ˚CA ATDC	CFD, ˚CA ATDC	|Diff|
2.5	CA10	-2.5	0.5	3.0
	CA50	11.5	13.4	1.9
	CA90	18.5	26.1	7.6
	IMEP	17.3	16.7	0.6
2.6	CA10	-3.5	-0.5	3.0
	CA50	11.0	13.1	2.1
	CA90	18.5	25.0	6.5
	IMEP	17.6	16.9	0.7
2.7	CA10	-3.5	-1.3	2.2
	CA50	11.0	13.0	2.0
	CA90	18.0	24.2	6.2
	IMEP	17.8	17.0	0.8

EGR Rate Variation

This study explored the effects of 20 %, 30 %, and 40 % of EGR on GCI combustion at 1250 rpm and 3 bar IMEP operating conditions. It is common that more than 50 % of the dilution level can be utilized with thermally elevated conditions at low load conditions to control the rapid auto-ignition combustion process and provide adequate energy for combustion stability because of the lower reactivity and high latent heat of the fuel. However, up to 40 % of EGR was simulated in this study to achieve stable and healthy combustion. It should be mentioned that various EGR levels in this study mean the total amount of residual gas, accounting for both external EGR and internal EGR during the gas exchange process. Also, the single-cylinder GT model used in this study was built for demonstration purposes; thus, 40 % of EGR was not achievable due to the rack of the turbine, which restricts gas flow and drives EGR flow. Up to 35% of EGR was employed instead. The effects of different levels of EGR on the combustion process were plotted in Figure 63, Figure 64, and Figure 65 and the summary is listed in Table 16, Table 17, and Table 18.

At 1250 rpm 3 bar IMEP, model prediction showed reasonable agreement with CFD results. The peak heat release predicted by the GCI model was lower and more advanced when compared with the CFD model. The average absolute discrepancy in CA10 and CA50 across the cases was less than 3 CAD, and the average IMEP gap was about 0.2 bar.

For 2000 rpm 12 bar IMEP and 2250 rpm 18 bar IMEP cases, it was clearly seen that the higher level of EGR showed effective mitigation in rapid combustion, causing lower heat release and pressure rise rate during PPCI combustion as the EGR rate increased. For the second heat release represented by diffusion combustion, the higher level of EGR at IVC revealed a higher peak of heat release because of the unburned fuel left from the weak PPCI combustion, contributing to fewer combustion products during diffusion combustion. The average IMEP variations between the model and CFD at each operating condition were 0.5 and 0.7 bar, respectively. For CA50, the average gap was 1.35 CAD and 1.9 CAD, which is relatively small.

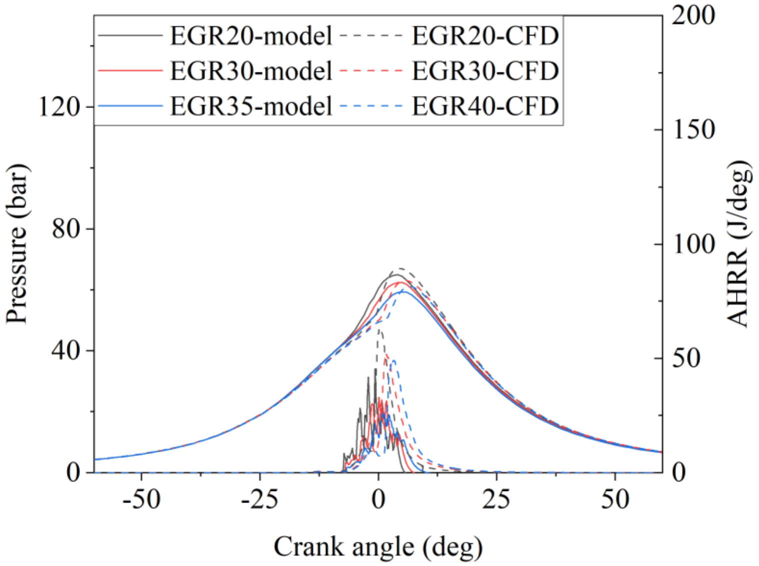

Figure 63 Validation of GCI model against CFD simulation data with EGR 20, 30, and 40 % at IVC at 1250 rpm 3 bar IMEP, TIVC 380 K.

Table 16 Summary of EGR impact on GCI combustion characteristics simulated by GCI model and CFD model at 1250 rpm 3 bar IMEP.

EGR, %	Parameters	GCI Model, ˚CA ATDC	CFD, ˚CA ATDC	|Diff|
20	CA10	-4.9	-2.5	2.4
	CA50	-1.1	1.2	2.3
	CA90	2.7	6.2	3.5
	IMEP	2.8	2.95	0.15
30	CA10	-4.3	-1.4	2.9
	CA50	-0.1	2.7	2.8
	CA90	3.5	9.2	5.7
	IMEP	2.7	2.88	0.18
35/40	CA10	-4.1	-1.1	3.0
	CA50	0.5	4.0	3.5
	CA90	4.5	10.4	5.9
	IMEP	2.5	2.86	0.36

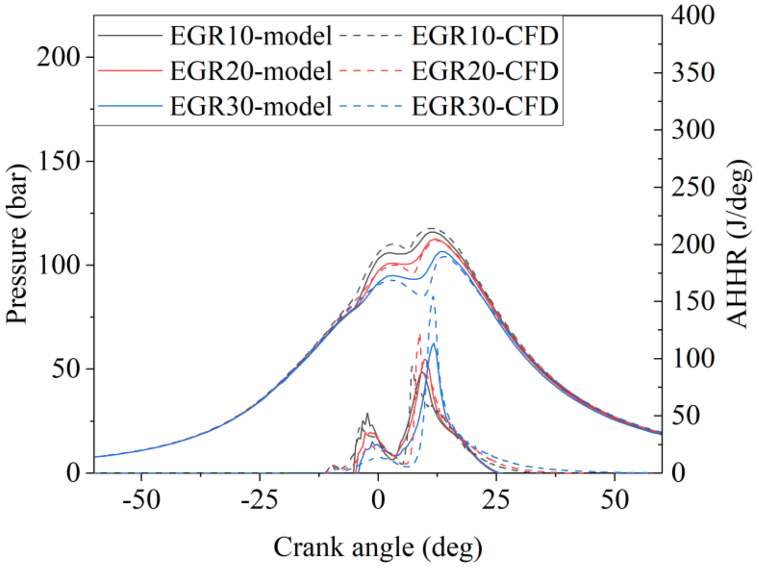

Figure 64 Validation of GCI model against CFD simulation data with EGR 10, 20, and 30 % at IVC at 2000 rpm 12 bar IMEP, TIVC 360 K.

Table 17 Summary of EGR impact on GCI combustion characteristics simulated by GCI model and CFD model at 2000 rpm 12 bar IMEP.

EGR, %	Parameters	GCI Model, ˚CA ATDC	CFD, ˚CA ATDC	|Diff|
10	CA10	-2.25	-2.6	0.35
	CA50	9.25	10.0	0.75
	CA90	17.75	20.6	2.85
	IMEP	12.26	11.7	0.56
20	CA10	-0.75	0.01	0.76
	CA50	9.75	11.3	1.55
	CA90	17.75	22.8	5.05
	IMEP	11.85	11.5	0.35
30	CA10	0.75	3.4	2.65
	CA50	11.25	13.0	1.75
	CA90	18.25	28.0	9.75
	IMEP	11.2	11.2	0.0

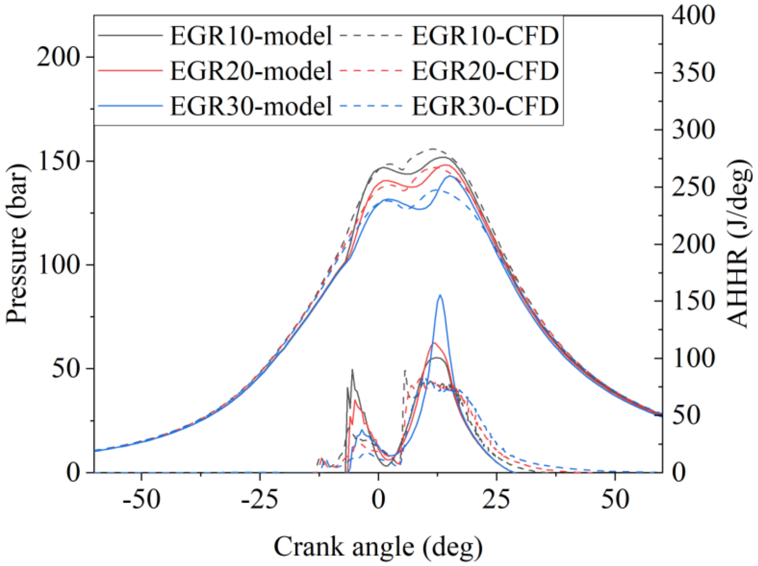

Figure 65 Validation of GCI model against CFD simulation data with EGR 10, 20, and 30 % at IVC at 2250 rpm 18 bar IMEP, 360 K.

Table 18 Summary of EGR impact on GCI combustion characteristics simulated by GCI model and CFD model at 2250 rpm 18bar IMEP.

EGR, %	Parameters	GCI Model, ˚CA ATDC	CFD, ˚CA ATDC	|Diff|
10	CA10	-4.5	-3.3	1.2
	CA50	10.5	11.8	1.3
	CA90	17.5	22.5	5.0
	IMEP	18.1	17.1	1.0
20	CA10	-3.5	-0.5	3.0
	CA50	11.0	13.1	2.1
	CA90	18.5	25.0	6.5
	IMEP	17.6	16.8	0.8
30	CA10	-1.0	3.8	4.8
	CA50	12.5	14.9	2.4
	CA90	19.0	29.1	10.1
	IMEP	16.8	16.4	0.4

4.5 Summary

In this chapter, the development of a quasi-dimensional phenomenological PPCI-diffusion combustion model was presented. The model was developed and improved from the traditional spray model. For the spray sub-model, the penetration length of the gasoline spray was validated against a high-pressure gasoline injection test under vaporizing conditions (>850 K). In addition, variable injection pressure was considered to realize the fuel distribution within the fuel “cloud”. CFD spray simulation results were used to support the development of the spray model. It was observed from the CFD analysis that a high concentration of the fuel was exhibited at the tip of the spray, and this phenomenon was well captured by the improved spray model by considering ramp-up and ramp-down periods during injection.

For the PPCI diffusion combustion model, phenomenological SI and CI models with modifications were employed as a base framework, and an additional multizone model approach was adapted for ignition delay calculation during PPCI combustion. In the combustion model, spray dynamics, air mass entrainment, ignition delay, and heat release were calculated at each time step, and typical Arrhenius form ignition delay was employed for diffusion combustion.

The quasi-dimensional GCI combustion model was validated against experimental data and CFD simulation data when experimental data was unavailable. For low load, misfire was also captured with lower TIVC. Thus, one of the main concerns in GCI combustion was also addressed in this model. To evaluate the developed model, CA10, CA50, and CA90 were compared with CFD results, and CA10 and CA50 showed less than 5 ˚CA discrepancy. It can be concluded that the GCI combustion model developed in this study is able to capture the GCI combustion characteristics comparable to CFD results but takes less computational time.

Chapter 5. GCI Combustion Model Application in a System-Level Simulation

5.1 1D GT Model Description

This chapter demonstrates the application of the GCI model in a system-level analysis using a variable valvetrain system as an example. GT-Suite was utilized as a platform. Figure 66 presents the engine system model developed using GT-Suite. This model was modified and simplified from a full-scale diesel engine system. This simplified model contains one single cylinder, intake/exhaust manifolds, valves, HP-EGR, EGR controller, and crankcase, as denoted as boxes in Figure 66. The inlet and outlet conditions were maintained at a constant level for simplicity in simulating upstream of intake and exhaust manifold conditions.

The PCCI-diffusion GCI combustion model developed in Chapter 4 was implemented into GT-Suite. This combustion model is used to simulate a closed cycle from the intake valve closing to the exhaust valve opening period, including the fuel injection, spray development, fuel evaporation, mixing, and combustion. The standard GT-Suite model was used during gas exchange. The valve timing and lift were adapted and implemented based on the base diesel engine. It should be noted that this model can be extended to a full-scale engine system with multiple cylinders, a turbocharger, an EGR system, a charge cooler, and an aftertreatment system.

In this study, 1250 rpm 3 bar IMEP low-load operating condition was considered to investigate the effects of variable valve actuation on the combustion characteristics. A single injection strategy was employed at -28 °CA ATDC, and the external EGR was intentionally not utilized to have this research focused on dilution level changes with various valvetrain strategies. The in-cylinder pressure and temperatures at IVC were kept at 1.05 bar and 340 K, respectively, which showed in-complete combustion with a 30 % EGR rate, as shown in the previous chapter. The exhaust pressure and temperature were at 1.1 bar and 500 K to mimic the condition at the exhaust manifold. The detailed operating condition is listed in Table 19.

Table 19 Low-load engine operating condition simulated in this chapter

Engine speed [rpm]	1250
Engine load, IMEP [bar]	3
Intake manifold pressure [bar]	1.05
Intake manifold temperature [K]	360
Exhaust manifold pressure [bar]	1.1
Exhaust manifold temperature [K]	500
Injection timing [˚CA ATDC]	-28
Injection pressure [bar]	200
Injection quantity [mg]	8
External EGR rate [%]	0

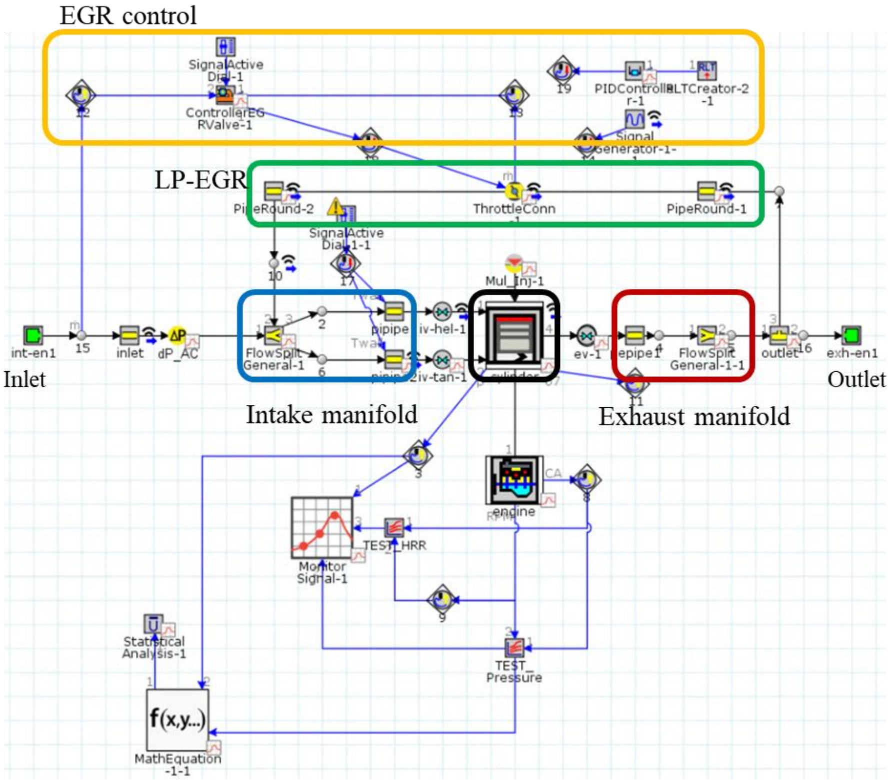

Figure 66 A single cylinder engine GT model with sub-systems.

5.2 Variable Valve Actuation Strategy

As discussed in the previous chapter, in-cylinder thermal conditions play a significant role in GCI combustion at low-load operation, as cold in-cylinder thermal conditions can cause incomplete combustion. Several strategies, such as an electric intake air heater, VVA, and back pressure valve, have been proposed [86] to effectively promote the in-cylinder thermal energy and exhaust gas temperature for the fast warm-up of the aftertreatment system downstream and control of GCI combustion. Variable valvetrain strategies, including variable valve timing and exhaust gas rebreathing strategies, were considered to examine the effect of the gas exchange process on the in-cylinder thermal condition using a simple single-cylinder model. Although the effects of the interaction between the air boosting system and valvetrain system may not be reflected in this study due to the lack of a turbocharger system in the current model, the purpose of this chapter is to demonstrate the ability of the developed GCI combustion model in engine system simulation when integrated into a system level tool with valvetrain system. The strategies considered in this chapter are briefly described as follows.

Early exhaust valve opening (EEVO) or late exhaust valve opening (LEVO) strategies are to advance or retard the exhaust valve open/closing event, allowing the exhaust gas to exit the cylinder earlier or later than base timing. In this demonstration, ± 20 ˚CA of shifting from the base timing listed in Table 1 was employed for EEVO and LEVO. EEVO strategy ensures higher thermal energy content of the gas, which will promote faster light-off time of downstream aftertreatment system at the cost of gross indicated work. In addition, the early closing timing can cause recompression of the cylinder, resulting in higher pumping losses. For the LEVO strategy, the expansion of the piston is maximized by opening the exhaust valve late, and the gross work is expected to increase. However, the downstream gas temperature will lose thermal energy during expansion cooling. The valve timings and lifts considered in this study are shown in Figure 67 (a).

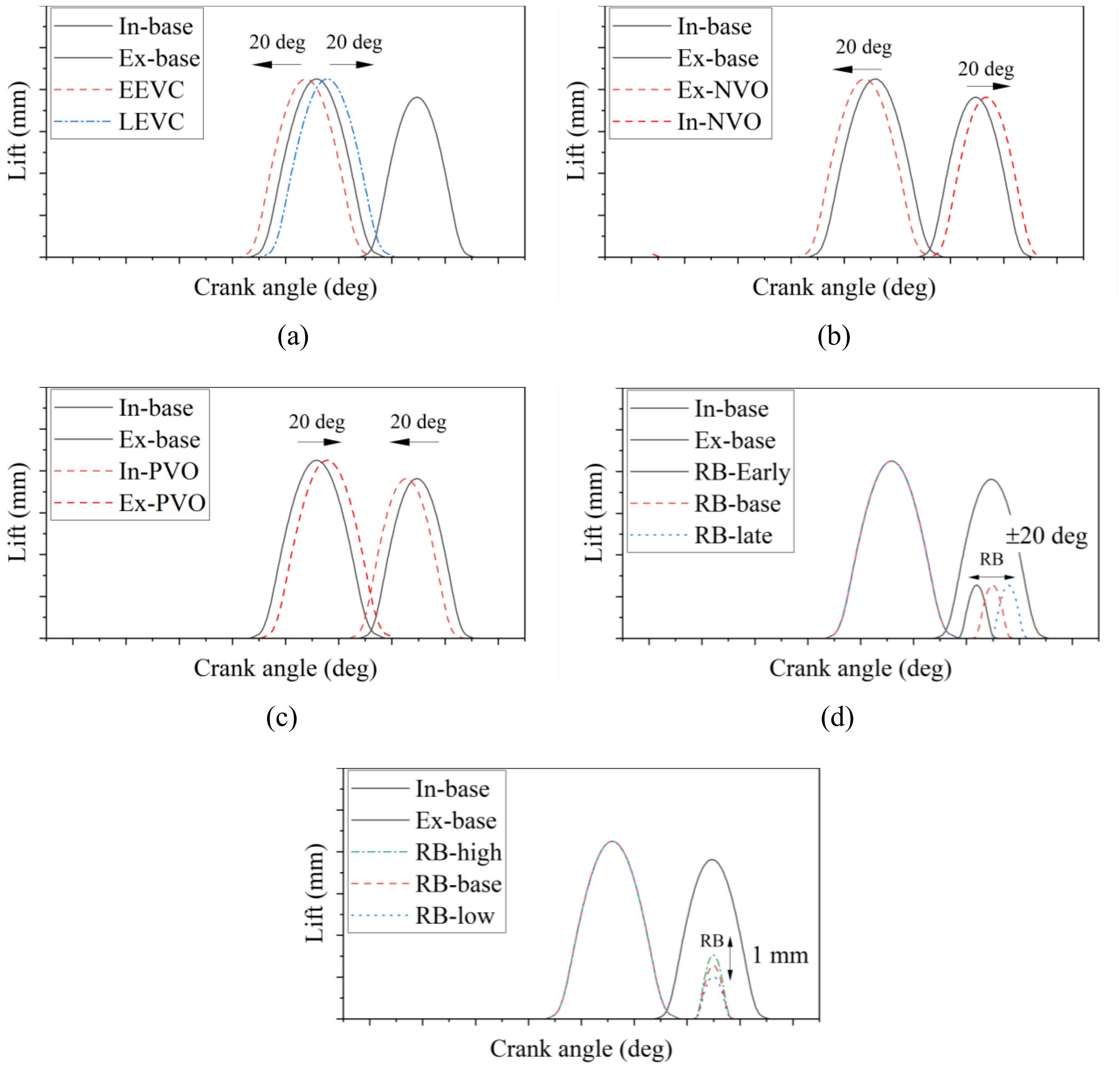

(a) (b) (c) (d) (e)

Figure 67 Variable valve actuation strategies simulated in this study: (a) EEVC and LEVC, (b) NVO, (c) PVO, (d) exhaust rebreathing with timings, and (e) exhaust rebreathing with variable lifts.

The negative valve overlap (NVO) strategy can be seen as an extension of EEVO with retarded intake valve opening (20 ˚CA) from the base timing. A similar level of trapped gas in the cylinder is expected to be retained as EEVO with less pumping loss with optimized valve phasing. In addition, NVO features a recompression period due to the early and late timings of the exhaust valve open and intake valve open. The valve timing and lift of NVO are shown in Figure 67 (b).

Positive valve overlap (PVO) is the opposite concept of NVO, indicating that the valve overlap is more pronounced than the base timing. PVO is realized in this study by retarding the exhaust and advancing the intake valve timing (± 20 ˚CA) from the base timing. Therefore, an increased amount of exhaust gas trapped in the cylinder is expected. The valve timing and lift of PVO are presented in Figure 67 (c).

Exhaust gas rebreathing (RB) is re-introducing hot exhaust gas into the cylinder by opening the exhaust valve a second time during intake stroke. The downward piston motion during the intake stroke creates negative pressure in the cylinder, and the second exhaust valve opening event induces a reverse flow of exhaust gas from the exhaust manifold. The valve timing and lift of RB considered in this study (± 20 ˚CA and up to 1 mm lift difference) are presented in Figure 67 (d) and (e).

The mass flow through the exhaust and intake valves is presented in Figure 68 to Figure 74. Due to the advanced valve phasing of EEVC, the valve overlap period was not pronounced, whereas LEVC showed greater valve overlap with fixed intake valve timing. Additionally, retarded exhaust valve timing also contributed to the re-introduced residual gas from the exhaust gas manifold due to the downward piston movement. The higher level of the reintroduced hot gas contributed to the higher level of burned mass fraction and temperature at IVC. However, the effectiveness of the EEVO and LEVO in improving the thermal condition was not significant.

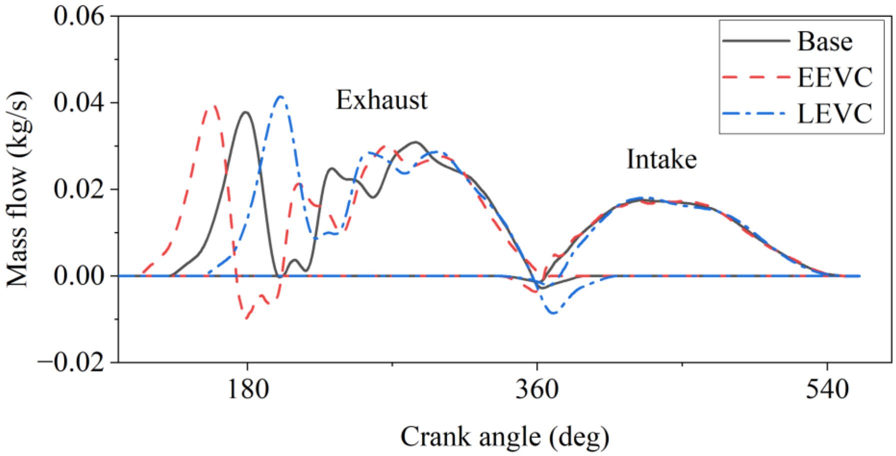

Figure 68 Exhaust and intake mass flow rate with EEVC and LEVC strategy.

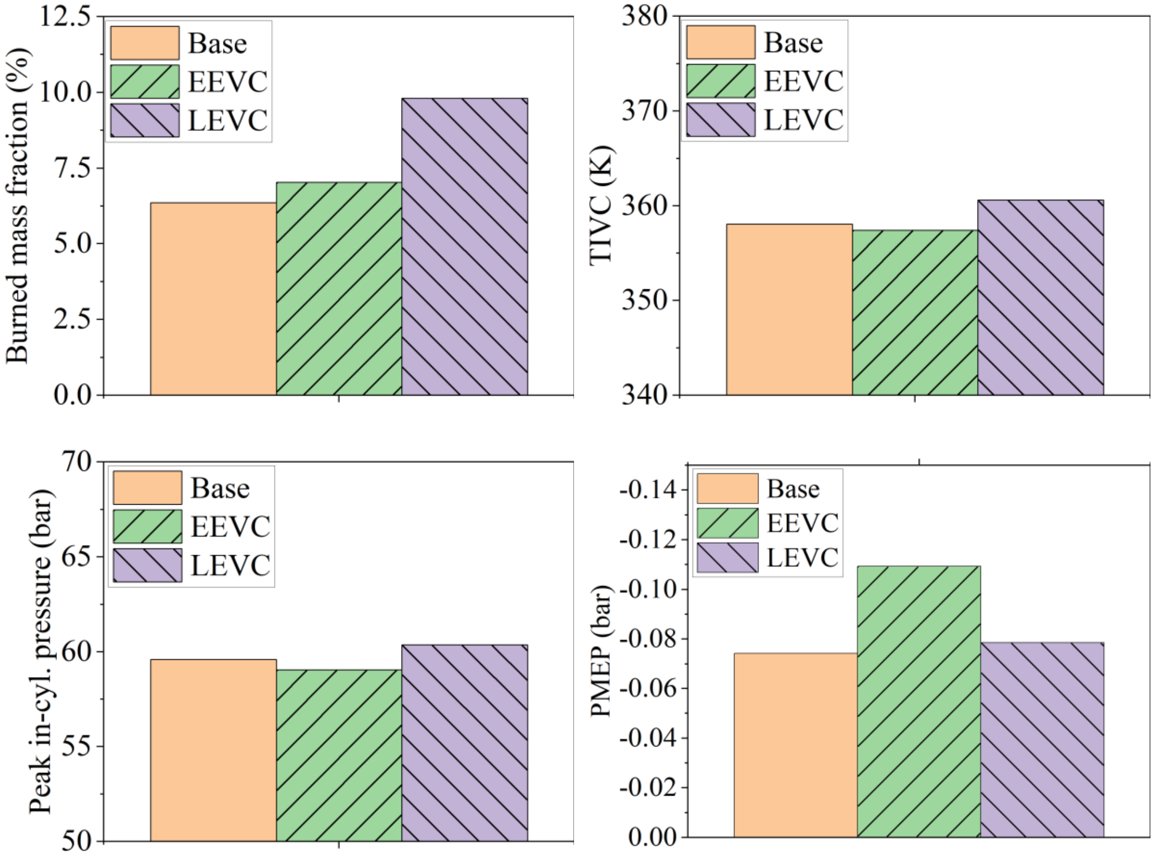

Figure 69 Comparison of burned mass fraction, temperature at IVC, peak in-cylinder pressure, and PMEP with base/EEVC/LEVC valve strategies.

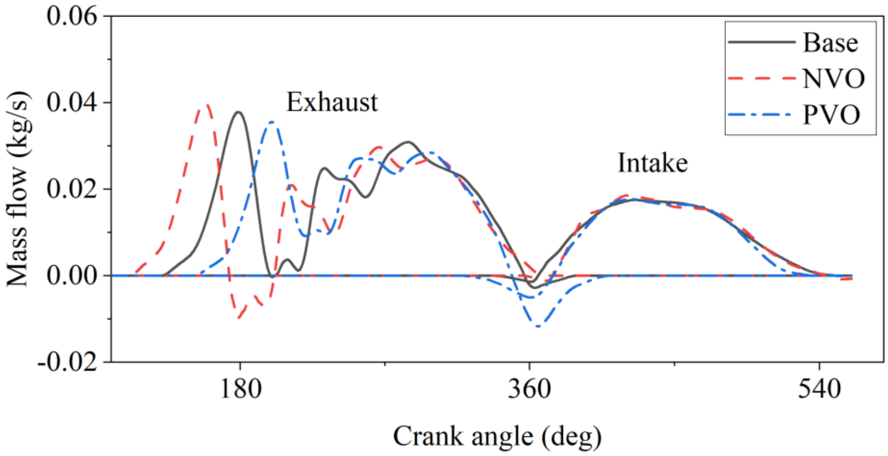

Figure 70 Exhaust and intake mass flow rate during valve overlap period with NVO and PVO strategy.

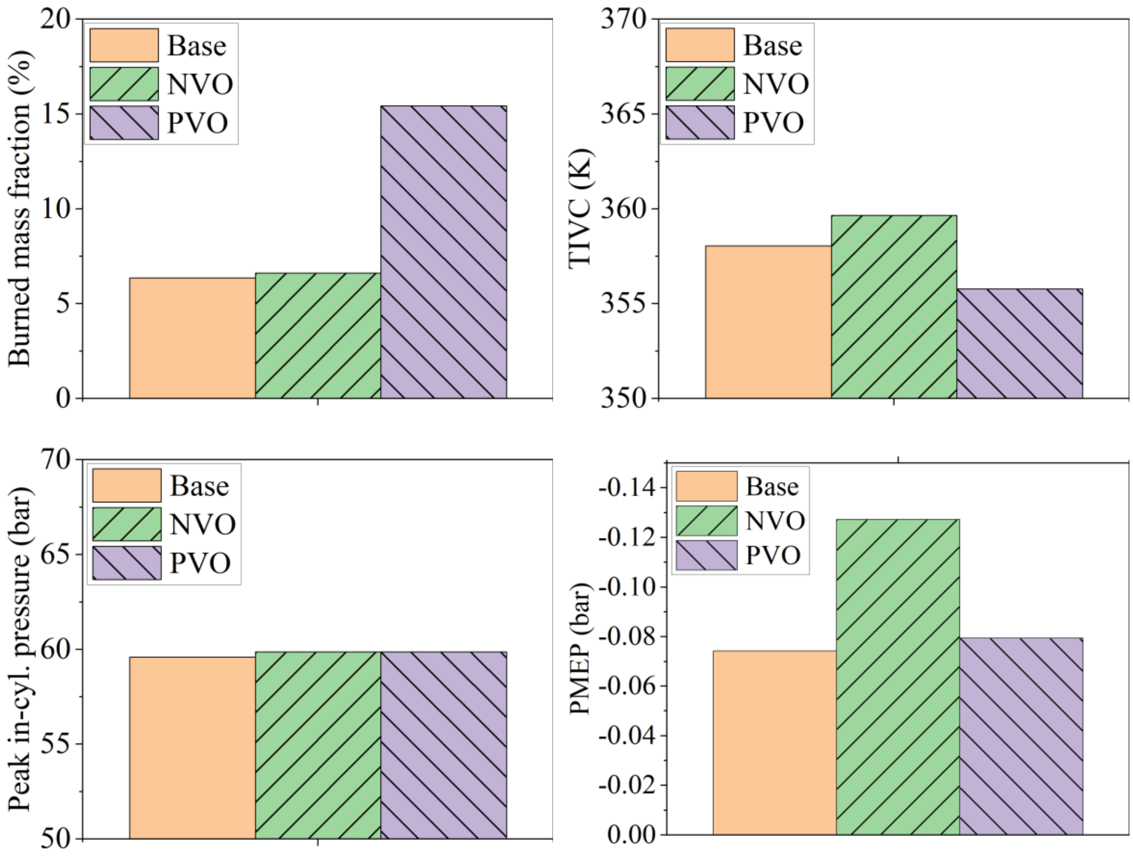

Figure 71 Comparison of burned mass fraction, temperature at IVC, peak in-cylinder pressure, and PMEP with base/NVO/PVO valve strategies.

As shown in Figure 70 and Figure 71, the application of the NVO strategy has a very mild impact on the fraction of the burned gas retained in the cylinder and gas temperature at IVC. In comparison, PVO revealed a higher level of trapped mass than baseline. The prolonged valve overlap caused the backflow of the exhaust gas into the cylinder and intake manifold due to the early opening of the intake valves. However, the lower temperature at IVC was observed with the PVO strategy, although the decrease was negligible. The hot exhaust gas was cooled down due to the backflow into the intake manifold, which is cooler than the in-cylinder condition.

Exhaust gas rebreathing strategy was investigated as a means of elevating thermal conditions in the cylinder. As shown in Figure 72, a significant amount of exhaust gas was re-introduced into the cylinder during the intake stroke by slightly opening the exhaust valve. The three timings of rebreathing strategy, early (-20 ˚CA), baseline, and late (+20 ˚CA), were investigated in this study. The baseline was set at the timing when both maximum lifts of intake and RB are aligned, as shown in Figure 67 (e). It was presented that high levels of burned mass were achieved for the three cases, which increased TIVC. As the RB timing was advanced, the peak backflow mass flow rate also increased, indicating a higher burned mass fraction. With the retarded RB timing, the burned mass fraction in the cylinder dropped slightly, and the lowest TIVC was shown among the three cases in this study.

Effects of the different lifts of the rebreathing valve on thermal conditions at IVC were also investigated with fixed RB timing. The RB timing was maintained at constant timing, but the lift was varied by up to 1 mm. This lift was not optimized, and it was for demonstration only. As expected, higher lift exhibited the increased mass flow, leading to a higher level of trapped gas content, resulting in higher TIVC, as shown Figure 74 and Figure 75.

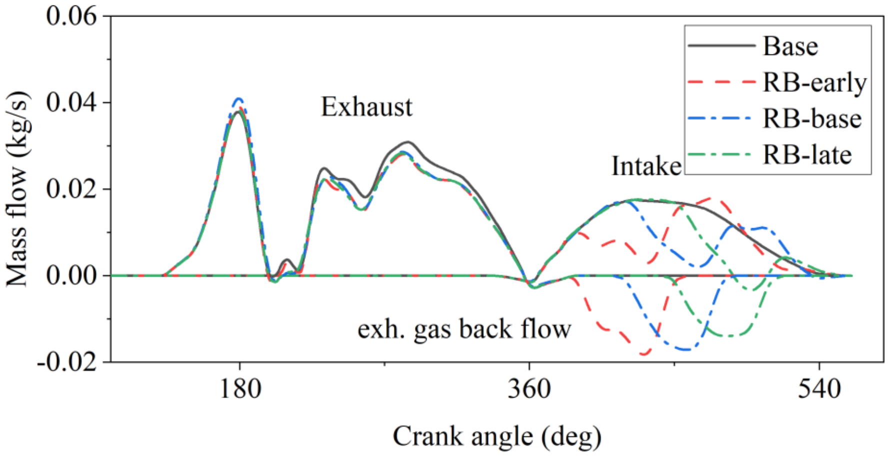

Figure 72 Exhaust and intake mass flow rate with different timing of exhaust gas rebreathing strategy.

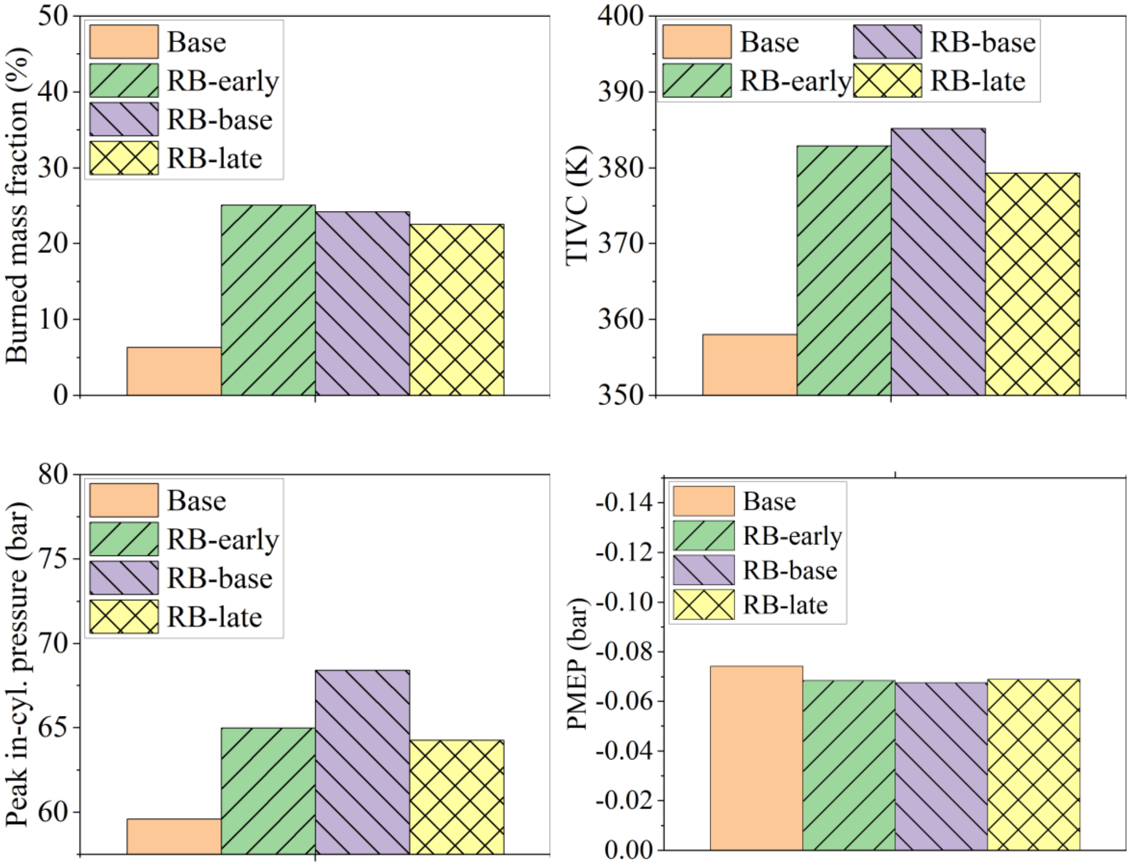

Figure 73 Comparison of burned mass fraction, temperature at IVC, peak in-cylinder pressure, and PMEP with base(NO-RB), RB-early(-20 ˚CA), RB-base, RB-late (+20 ˚CA) valve strategies.

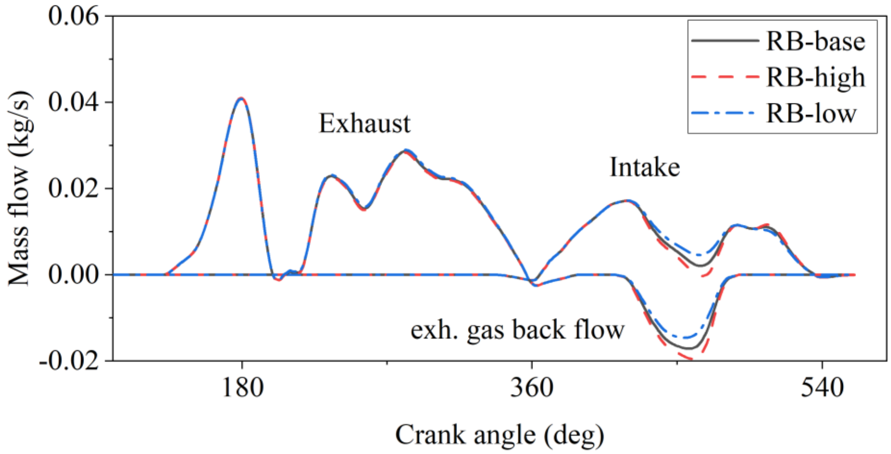

Figure 74 Exhaust and intake mass flow rate with different lifts of exhaust gas rebreathing strategy.

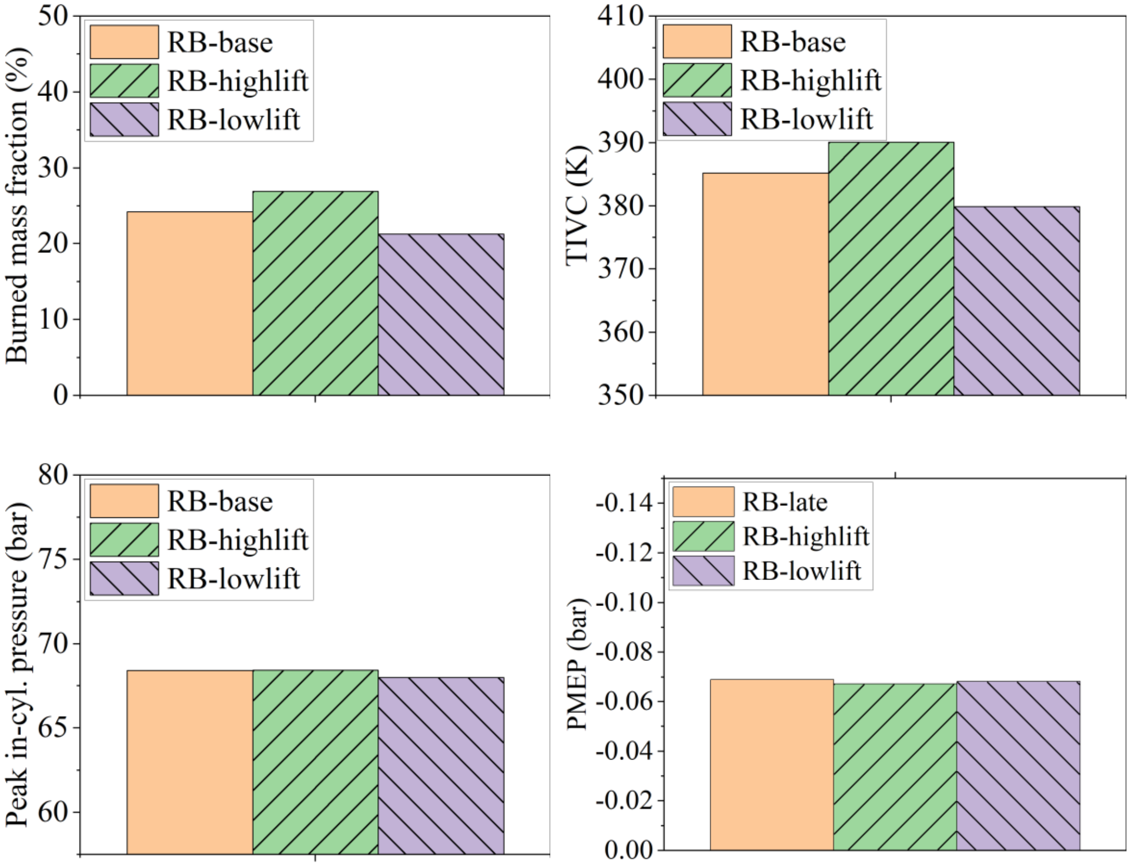

Figure 75 Comparison of burned mass fraction, temperature at IVC, peak in-cylinder pressure, and PMEP with RB-base/RB-high lift/RB-low lift valve strategies.

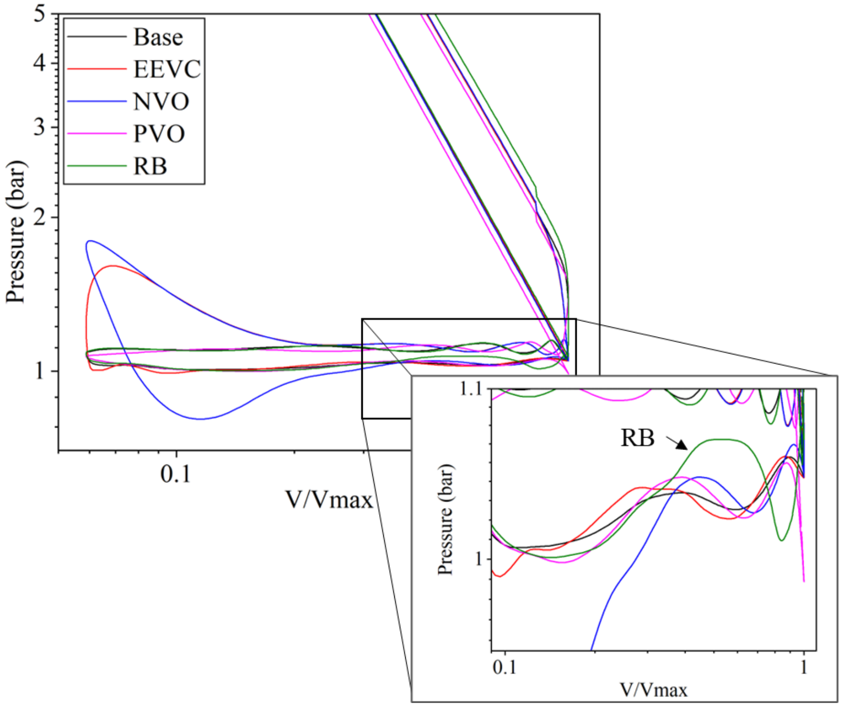

Figure 76 LogP-logV diagram comparison with valvetrain strategies.

Pumping loss is one of the parameters that play a significant role in system-level analysis. P-V graph in log scale, as shown in Figure 76, can be a good indicator. The area of the bottom P-V loop represents the pumping loss in a system. EEVC and NVO showed greater pumping loss in this study. Early exhaust valve closing caused re-compression in the cylinder before the end of the exhaust stroke. As a result, the piston movement toward TDC with early closed valves led to the recompression of the gas. As the intake valve opened near the TDC, the in-cylinder pressure dropped significantly to the ambient level. For NVO, where the intake valve was retarded, in addition to the EEVC strategy, the re-compression was more pronounced, and negative pressure was also observed due to the intake stroke. It should be stated that the intake valve opening timing was not optimized for NVO strategy and can be adjusted to minimize the negative pressure by retarding the intake valve opening. For the RB strategy, a pressure increase was observed at the end of the intake stroke due to the re-introduction of exhaust gas into the cylinder.

Figure 77 summarizes the effects of VVA strategies on the combustion process, including TIVC, TEVO, maximum in-cylinder pressure, IMEP, burned mass trapped, and PMEP at 1250 rpm 3 bar IMEP operating condition. Considering the objective of the VVA implementation, which is to improve the combustion process, rebreathing (RB) was the most effective method to increase TIVC and TEVO and reduce PMEP. TIVC and TEVO were increased up to 33 K and 83 K, respectively, with RB-high lift case, resulting in promoted combustion. Consequently, maximum in-cylinder pressure and IMEP increased by 8.85 bar and 0.48 bar, respectively.

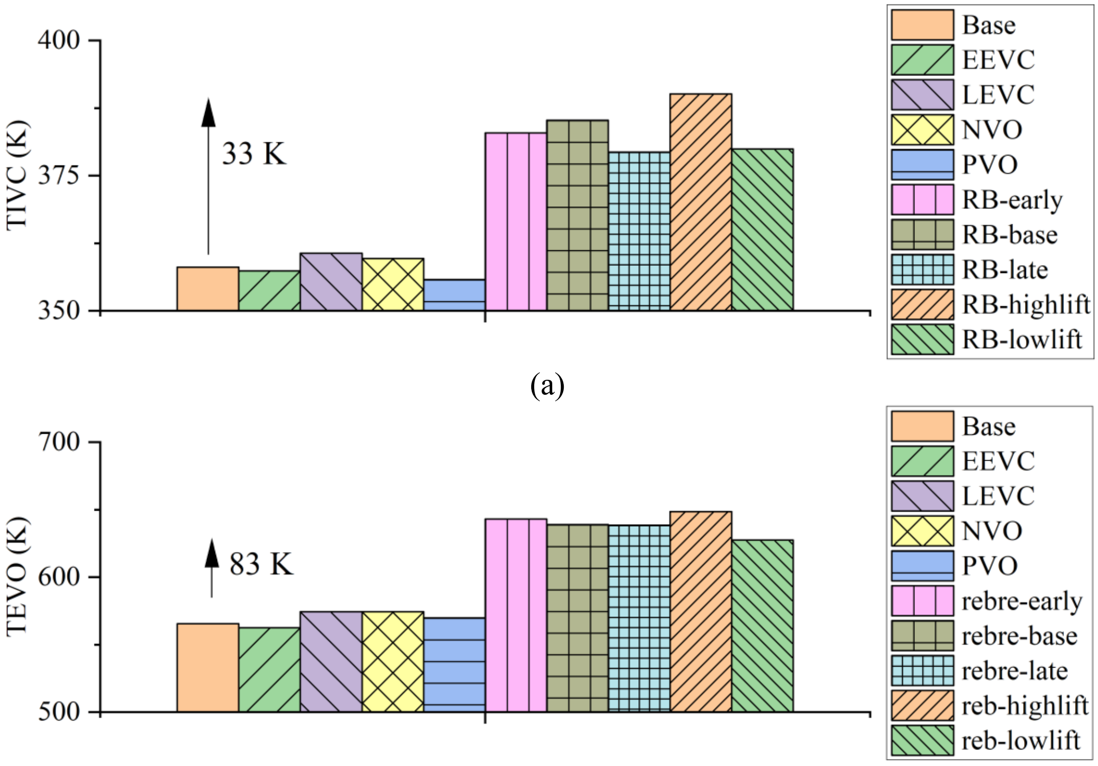

(a)

(b)

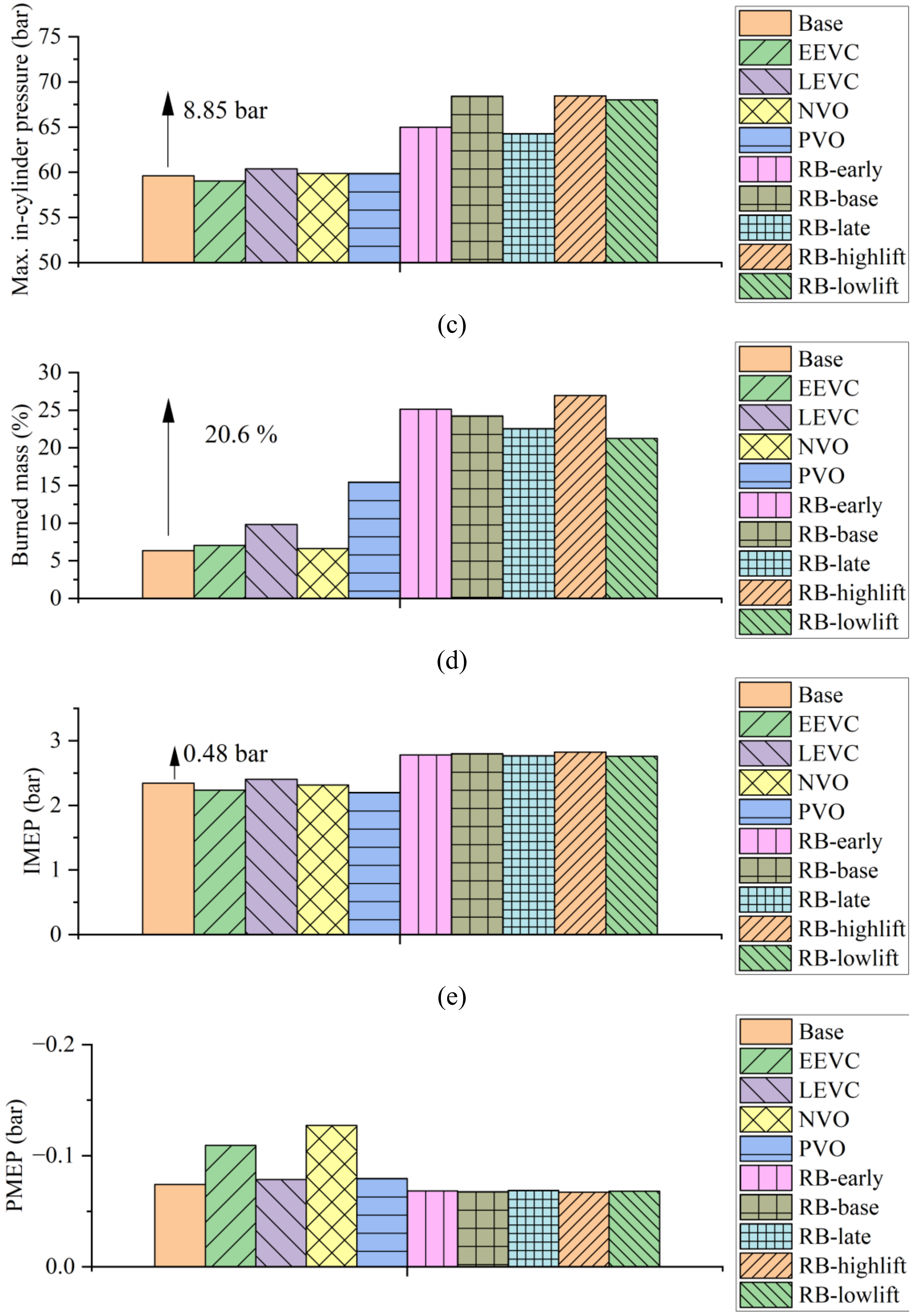

(c)

(d)

(e)

(f)

Figure 77 Summary of the effect of VVA strategies on (a) TIVC, (b) TEVO, (c) Max. in-cylinder pressure, (d) burned mass, (e) IMEP, and (f) PMEP.

5.3 Summary

This chapter evaluated various VVA strategies, including EEVO, LEVO, NVO, PVO, and RB with timings and lifts in a system-level approach. In this study, low load operating condition, 1250 rpm 3 bar IMEP, was considered with the GCI combustion model to account for the effects of thermal boundary conditions attained by VVA on GCI combustion. The simulation results revealed RB was the most attractive and promising strategy among VVA in increasing the bulk gas temperature at IVC, exhaust temperature at EVO, and internal residual gas fraction. RB with a high lift case was able to achieve 33 K, 83 K, and 20.6 % increases in TIVC, TEVO, and burned mass fraction, respectively, compared with that of the base case. This thermally enhanced boundary condition increased maximum peak in-cylinder pressure and IMEP due to the promoted chemical kinetics during the auto-ignition process. Also, the increased TEVO is expected to promote the aftertreatment light-off. In this simulation study, the effects of VVA on PMEP were insignificant, except for the EEVO and NVO cases. This may be due to the fact that inlet and outlet conditions were kept constant without a turbocharger system consideration. Further optimization work is needed in the future for more accurate results.

Chapter 6. Numerical Investigation of the Potential of CC-SCR in Further Reducing NOx Emissions

Selective catalytic reduction (SCR) technology has been proven reliable and effective and is commonly employed in diesel engine applications to reduce tailpipe-out NOx emissions. Moreover, a closed coupled SCR (CC-SCR) system can be additionally utilized to further mitigate the NOx emissions. This chapter firstly addresses preliminary CFD results about the inhomogeneity at the inlet of CC-SCR. Then, the effects of CC-SCR geometry on NOx emissions were numerically investigated using GT-Suite. This chapter utilized diesel engine transient testing data for preliminary analysis due to the limited GCI engine testing results and GCI model emissions prediction. Nevertheless, the simulated results are still expected to be valid for GCI engine application.

6.1 CC-SCR CFD Simulation

This section simulates the effect of CC-SCR on further reducing NOx emissions using CFD and GT-Suite models. The simulation has focused on the impact of the inhomogeneity of the gas flow, the necessity of the different dimension approaches in the SCR model, and the application of a CC-SCR system in reducing NOx emissions. With the increasingly stringent regulations, the closed coupled SCR strategy has been adapted to minimize the tailpipe NOx emissions by maximizing the potential of thermal energy from exhaust gas in the heating SCR system while minimizing the heat loss to the ambient. The CC-SCR is located downstream of the turbocharger, as shown in Figure 78, to reduce NOx emissions further, especially during the cold start process. The wastegate turbocharger in this CFD model was modified and set up based on the available example case (Garrett GT2860RS) from ConvergeCFD, and the CC-SCR was added to the existing 3D model. Again, this case setup was developed for demonstration only and does not represent any actual hardware. Some of the initial boundary conditions are listed in Table 20.

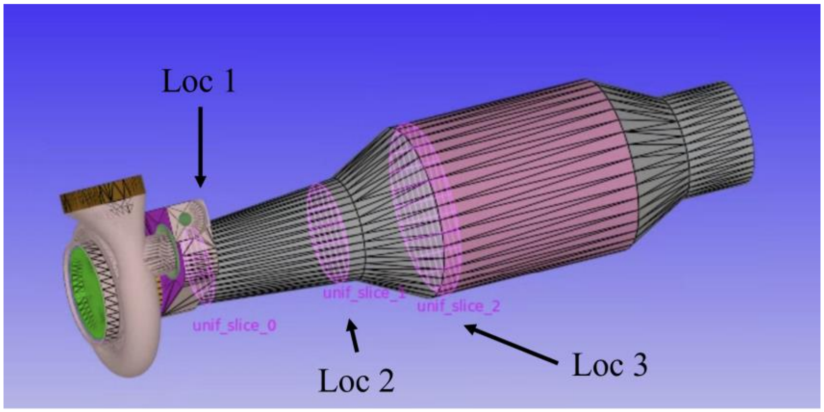

Figure 78 3D CFD model of the closed coupled SCR system with a turbocharger.

Table 20 Initial boundary conditions

Parameter	Value
Inlet pressure [bar]	2
Inlet temperature [K]	700
Outlet pressure [bar]	1
Outlet temperature [K]	500
Turbine speed [RPM]	120k

Figure 79 shows a cross-sectional diagram of flow velocity under steady-state operating condition. As expected, the flow velocity was higher near the wall, whereas the center region showed lower velocity due to the centrifugal force induced by the turbine blade. As the flow reached the diverging cone pipe, the overall velocity was reduced due to the increased cross-sectional area. At the inlet of the SCR catalyst block, denoted as the pink region in Figure 78, the stagnated flow in Figure 79 was observed because of the flow fraction caused by the monolith. Figure 80 presents the cross-sectional velocity magnitude distribution at three locations: 1) the outlet of the turbine (Loc1), 2) the middle of the inlet pipe (Loc2), and 3) the inlet of the SCR monolith (Loc3), as noted in Figure 78.

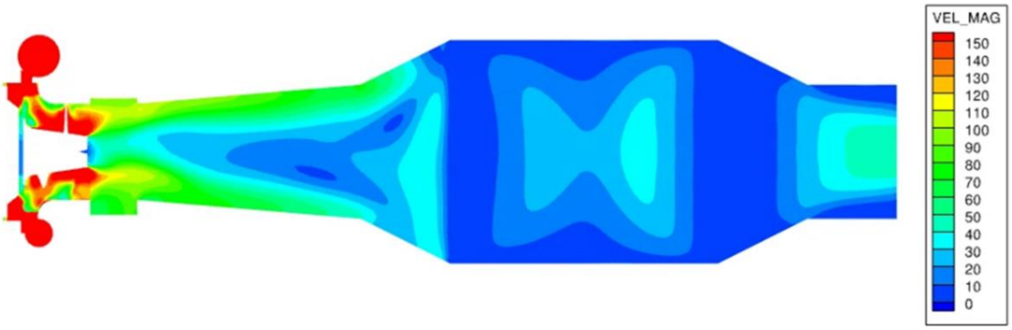

Figure 79 Cross sectional diagram of gas velocity across the CC-SCR system.

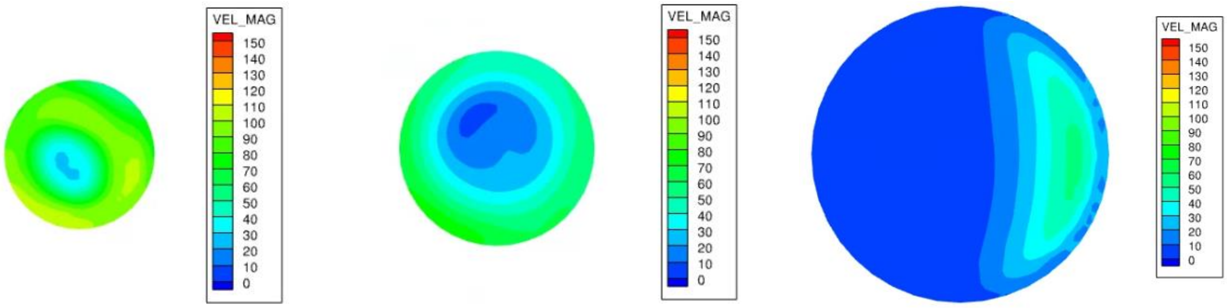

(a) Location 1: 0.27 m (b) Location 2: 0.35 m (c) Location 3: 0.41 m

UI: 0.76 UI: 0.66 UI: 0.48

Figure 80 Cross-sectional diagrams of velocity magnitude at 0.27, 0.35, and 0.41 m from the turbine outlet.

The definition of uniformity Index (UI), shown in Figure 80, is presented in Eq. 6.1, and it is an indicator of the state of the distribution on a plain surface. If UI is closer to unity, it means the distribution is closer to uniform in the cross-section. UI was employed to quantify the inhomogeneity of the flow velocity. As shown in Figure 80, when exhaust gas flows to the inlet of SCR, the UI observed is relatively low, indicating the flow is highly non-uniform at the inlet of the CC-SCR in this simulation. The highly non-uniform distribution of the flow velocity will result in non-uniform reaction rates and non-uniform species distributions, eventually leading to lower NOx conversion efficiency than the ideal uniform distribution represented by UI of 1. In addition, the urea solution is injected upstream of the SCR system. The distribution of NH_3 may also be non-uniform, considering the atomization and evaporation of urea solution and such a short travel distance and time. If the urea injection location is close to SCR, urea or NH_3 may show skewed concentration at a particular location due to the short mixing time, especially when the exhaust temperature is low. This may cause inconsistency between the distribution of exhaust gas species and the NH_3 in the SCR system. This preliminary flow observation can reveal the importance and necessity of utilizing different dimensions of the SCR model in a system-level analysis.

$$UI = Y_{L1,x} = 1 - \frac{1}{2} \sum_{1}^{Ncells} \frac{A_{cell}}{A_{plane}} \frac{|x_{cell} - x_{mean}|}{x_{mean}} \qquad \text{Eq. 6.1}$$

6.2 SCR GT-Suite Model with Different Dimensions

This section examines SCR GT models with different dimensions, considering the observation from the CFD simulations described in the previous section. Under highly non-uniform distribution conditions, such as at the inlet of the CC-SCR, a high dimensional SCR model needs to be utilized to account for the inhomogeneity. GT-Suite offers 1D, 2D, and 3D SCR models that can be integrated with the engine system. In this study, the performance of the SCR model with 1D and 3D dimensions is selected and evaluated in terms of NOx conversion efficiency and computational time. For the evaluation of the model, a simple SCR system model was developed, as shown in Figure 81.

In this model, the gas phase NH_3 was directly imposed as an input, and the gas composition is listed in Table 21. The SCR surface mechanism was adapted from the reference [87]. The ratio of NO_2 to NO was set as 1:1, and the concentration of NH_3 was equal to the total NOx concentration. Theoretically, the ratio between NH_3 and NOx should be about 1 so that all the NH_3 is consumed, and no significant NH3 is slipping through the SCR catalyst since NH_3 is a toxic species and highly regulated. This model was first validated against test bench results, as shown in Figure 82. The model was mainly validated at a high-temperature range for demonstration purposes, where the NOx reduction efficiency was high. The result showed that the NOx reduction efficiency was well correlated with each other with up to 3 % error range.

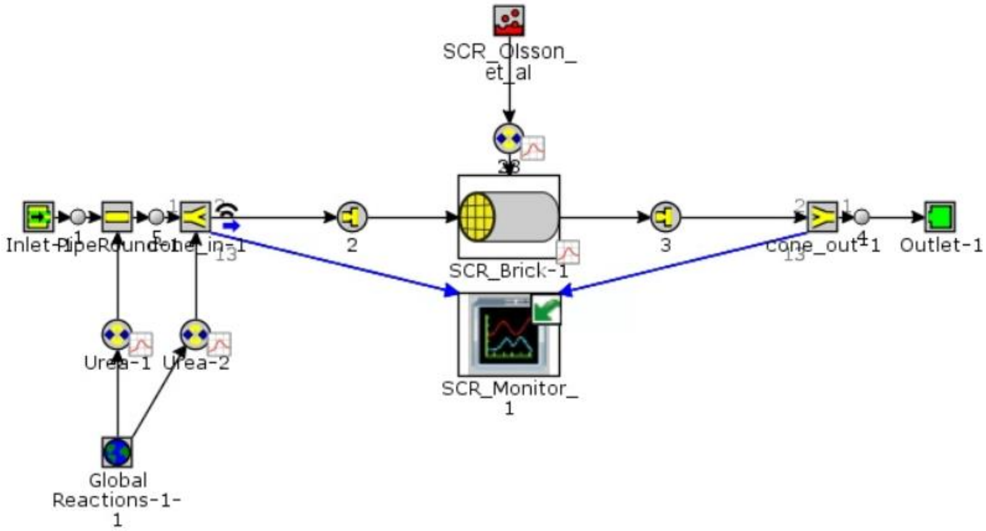

Figure 81 SCR model in GT-Suite.

Table 21 Boundary condition and inlet composition in this simulation.

Boundary condition	
Gas temperature [°C]	100-600
Wall temperature [°C]	100-600
Exhaust flow rate [g/s]	72 / 150 / 300
Cell density [CPSI]	400
Diameter [in]	11.35
Length [in]	12.9
Volume [L]	15.7
Inlet gas mole fraction [88]	
O_2	8 %
N_2	83.9 %
H_2O	8 %
NH_3	500 ppm
NO	250 ppm
NO_2	250 ppm

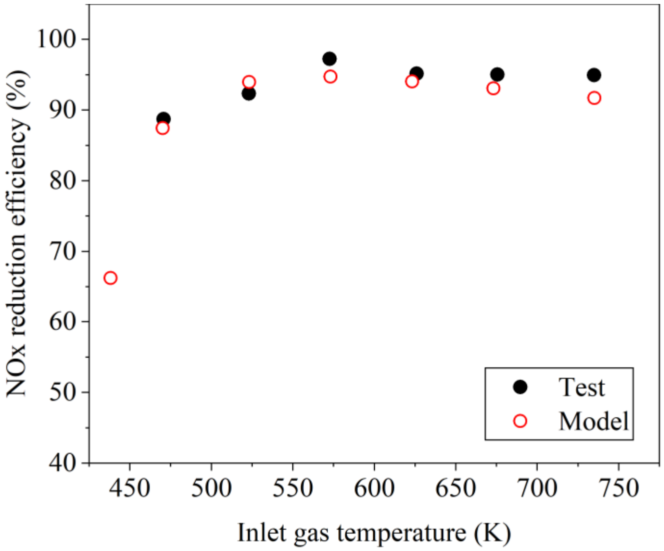

Figure 82 Comparison of NOx emissions simulated by GT-Suite SCR model with experimental results [88].

The validated model was utilized using 1D and 3D dimension approaches with both uniform and non-uniform species assumed, respectively, as shown in Figure 83. The NOx and NH_3 species were evenly distributed in the uniform case, and for non-uniform cases, NOx and NH_3 species were fed to about 75 % of the entire frontal area. As mentioned above, exhaust gas flow may exhibit highly non-uniform distribution at the inlet of the SCR catalyst, so a non-uniform case was examined in this study even though the distribution considered here may not represent actual gas flow and distribution. As shown in Figure 84, the 1D and 3D uniform cases were identical, and up to 7.6 % difference was shown between 3D non-uniform and uniform cases when the simulated mass flow rate was 72 g/s. This raises the need for a high-dimensional approach for an accurate NOx estimation.

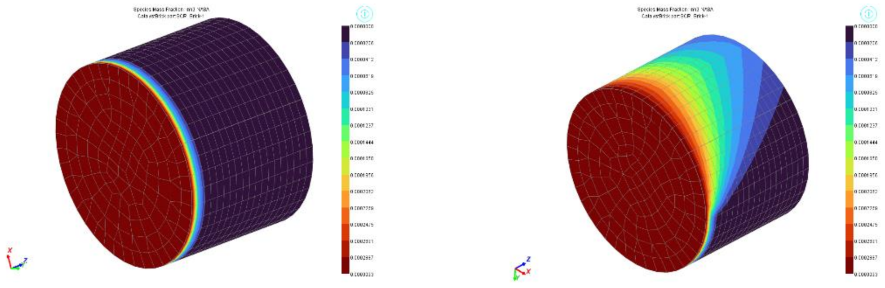

(a)Uniform species distribution. (b) Non-uniform distribution.

Figure 83 (a) Uniform and (b) non-uniform species distributions

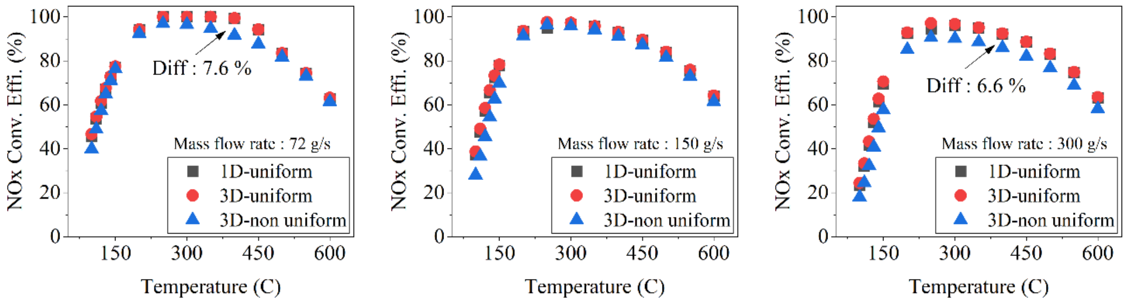

Figure 84 NOx conversion efficiency with different mass flow rates, 1D and 3D, uniform, and non-uniform inlet distribution.

It should also be stated that NOx and NH_3 species were fed together due to the limitation of the current modeling tool. In real applications, emissions and urea fluid droplets or gas phase NH_3 may not necessarily enter SCR evenly because of the droplet buoyant effect and gravity. If these effects were considered, the inconsistency might be increased because some portion of NH_3 may slip through the catalyst without participating in the catalytic reaction, resulting in a lower reduction rate of NOx emissions and a high level of ammonia slip. In conclusion, this demonstration necessitates an SCR model capable of simulating the independent distribution of urea or NH_3 species in a 3D SCR model.

Figure 85 indicates the significant increase in computation time when the 3D model was used, compared with 1D cases. In this evaluation, the simulation was terminated if 2000 iterations were reached or the steady state was achieved. The 1D model took less than 1 second across the cases, and when three-dimension approaches were adapted, the computational time significantly increased up to about 180 seconds per case. Considering the compromise between the model accuracy and computational time, in addition to the species distribution, selecting the efficient model will significantly influence a system-level analysis time, especially under a transient cycle.

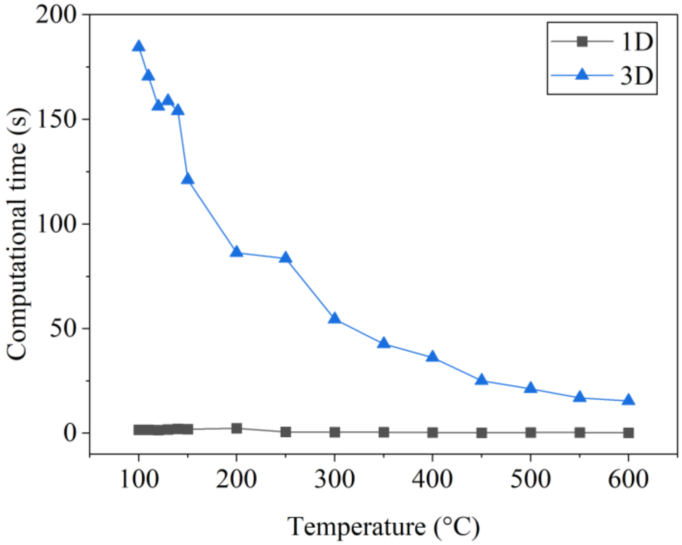

Figure 85 Impact of inlet temperature and model dimensions on computational time.

6.3 Closed Coupled SCR GT Model Analysis

In this section, the developed SCR model was applied to numerically examine the potential of a CCSCR in reducing NOx emissions. The impacts of CCSCR volume and geometry on NOx emissions were simulated with main floor SCR to investigate and maximize the NOx reduction efficiency under the first 500-second HD FTP transient operation. The volume, frontal diameter, and length of the CC-SCR system varied, as shown in Table 22. NH_3 was directly imposed as gas-phase as an input, and the ratio of NH_3 to NOx species was maintained at ~1 by a PID controller to inject additional NH_3 upstream of the main SCR. The exhaust gas temperature and composition at the inlet of SCR, measured from a 2010 model year HD engine FTP testing [89], were imposed in this model. Figure 86 shows the CC-SCR and SCR GT models used in this study. Adding CC-SCR while keeping the original main SCR system in this scenario increased the total SCR volume. The volume of the CC-SCR was varied from 10 ~ 50 % of the main SCR (15.7 L) with the assumed 3-, 6-, and 9-inch diameters. The length of CC-SCR was calculated accordingly to maintain the respective volumes. Table 22 lists the simulated cases.

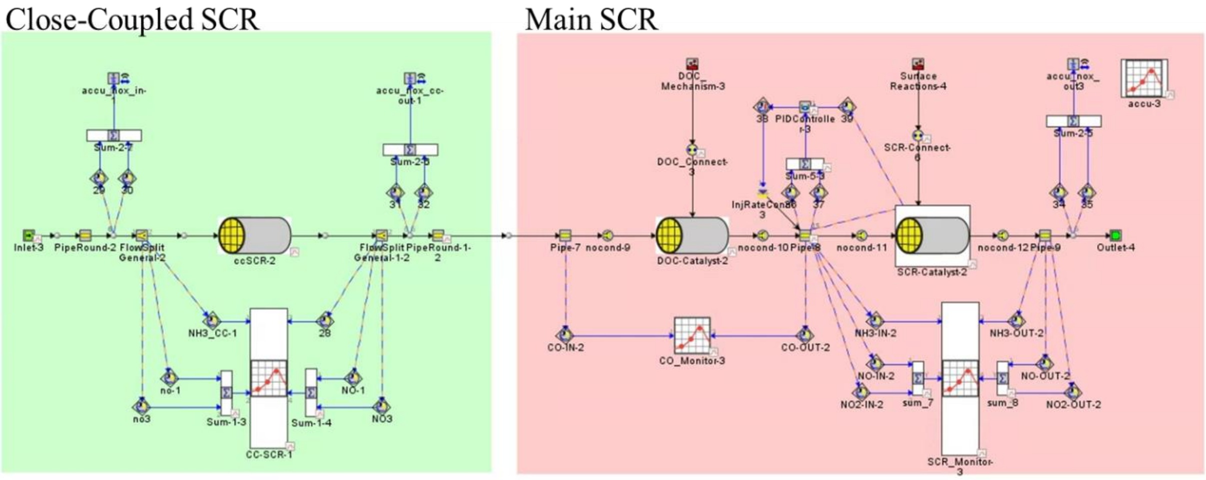

Figure 86 The CC-SCR and main SCR system in GT-Suite model.

Table 22 Detail of cases considered, adding CC-SCR while keeping the main SCR volume.

Case	1	2	3	4	5	6	7	8	9	10	11	12	13	14	15
Main SCR vol. [L]	15.7														
CC-SCR vol. [%] (relative to main SCR)	10	10	10	20	20	20	30	30	30	40	40	40	50	50	50
Total SCR Vol.[L]	**17.3**	**17.3**	**17.3**	**18.8**	**18.8**	**18.8**	**20.4**	**20.4**	**20.4**	**22.0**	**22.0**	**22.0**	**23.6**	**23.6**	**23.6**
CC-SCR dia.[in]	3	6	9	3	6	9	3	6	9	3	6	9	3	6	9
CC-SCR length [in]	4.6	3.7	3.7	10.8	7.6	7.4	18.1	11.6	11.1	26.5	15.7	15.0	35.8	20.0	18.7
Accum. NOx [g]	18.2	17.7	17.6	17.8	17.1	16.9	17.7	16.9	16.7	17.8	16.9	16.7	18.0	17.0	16.7

Figure 87 ~ Figure 89 present the location of the NOx probe in this simulation, accumulated mass of NOx after 500 seconds of HD FTP cycle in different cases, and temperature at SCRs. In Figure 88, the lower case number indicates a smaller volume of CC-SCR (10 % of the main SCR), and the higher number case presents a bigger CC-SCR volume (50 % of the main SCR). The three consecutive cases have the same volume but different diameters and lengths of CC-SCR, as shown in Table 22.

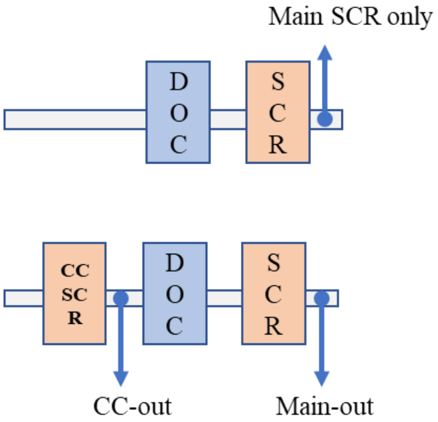

Figure 87 Location of NOx measurement in simulation.

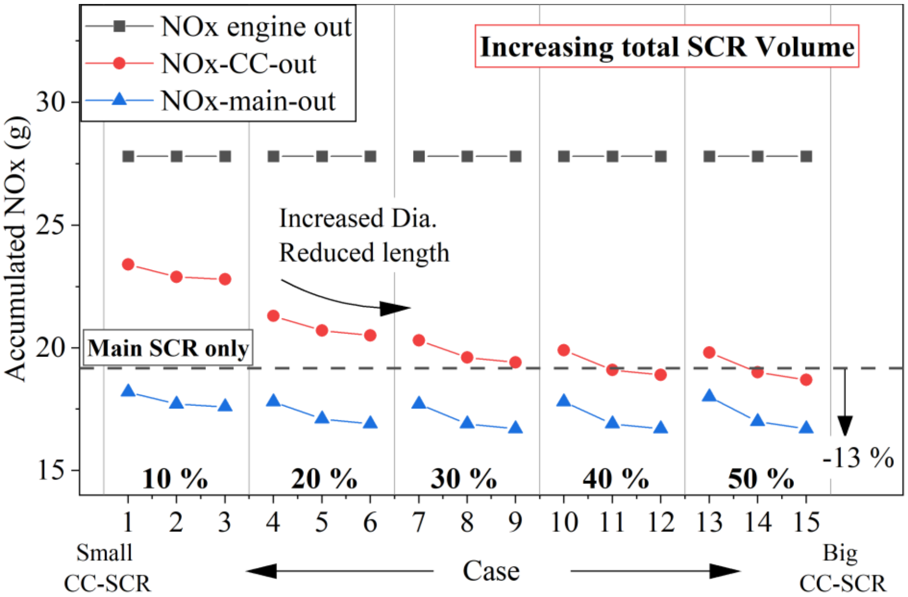

Figure 88 Accumulated NOx emitted from engine, CC-SCR, and main SCR. The volume of the CC-SCR varied from 10 % ~ 50 % of the main SCR.

It was observed that a larger CC-SCR effectively reduced NOx, and a larger frontal diameter with a shorter length was more effective when the volume of the CC-SCR was maintained, as shown in Figure 88. With CC-SCR, up to an additional 13 % of NOx was reduced compared to the main SCR only case. This is because CC-SCR temperature presented a rapid increase compared with that of the main SCR, as shown in Figure 89, and surface catalytic reaction in CC-SCR started to activate earlier than the main SCR. It took about 235 seconds for CC-SCR to reach 170 ˚C, which is a significant reduction (~ 41%) compared to the main SCR. Figure 90 shows the temperature variation of scenario 1 (CC-SCR + main SCR) and the main SCR only case, colored with urea injection activation range (160~180 ˚C). CC-SCR in the scenario 1 case reached 170 ˚C, about 20 % faster than the main SCR only case. The simulation results also revealed that the performance of CC-SCR was saturated with about 30 % case, not showing significant improvement with further increase in its volume.

Additionally, the greater volume of CC-SCR did not always show a better NOx reduction rate. As shown in case 12 and case 13 in Figure 88, a lesser volume of CC-SCR (40 % of the main SCR) with a larger diameter performed better in NOx reduction than a greater volume of CC-SCR (50%). This result poses the importance of optimization in CC-SCR geometry to maximize its performance.

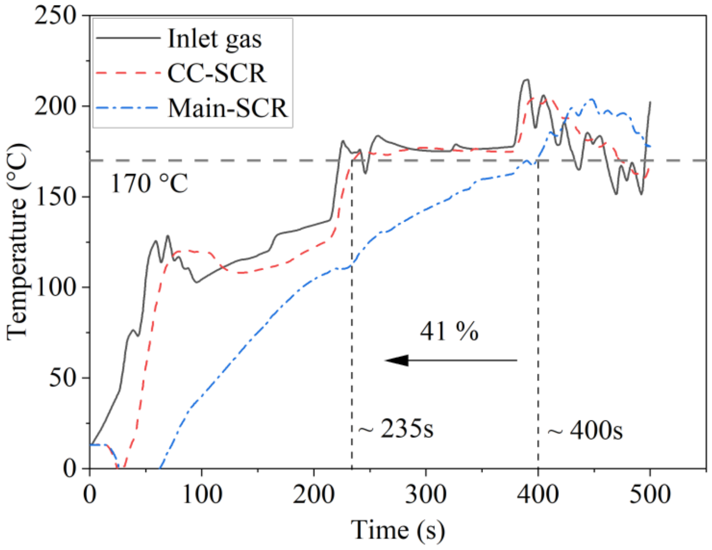

Figure 89 Variation of the temperatures at inlet, CC-SCR, and main SCR with time under the first 500 second HD FTP transient cycle simulation

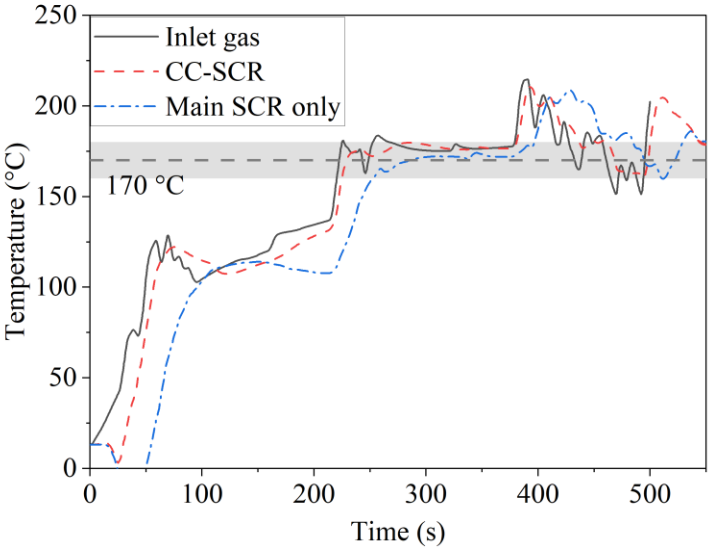

Figure 90 Variation of the temperatures at the inlet, CC-SCR + main SCR case (scenario1), and main SCR only case under the first 500 second HD FTP transient cycle simulation

Figure 91 presents (a) the space velocities of the different CC-SCR volumes and (b) the NOx reduction efficiency among the cases with the same volume but different diameters. Space velocity can be considered as an indicator showing the residence time of the gas in the CC-SCR, and it was observed that the space velocity was nearly constant for the same volume of the CC-

SCR. Lower space velocity means the time spent in the catalyst is longer, which results in higher reduction efficiency. As shown in (b), a bigger diameter of the CC-SCR was shown to be more effective in reducing NOx when the volume was constant.

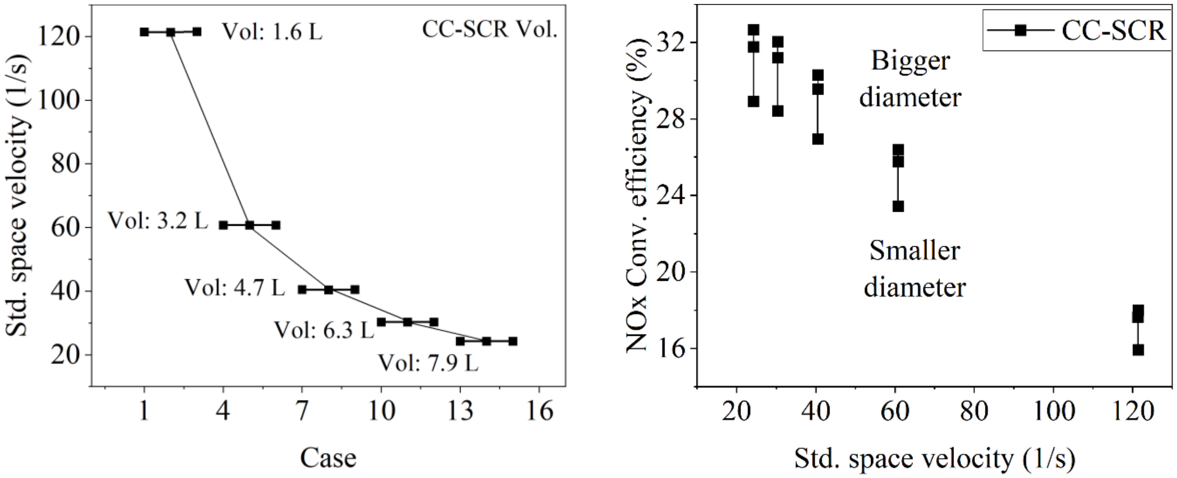

(a) Standard space velocity (b) NOx reduction efficiency in CC-SCR

Figure 91 Impact of CC-SCR geometry on gas space velocity and NOx reduction efficiency of CC-SCR.

It should be mentioned that the gas temperature was imposed as an input in this simulation and obtained upstream of DOC during the test, which implies that the gas temperature in this study may be lower than the actual turbine out gas temperature. Also, the gas phase NH_3 was directly imposed in this analysis instead of liquid phase urea solution, so the evaporation and the availability of NH_3 will also affect the overall performance of the CC-SCR. Therefore, the inhomogeneity of species such as NOx and NH_3 should also be considered for evaluating the effects of the geometry of the CC-SCR on reduction efficiency.

A 2nd scenario was also considered in this study to evaluate the performance of the CC-SCR in reducing NOx emissions when the total volume of the SCR system was kept constant. In this scenario, the volume of the main SCR was also reduced according to the size of the CC-SCR to keep the total volume of the SCR system constant. The case setup is listed in Table 23. As previously mentioned, the CC-SCR varied from 10 % ~ 50 % of the original main SCR size (15.7 L). However, the main SCR was also reduced from 90 % to 50 % of the original volume (15.7 L), respectively, so that the total volume of the SCR can be kept constant (15.7 L). As shown in Figure 92, the accumulated NOx decreased by about 12 %, comparable to the previous scenario 1 (increased total SCR volume by adding CC-SCR). Figure 93 compares the accumulated NOx observed from scenario 2 (constant total SCR volume with CC-SCR introduced) and scenario 1 (increased total SCR volume by introducing CC-SCR). It was evident that reducing the volume of the main SCR with the addition of CC-SCR did not significantly impact NOx emissions, compared with the cases when the volume of the main SCR was maintained as constant. The reduction in NOx emissions was mainly due to the quick warm-up of the CC-SCR. Further simulation work should be conducted.

Table 23 List of the simulation cases when the total Vol. of SCR was kept constant at 15.7 L.

Case	1	2	3	4	5	6	7	8	9	10	11	12	13	14	15
Main SCR vol. [frac.]	0.9	0.9	0.9	0.8	0.8	0.8	0.7	0.7	0.7	0.6	0.6	0.6	0.5	0.5	0.5
CC-SCR vol. [%] (relative to original main SCR)	10	10	10	20	20	20	30	30	30	40	40	40	50	50	50
Total SCR Vol. [L]	**15.7**														
CC-SCR dia.[in]	3	6	9	3	6	9	3	6	9	3	6	9	3	6	9
CC-SCR length [in]	4.6	3.7	3.7	10.8	7.6	7.4	18.1	11.6	11.1	26.5	15.7	15.0	35.8	20.0	18.7
Accum. NOx [g]	18.2	17.7	17.6	17.8	17.1	17.0	17.7	17.0	16.7	17.9	17.0	16.7	18.1	17.1	16.8

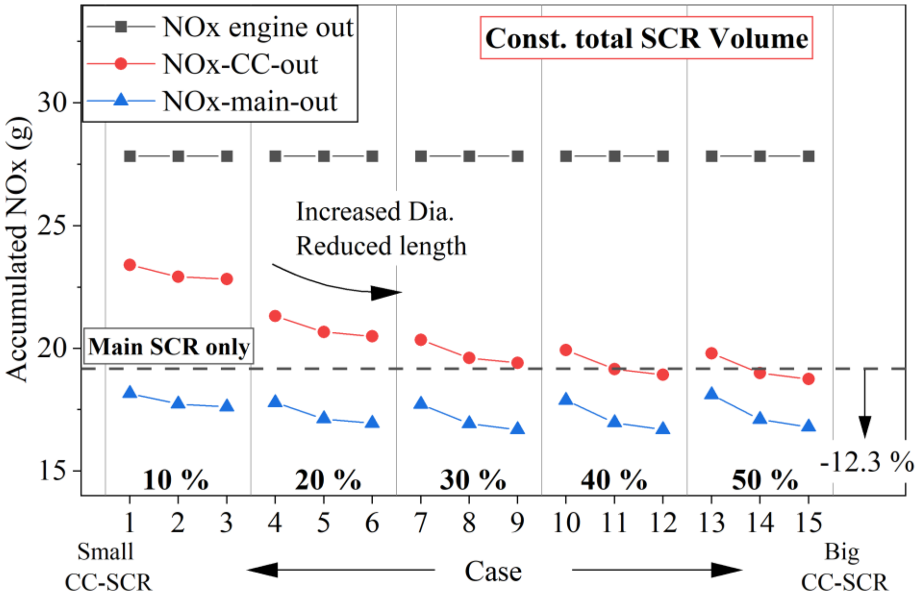

Figure 92 Accumulated NOx emissions at engine-out, CC-SCR out, and main SCR out. The volume of the CC-SCR varied from 10 % ~ 50 % with reduced main SCR volume accordingly. Total SCR volume was kept constant.

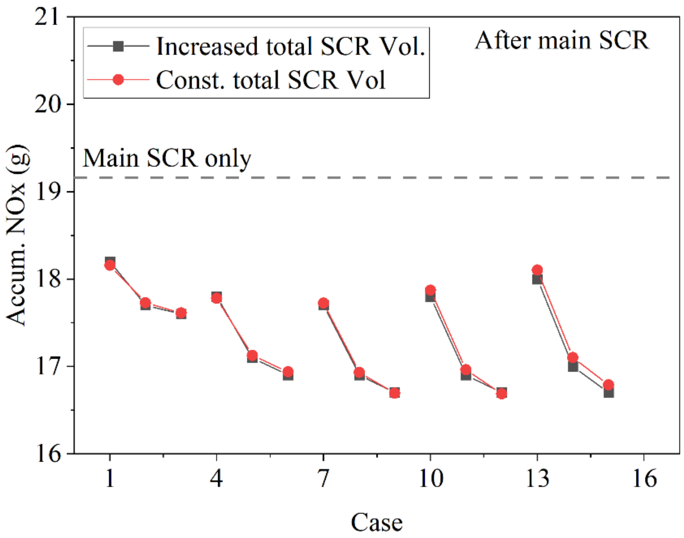

Figure 93 Effect of CC-SCR on the accumulated NOx after main SCR with/without increasing the total volume of the SCR system.

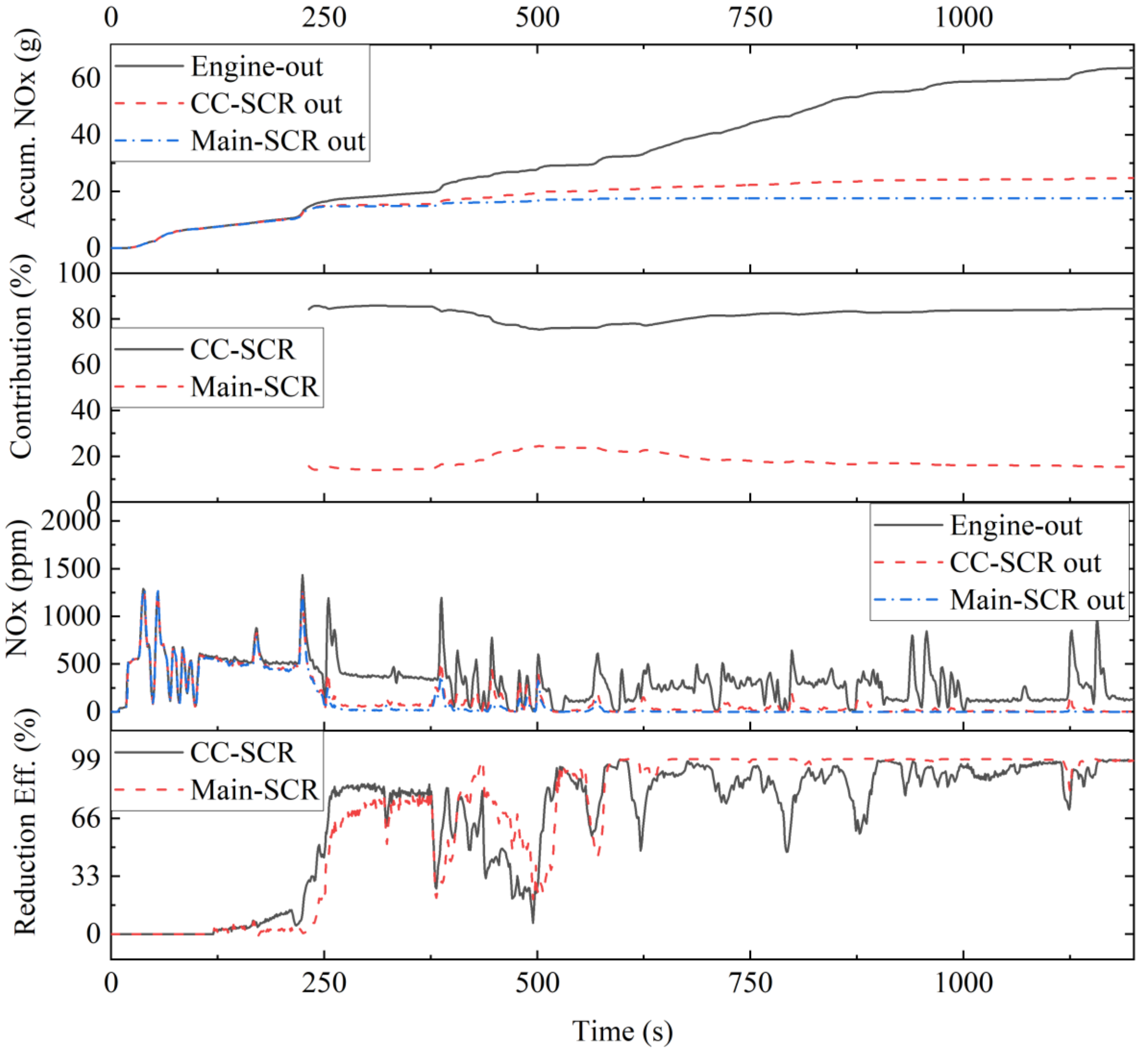

Figure 94 Instantaneous accumulated NOx, contribution at each SCR, concentration, and reduction efficiency of the NOx emission during HD FTP transient cycle with 30 % CC-SCR and total SCR volume of 15.7 L.

Figure 94 shows the instantaneous accumulated mass, contribution of NOx reduction at each SCR, instantaneous NOx concentration, and reduction rate of NOx at engine-out, downstream CC-SCR, and downstream main SCR under HD FTP transient cycle. As expected, CC-SCR showed faster initiation of NOx reduction than the main SCR due to the quicker warm-up, resulting in a considerable drop in NOx concentration level as well.

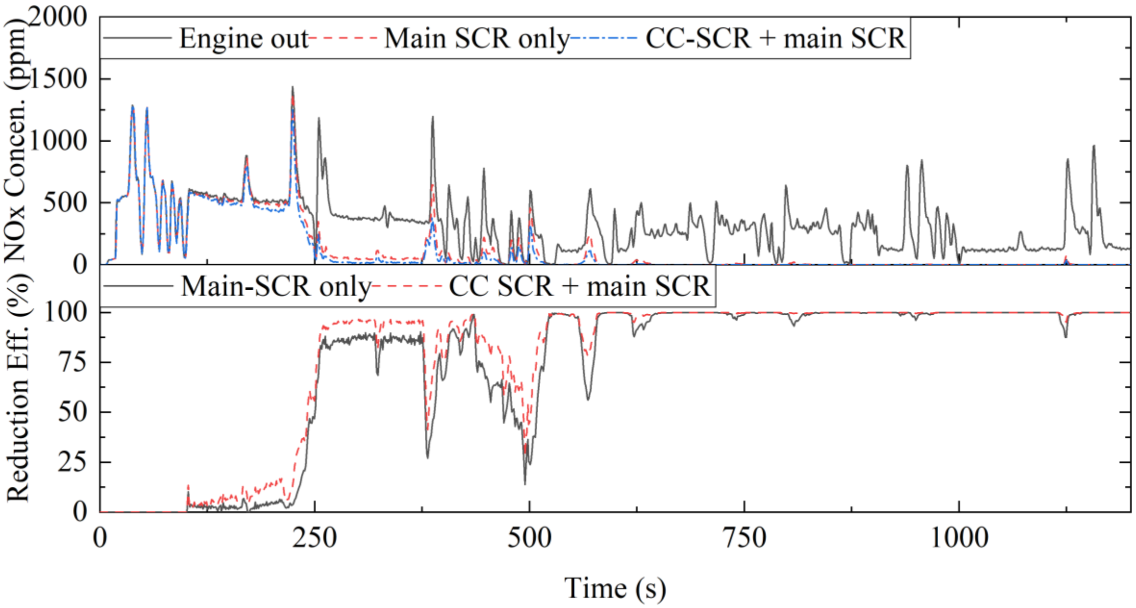

Figure 95 Instantaneous NOx concentration and reduction rate with main SCR only and 30 % CC-SCR case + main SCR. The volume of the total SCR is 15.7 L.

It was observed that CC-SCR contributed more than 80 % of total NOx reduction throughout the entire cycle once it was warmed up. In contrast, the main SCR contributed only about 20 % of total NOx reduction. This result reveals that even a small CC-SCR will effectively decrease NOx emissions during the cold start process. The volume of the CC-SCR was less than half of the main SCR, both totaling 15.7 L. A NOx reduction efficiency drop was observed from 375 to 500 seconds of the cycle because of relatively higher engine speed and less torque request of the FTP cycle. It was also observed that the NOx reduction efficiency of the main SCR reached nearly 100 % (at 625s), whereas CC-SCR presented some degree of variation due to relatively lower residence time caused by the higher velocity and temperature of the exhaust gas.

Figure 95 compares the instantaneous NOx concentration and reduction efficiencies of 1) main SCR only and 2) 30 % CC-SCR case + main SCR with constant total SCR volume, 15.7 L. It was evident that CC-SCR + main SCR showed dramatically improved performance due to the shorter light-off temperature of the CC-SCR. Also, during rapid transient operations such as at 350~500 seconds, CC-SCR still showed a higher NOx reduction rate than that of the main SCR only case even though the overall efficiency dropped due to the lower thermal energy content and higher flow velocity of exhaust gas during transient operation. This caused species to slip through the SCR. This efficiency drop was also observed in engine testing results [89].

6.4 Summary

This chapter presented a preliminary numerical investigation of the CC-SCR implementation in an HD diesel engine system. Firstly, the CFD simulation identified the non-uniform velocity and species distribution in a CC-SCR system, which raised the necessity for a high-dimension SCR model. Highly non-uniform distribution was identified at the inlet of CC-SCR due to the centrifugal force induced by a turbocharger. To account for non-uniform distribution, a 3D SCR model available in GT-Suite was utilized to simulate the uniform and non-uniform inlet distribution cases. Up to 7.6 % variation was observed between the two cases in 3D SCR model simulation. The simulation of the CC-SCR using the GT model concluded that the addition of a CC-SCR was a very effective method to reduce the tail-pipe NOx emissions further. In contrast, the effectiveness of having larger volume of the main SCR diminished with CC-SCR installation during the HD cold FTP transient cycle. The majority of the tailpipe NOx was accumulated during the beginning of the cycle when the SCR system temperature was low. Once the main SCR system reached a warm-up state, there was no significant difference among the different volumes of the main SCR. Also, it should be reminded that NH_3 was directly imposed at the inlet instead of liquid phase urea solution. Therefore, the influence of urea spray phenomena, such as evaporation and non-uniform distribution, were not accounted for in this simulation. Further investigation may be needed.

Chapter 7. Conclusions and Future Work

7.1 Conclusions of This Study

This research developed a quasi-dimension combustion model for GCI combustion engines featuring PPCI and diffusion combustion. Commercially available CFD software, ConvergeCFD, was utilized to simulate GCI combustion with a reduced TPRF-E chemistry mechanism. The CFD model was validated against GCI engine testing data at 1) 2000 rpm 12 bar IMEP and 2) 2250 rpm 18 bar IMEP. Additional CFD simulations were conducted to provide a reference for the quasi-dimensional GCI combustion model development and validation. The GCI combustion model developed was able to capture the main combustion characteristics of GCI combustion and predict the cylinder pressure, heat release process, and combustion phasing. The developed GCI combustion model was integrated into GT-Suite and used to numerically investigate the impact of VVA strategies in improving the low-load operation of the GCI engine. The potential of introducing a CC-SCR into an HD diesel engine after-treatment system to reduce NOx emissions during the cold start process was numerically examined. The main findings and conclusion of this study can be summarized as follows.

- A CFD simulation model with TPRFE mechanism was developed using ConvergeCFD. at Aramco. The simulated in-cylinder pressure, heat release rate, and combustion phasing of the GCI engine were found to agree reasonably well with experimental data at 2000 rpm 12 bar IMEP and 2250 rpm 18 bar IMEP measured at Aramco. The difference in the peak in-cylinder pressures for both operating conditions was less than 2 bar. Discrepancy of CA90 was less than 6 ˚CA, and CA10 and CA50 presented less than 3 ˚CA across the operating conditions.
- The traditional quasi-dimension spray jet model by Hiroyasu was improved in this

study to account for 1) the ramp-up and ramp-down period of the rate of injection and 2) fuel distribution within the fuel cloud. The spray model was calibrated against the test result from the reference, and the spray tip penetration length was well captured by the improved model.

- A spray CFD simulation was conducted to investigate fuel distribution in spray plumes and confirm the model improvement in this study. CFD simulation results displayed analogous behavior, showing a high concentration of the fuel near the tip of the spray. This characteristic was well simulated in the improved spray model. Additionally, spray wall impingement was simulated using CFD, and results also revealed a higher concentration of fuel near the tip of the spray plume.
- PPCI combustion was simulated by considering fuel distribution and a multizone approach in the developed combustion model. The fuel distribution was estimated by the improved spray model, and a multizone approach was used to calculate the ignition delay of fuel packets. Flame propagation and heat release were calculated. Mixing-controlled diffusion combustion was modeled by the traditional spray jet model. Spray penetration, air entrainment, ignition delay, and heat release were calculated at each time step.
- The GCI model was validated against both engine experimental data available by Aramco and the CFD simulation data. The cylinder pressure, heat release process, and combustion phasing predicted using the quasi-dimension model were found to agree reasonably well with engine test data and CFD simulation results, showing less than 1 bar in IMEP and 2 ˚CA variation in CA 50. The impact of temperature, pressure, and EGR rate at IVC on GCI combustion can be simulated with acceptable accuracy.

- VVA strategy was evaluated in a single-cylinder GT-Suite model integrated with the newly developed GCI combustion model. The effect of VVA on in-cylinder condition and GCI combustion was simulated at 1250 rpm 3bar IMEP. The VVA strategies considered in this simulation are EEVO, LEVO, PVO, NVO, and exhaust RB with timings and lifts. The exhaust gas RB strategy was identified as the most effective method to increase TIVC, TEVO, and internal residual gas fraction by re-introducing exhaust gas during intake stroke. 33 K, 83 K, and 20.6 % increase in TIVC, TEVO, and residual gas fraction were observed, respectively, leading to an 8.9 bar and 0.5 bar increase in peak in-cylinder pressure and IMEP, respectively.
- The non-uniform distribution of flow velocity at the inlet of the CC-SCR was identified based on ConvergeCFD simulation results. This observation brought a necessity for a model capable of simulating the inhomogeneity. A 3D SCR model offered by GT-Suite was utilized to simulate uniform and non-uniform inlet species distribution. Up to a 7.6 % discrepancy was observed between the two cases.
- Various volumes and geometries of CC-SCR were evaluated using GT-Suite based on HD diesel cold FTP cycle test results. The effects of the volume of CC-SCR on the NOx reduction rate were investigated with two scenarios: 1) increased volume of total SCR by adding CC-SCR to the existing main SCR (15.7 L) and 2) adding CC-SCR and reducing existing main SCR volume, keeping the total volume constant (15.7 L). It was observed that CC-SCR had a faster (41 %) light-off time than that of the main SCR only case, resulting in a higher NOx reduction rate in both scenarios. Two scenarios revealed minor differences in tailpipe NOx, showing that the impact of the main SCR was not significant under the operating conditions examined.

- Additionally, diameter showed a higher impact on the performance of CC-SCR among the cases whose volume was kept constant. The CC-SCR, with a diameter of 9 inches, 30 % volume of the original main SCR (15.7 L), and a total SCR volume of 15.7 L, showed the most compromised performance under the HD cold FTP cycle. It was observed that 80 % of total NOx reduction occurred at CC-SCR, and 20 % was reduced at the main SCR, indicating the significant contribution of the CC-SCR.

7.2 Future Work

The PPCI-diffusion GCI combustion model has been developed based on limited engine testing results for both CFD and quasi-dimension phenomenological model validation. Model fidelity and reliability can be further improved. In addition, the existing 3D SCR model can be further improved if the following is considered in the future.

- Further CFD and GCI combustion model validation can be carried out over broad operating conditions against engine testing results.
- The phenomenological spray jet combustion model is based on the Lagrangian approach by introducing a finite number of packets into the combustion chamber. The limited number of packets can cause computational error and spiky heat release. Eulerian approach may be able to reduce this intrinsic limitation.
- Engine-out emissions are the main parameters during the combustion optimization. Considering the significant impact of aftertreatment and turbocharger on tailpipe emissions, fast warm-up measures, such as rebreathing, should be included in an engine system performance optimization process.
- The existing SCR catalyst model can be improved by accounting for the non-uniform

distribution of the individual species. Also, a mixer should be included because a mixer plays a vital role in urea injection, atomization, mixing with exhaust gas, and distribution at the inlet of SCR.

- For computationally effective simulation, an efficient algorithm of switching 1D and 3D SCR models should be considered to accurately evaluate the performance of SCR with less computational need, especially during transient operation simulation.

Reference

[1] IEA (2021), "Tracking Transport 2021 – Analysis - IEA." https://www.iea.org/reports/tracking-transport-2021

[2] US EPA. "Final Rule to Revise Existing National GHG Emissions Standards for Passenger Cars and Light Trucks Through Model Year 2026." https://www.epa.gov/regulations-emissions-vehicles-and-engines/final-rule-revise-existing-national-ghg-emissions

[3] P. Bielaczyc and J. Merkisz, "Euro III / Euro IV Emissions - A Study of Cold Start and Warm Up Phases with a SI (Spark Ignition) Engine,", SAE Technical Paper 1999-01-1073, 1999, doi: 10.4271/1999-01-1073.

[4] M. Weilenmann, J.-Y. Favez, and R. Alvarez, "Cold-start emissions of modern passenger cars at different low ambient temperatures and their evolution over vehicle legislation categories," *Atmospheric Environment,* vol. 43, no. 15, pp. 2419-2429, 2009/05/01/ 2009, doi: https://doi.org/10.1016/j.atmosenv.2009.02.005.

[5] D. Ball *et al.*, "Investigation of LEV-III Aftertreatment Designs," *SAE International Journal of Fuels and Lubricants,* vol. 4, no. 1, pp. 1-8, 2011.

[6] A. Russell and W. S. Epling, "Diesel Oxidation Catalysts," *Catalysis Reviews,* vol. 53, no. 4, pp. 337-423, 2011/10/01 2011, doi: 10.1080/01614940.2011.596429.

[7] C. M. Schär *et al.*, "Control of a Urea SCR Catalytic Converter System for a Mobile Heavy Duty Diesel Engine," SAE Technical Paper 2003-01-0776, 2003, doi: 10.4271/2003-01-0776.

[8] G. T. Kalghatgi, "Auto-Ignition Quality of Practical Fuels and Implications for Fuel Requirements of Future SI and HCCI Engines," SAE Technical Paper 2005-01-0239, 2005, doi: 10.4271/2005-01-0239.

[9] F. J. Jiménez-Espadafor *et al.*,"Experimental analysis of low temperature combustion mode with diesel and biodiesel fuels: A method for reducing NOx and soot emissions," *Fuel Processing Technology,* vol. 103, pp. 57-63, 2012/11/01/ 2012, doi: https://doi.org/10.1016/j.fuproc.2011.11.014.

[10] K. Epping *et al.*, "The Potential of HCCI Combustion for High Efficiency and Low Emissions," SAE Technical Paper 2002-01-1923, 2002, doi: 10.4271/2002-01-1923.

[11] *Combustion : Physical and Chemical Fundamentals, Modeling and Simulation, Experiments, Pollutant Formation*. (2006). Springer-Verlag, Heidelberg.

[12] R. M. Hanson *et al.*, "An Experimental Investigation of Fuel Reactivity Controlled PCCI Combustion in a Heavy-Duty Engine," *SAE International Journal of Engines,* vol. 3, no. 1, pp. 700-716, 2010, doi: 10.4271/2010-01-0864.

[13] S. L. Kokjohn *et al.*, "Fuel reactivity controlled compression ignition (RCCI): a pathway to controlled high-efficiency clean combustion:," *http://dx.doi.org/10.1177/1468087411401548,* research-article 2011-06-22 2011, doi: 10.1177_1468087411401548.

[14] S. L. Kokjohn *et al.*, "Experiments and Modeling of Dual-Fuel HCCI and PCCI Combustion Using In-Cylinder Fuel Blending," *SAE International Journal of Engines,* vol. 2, no. 2, pp. 24-39, 2009, doi: 10.4271/2009-01-2647.

[15] A. B. Dempsey, S. J. Curran, and R. M. Wagner, "A perspective on the range of gasoline compression ignition combustion strategies for high engine efficiency and low NOx and

soot emissions: Effects of in-cylinder fuel stratification*:,"*http://dx.doi.org/10.1177/1468087415621805,* research-article 2016-01-14 2016, doi: 10.1177_1468087415621805.

[16] M. Sjöberg and J. E. Dec, "Comparing late-cycle autoignition stability for single- and two-stage ignition fuels in HCCI engines," *Proceedings of the Combustion Institute,* vol. 31, no. 2, pp. 2895-2902, 2007/01/01/ 2007, doi: https://doi.org/10.1016/j.proci.2006.08.010.

[17] R. K. Maurya, "Characteristics and Control of Low Temperature Combustion Engines : Employing Gasoline, Ethanol and Methanol", 1st 2018. ed. Cham: Springer International Publishing : Imprint: Springer, 2018.

[18] S. Saxena and I. D. Bedoya, "Fundamental phenomena affecting low temperature combustion and HCCI engines, high load limits and strategies for extending these limits," *Progress in Energy and Combustion Science,* vol. 39, no. 5, pp. 457-488, 2013/10/01/ 2013, doi: https://doi.org/10.1016/j.pecs.2013.05.002.

[19] F. Zhao, *Homogeneous Charge Compression Ignition (HCCI) Engines*. SAE International, 2003.

[20] H. Guo, H. Li, and W. S. Neill, "A Study on the Performance of Combustion in a HCCI Engine Using n-Heptane by a Multi-Zone Model," presented at the ASME 2009 Internal Combustion Engine Division Fall Technical Conference, 2009.

[21] H. Li *et al.*, "An Experimental and Modeling Study of HCCI Combustion Using n-Heptane," Proceedings of the ASME 2006 Internal Combustion Engine Division Fall Technical Conference, 2006.

[22] B. Lawler *et al.*, "Thermally Stratified Compression Ignition: A new advanced low temperature combustion mode with load flexibility," *Applied Energy,* vol. 189, pp. 122-132, 2017/03/01/ 2017, doi: https://doi.org/10.1016/j.apenergy.2016.11.034.

[23] M. R. Boldaji *et al.*, "Computational fluid dynamics investigations of the effect of water injection timing on thermal stratification and heat release in thermally stratified compression ignition combustion," *https://doi.org/10.1177/1468087418767451, International Journal of Engine Research. 2019;20(5):555-569.* doi: 10.1177_1468087418767451.

[24] C. Noehre *et al.*, "Characterization of Partially Premixed Combustion," SAE Technical Paper 2006-01-3412, 2006, doi: 10.4271/2006-01-3412.

[25] W. L. Hardy and R. D. Reitz, "A Study of the Effects of High EGR, High Equivalence Ratio, and Mixing Time on Emissions Levels in a Heavy-Duty Diesel Engine for PCCI Combustion," SAE Technical Paper 2006-01-0026, 2006, doi: 10.4271/2006-01-0026.

[26] Y. Takeda and N. Keiichi, "Emission Characteristics of Premixed Lean Diesel Combustion with Extremely Early Staged Fuel Injection," SAE Technical Paper 961163, 1996, doi: 10.4271/961163.

[27] T. Hashizume *et al.*, "Combustion and Emission Characteristics of Multiple Stage Diesel Combustion," SAE 980505, 1998, doi: 10.4271/980505.

[28] V. Manente, B. Johansson, and P. Tunestal, "Partially Premixed Combustion at High Load using Gasoline and Ethanol, a Comparison with Diesel," SAE Technical Paper 2009-01-0944, 2009, doi: 10.4271/2009-01-0944.

[29] C. P. Kolodziej *et al.*, "Operation of a Gasoline Direct Injection Compression Ignition Engine on Naphtha and E10 Gasoline Fuels," *SAE International Journal of Engines,* vol. 9, no. 2, pp. 979-1001, 2016, doi: 10.4271/2016-01-0759.

[30] K. Cho *et al.*, "Gasoline Fuels Assessment for Delphi's Second Generation Gasoline Direct-Injection Compression Ignition (GDCI) Multi-Cylinder Engine," *SAE International Journal of Engines,* vol. 10, no. 4, pp. 1430-1442, 2017, doi: 10.4271/2017-01-0743.

[31] M. Sellnau *et al.*, "Gasoline Direct Injection Compression Ignition (GDCI) - Diesel-like Efficiency with Low CO2 Emissions," *SAE International Journal of Engines,* vol. 4, no. 1, pp. 2010-2022, 2011, doi: 10.4271/2011-01-1386.

[32] M. C. Sellnau *et al.*, "Full-Time Gasoline Direct-Injection Compression Ignition (GDCI) for High Efficiency and Low NOx and PM," *SAE International Journal of Engines,* vol. 5, no. 2, pp. 300-314, 2012, doi: 10.4271/2012-01-0384.

[33] M. Sellnau *et al.*, "Development of a Gasoline Direct Injection Compression Ignition (GDCI) Engine," *SAE International Journal of Engines,* vol. 7, no. 2, pp. 835-851, 2014, doi: 10.4271/2014-01-1300.

[34] M. Sellnau *et al.*, "GDCI Multi-Cylinder Engine for High Fuel Efficiency and Low Emissions," *SAE International Journal of Engines,* vol. 8, no. 2, pp. 775-790, 2015, doi: 10.4271/2015-01-0834.

[35] M. Sellnau *et al.*, "Pathway to 50% Brake Thermal Efficiency Using Gasoline Direct Injection Compression Ignition*",* SAE Int. J. Adv. & Curr. Prac. in Mobility 1(4):1581-1603, 2019, https://doi.org/10.4271/2019-01-1154.

[36] K. Cho *et al.*, "Investigation of Fuel Effects on Combustion Characteristics of Partially Premixed Compression Ignition (PPCI) Combustion Mode at Part-Load Operations," *SAE International Journal of Engines,* vol. 11, no. 6, pp. 1371-1383, 2018, doi: 10.4271/2018-01-0897.

[37] Y. Zhang *et al.*, "CFD-Guided Combustion Strategy Development for a Higher Reactivity Gasoline in a Light-Duty Gasoline Compression Ignition Engine," SAE Technical Paper 2017-01-0740, 2017, doi: 10.4271/2017-01-0740.

[38] Y. Zhang *et al.*, "An Experimental and Computational Investigation of Gasoline Compression Ignition Using Conventional and Higher Reactivity Gasolines in a Multi-Cylinder Heavy-Duty Diesel Engine," SAE Technical Paper 2018-01-0226, 2018, doi: 10.4271/2018-01-0226.

[39] Y. Zhang and M. Sellnau, "A Computational Investigation of PPCI-Diffusion Combustion Strategy at Full Load in a Light-Duty GCI Engine," *SAE International Journal of Advances and Current Practices in Mobility,* vol. 3, no. 4, pp. 1757-1775, 2021, doi: 10.4271/2021-01-0514.

[40] M. Yıldız and B. Albayrak Çeper, "Zero-dimensional single zone engine modeling of an SI engine fuelled with methane and methane-hydrogen blend using single and double Wiebe Function: A comparative study," *International Journal of Hydrogen Energy,* vol. 42, no. 40, pp. 25756-25765, 2017/10/05/ 2017, doi: https://doi.org/10.1016/j.ijhydene.2017.07.016.

[41] S. Awad *et al.*, "Single zone combustion modeling of biodiesel from wastes in diesel engine," *Fuel,* vol. 106, pp. 558-568, 2013/04/01/ 2013, doi: https://doi.org/10.1016/j.fuel.2012.11.051.

[42] F. Maroteaux, C. Saad, and F. Aubertin, "Development and validation of double and single Wiebe function for multi-injection mode Diesel engine combustion modelling for hardware-in-the-loop applications," *Energy Conversion and Management,* vol. 105, pp. 630-641, 2015/11/15/ 2015, doi: https://doi.org/10.1016/j.enconman.2015.08.024.

[43] J. Zhu *et al.*, "Development and Validation of a Modeling and Calibration Method for Diesel-Like Multistage Combustion Based On a Modified Multi-Wiebe Function," *ACS Omega,* vol. 7, no. 14, pp. 11756-11769, 2022/04/12 2022, doi: 10.1021/acsomega.1c06858.

[44] Gamma technologies, "GT-Suite v2022 Manual."

[45] T. Yoshizaki, K. Nishida, and H. Hiroyasu, "Approach to Low NOx and Smoke Emission Engines by Using Phenomenological Simulation," SAE Technical Paper 930612, 1993, doi: 10.4271/930612.

[46] D. Jung and D. N. Assanis, "Multi-Zone DI Diesel Spray Combustion Model for Cycle Simulation Studies of Engine Performance and Emissions," SAE 2001-01-1246, 2001, doi: 10.4271/2001-01-1246.

[47] H. Hiroyasu, T. Kadota, and M. Arai, "Development and Use of a Spray Combustion Modeling to Predict Diesel Engine Efficiency and Pollutant Emissions : Part 1 Combustion Modeling," *Bulletin of JSME,* vol. 26, no. 214, pp. 569-575, 1983, doi: 10.1299/jsme1958.26.569.

[48] C. D. Rakopoulos *et al.*, "Investigating the EGR rate and temperature impact on diesel engine combustion and emissions under various injection timings and loads by comprehensive two-zone modeling," *Energy,* vol. 157, pp. 990-1014, 2018/08/15/ 2018, doi: https://doi.org/10.1016/j.energy.2018.05.178.

[49] R. C. Li, G. G. Zhu, and Y. Men, "A two-zone reaction-based combustion model for a spark-ignition engine", *https://doi.org/10.1177/1468087419841746, International Journal of Engine Research*, 2021, 22(1):109-124*,* doi: 10.1177_1468087419841746.

[50] M. Bissoli *et al.*, "A new predictive multi-zone model for HCCI engine combustion," *Applied Energy,* vol. 178, pp. 826-843, 2016/09/15/ 2016, doi: https://doi.org/10.1016/j.apenergy.2016.06.062.

[51] P. Kongsereeparp and M. D. Checkel, "Novel Method of Setting Initial Conditions for Multi-Zone HCCI Combustion Modeling," SAE Technical Paper 2007-01-0674, 2007, doi: 10.4271/2007-01-0674.

[52] W. L. Easley, A. Agarwal, and G. A. Lavoie, "Modeling of HCCI Combustion and Emissions Using Detailed Chemistry," SAE Technical Paper 2001-01-1029, 2001, doi: 10.4271/2001-01-1029.

[53] J. M. Garcia-Guendulain *et al.*, "Computationally efficient evaluation of optimum homogeneous charge compression ignition operating range with accelerated multizone engine cycle simulation," *International Journal of Engine Research,* vol. 22, no. 7, pp. 2293-2304, 2021/07/01 2020, doi: 10.1177/1468087420929488.

[54] L. Liu *et al.*, "A review of phenomenological spray penetration modeling for diesel engines with advanced injection strategy," *International Journal of Spray and Combustion Dynamics,* vol. 12, p. 1756827720934067, 2020/01/01 2020, doi: 10.1177/1756827720934067.

[55] I. Najar *et al.*, "Review of 1D Spray Tip Penetration Models and Fuel Properties Influence on Spray Penetration," *SAE International Journal of Engines,* vol. 13, no. 4, pp. 521-544, 2020.

[56] L. Hausfelder, "Kompressorlose Dieselmaschinen," Berlin: Julius Springer, 1929.

[57] Y. Wakuri *et al.*, "Studies on the Penetration of Fuel Spray in a Diesel Engine," *Bulletin of JSME,* vol. 3, no. 9, pp. 123-130, 1960, doi: 10.1299/jsme1958.3.123.

[58] J. C. Dent, "A Basis for the Comparison of Various Experimental Methods for Studying

Spray Penetration," SAE Technical Paper 710571, https://doi.org/10.4271/710571.

[59] M. Arai, "Physics behind Diesel Sprays," ICLASS Congerence, 2012.

[60] J. D. Naber, S. N. Labs., D. L. Siebers, and S. N. Labs., "Effects of Gas Density and Vaporization on Penetration and Dispersion of Diesel Sprays," SAE Technical Paper 960034, 1996, doi: 10.4271/960034.

[61] W. S. Chiu, S. M. Shahed, and W. T. Lyn, "A Transient Spray Mixing Model for Diesel Combustion," *SAE Transactions,* vol. 85, pp. 502-512, 1976.

[62] J. M. Desantes *et al.*, "Development and validation of a theoretical model for diesel spray penetration," *Fuel,* vol. 85, no. 7, pp. 910-917, 2006/05/01/ 2006, doi: https://doi.org/10.1016/j.fuel.2005.10.023.

[63] R. Payri *et al.*, "On the dependence of spray momentum flux in spray penetration: Momentum flux packets penetration model," *Journal of Mechanical Science and Technology,* vol. 21, no. 7, pp. 1100-1111, 2007/07/01 2007, doi: 10.1007/BF03027660.

[64] M. Musculus *et al.*, "End-of-Injection Over-Mixing and Unburned Hydrocarbon Emissions in Low-Temperature-Combustion Diesel Engines," SAE Technical Paper 2007-01-0907, 2007, doi: 10.4271/2007-01-0907.

[65] M. Musculus and K. Kattke, "Entrainment Waves in Diesel Jets," *SAE International Journal of Engines,* vol. 2, pp. 1170-1193, 10/15 2009, doi: 10.4271/2009-01-1355.

[66] V. Yakhot and S. A. Orszag, *Renormalization group analysis of turbulence. I. Basic theory*. S.l: s.n. 1986.

[67] J. Gorman *et al.*, "Turbulence Models Commonly Used in CFD," 2021.

[68] R. Reitz and R. Diwakar, "Structure of High-Pressure Fuel Sprays," SAE Technical Paper 870598, 1987.

[69] H. J. Kull, "Theory of the Rayleigh-Taylor instability," *Physics Reports,* vol. 206, no. 5, pp. 197-325, 1991/08/01/ 1991, doi: https://doi.org/10.1016/0370-1573(91)90153-D.

[70] A. A. Amsden, P. J. O'Rourke, and T. D. Butler, "KIVA-II: A computer program for chemically reactive flows with sprays," United States: N. p., 1989. Web. doi:10.2172/6228444.

[71] S. L. Post and J. Abraham, "Modeling the outcome of drop–drop collisions in Diesel sprays," *International Journal of Multiphase Flow,* vol. 28, no. 6, pp. 997-1019, 2002/06/01/ 2002, doi: https://doi.org/10.1016/S0301-9322(02)00007-1.

[72] D. P. Schmidt and C. J. Rutland, "A New Droplet Collision Algorithm," *Journal of Computational Physics,* vol. 164, no. 1, pp. 62-80, 2000/10/10/ 2000, doi: https://doi.org/10.1006/jcph.2000.6568.

[73] Y. Li *et al.*, "Development of a reduced four-component (toluene/n-heptane/iso-octane/ethanol) gasoline surrogate model," *Fuel,* vol. 247, pp. 164-178, 2019/07/01/ 2019, doi: https://doi.org/10.1016/j.fuel.2019.03.052.

[74] V. I. Golovitchev *et al.*, "3-D Diesel Spray Simulations Using a New Detailed Chemistry Turbulent Combustion Model," *SAE Transactions,* vol. 109, pp. 1391-1405, 2000.

[75] S. Xu, *et al.*, "Quasi-Dimensional Diesel Engine Combustion Modeling With Improved Diesel Spray Tip Penetration, Ignition Delay, and Heat Release Submodels," *Journal of Engineering for Gas Turbines and Power,* vol. 139, no. 11, 2017, doi: 10.1115/1.4036575.

[76] T. Tzanetakis *et al.*, "Non-Reacting Spray Characteristics of Gasoline and Diesel With a Heavy-Duty Single-Hole Injector," *Frontiers in Mechanical Engineering,* Original Research vol. 8, 2022.

[77] A. A. Osorio, X. Tauzia, and A. Maiboom, "Development of a wall jet model dedicated to 1D combustion modelling for CI engines," *International Journal of Spray and Combustion Dynamics,* vol. 13, no. 3-4, pp. 146-163, 2021/09/01 2021, doi: 10.1177/17568277211059073.

[78] R. D. Reitz and F. B. Bracco, ""On the Dependence of Spray Angle and Other Spray Parameters on Nozzle Design and Operating Conditions," SAE Technical Paper 790494, 1979, https://doi.org/10.4271/790494.

[79] K. H. Kwak, D. Jung, and C. Borgnakke, "Enhanced spray and evaporation model with multi-fuel mixtures for direct injection internal combustion engines," *International Journal of Engine Research,* vol. 15, no. 4, pp. 488-503, 2014/06/01 2013, doi: 10.1177/1468087413495203.

[80] S. G. Poulos and J. B. Heywood, "The Effect of Chamber Geometry on Spark-Ignition Engine Combustion," *SAE Transactions,* vol. 92, pp. 1106-1129, 1983.

[81] J. B. Heywood, *Internal Combustion Engine Fundamentals*, 2nd Edition ed. New York: McGraw-Hill Education, 2018.

[82] D. DelVescovo, S. Kokjohn, and R. Reitz, "The Development of an Ignition Delay Correlation for PRF Fuel Blends from PRF0 (n-Heptane) to PRF100 (iso-Octane)," *SAE International Journal of Engines,* vol. 9, no. 1, pp. 520-535, 2016.

[83] J. C. Livengood and P. C. Wu, "Correlation of autoignition phenomena in internal combustion engines and rapid compression machines," *Symposium (International) on Combustion,* vol. 5, no. 1, pp. 347-356, 1955/01/01/ 1955, doi: https://doi.org/10.1016/S0082-0784(55)80047-1.

[84] H. Hiroyasu, T. Kadota, and M. Arai, "Development and Use of a Spray Combustion Modeling to Predict Diesel Engine Efficiency and Pollutant Emissions : Part 2 Computational Procedure and Parametric Study," *Bulletin of JSME,* vol. 26, no. 214, pp. 576-583, 1983, doi: 10.1299/jsme1958.26.576.

[85] C. K. Westbrook and F. L. Dryer, "Simplified Reaction Mechanisms for the Oxidation of Hydrocarbon Fuels in Flames," *Combustion Science and Technology,* vol. 27, no. 1-2, pp. 31-43, 1981/12/01 1981, doi: 10.1080/00102208108946970.

[86] P. Kumar, M. Sellnau, A. Shah, C. Whitney, and R. Sari, "Development of Two-Step Exhaust Rebreathing for a Low-NOx Light-Duty Gasoline Compression Ignition Engine," *Energies*, vol. 15, no. 18, doi: 10.3390/en15186565.

[87] M. Colombo, G. Koltsakis, I. Nova, and E. Tronconi, "Modelling the ammonia adsorption–desorption process over an Fe–zeolite catalyst for SCR automotive applications," *Catalysis Today,* vol. 188, no. 1, pp. 42-52, 2012/07/01/ 2012, doi: https://doi.org/10.1016/j.cattod.2011.09.002.

[88] D. Chatterjee, *et al.*,"Numerical Simulation of Zeolite- and V-Based SCR Catalytic Converters," SAE Technical Paper 2007-04-16, 2007.

[89] Z. Gao, *et al.*, "Engine-Aftertreatment in Closed-Loop Modeling for Heavy Duty Truck Emissions Control," SAE Technical Paper 2019-04-02, 2019.

Appendix I Reduced TPRF-E Mechanism

C6H5CH3+OH<=>C6H5CH2+H2O
C6H5CH3+O2<=>C6H5CH2+HO2
C6H5CH2+OH<=>C6H5CHO+H2
C6H5CH2+HO2<=>C6H5CHO+H2O
C6H5CH2+O<=>C6H5CHO+H
C6H5CH2+O<=>C6H5+CH2O
C6H5CH3(+M)<=>C6H5CH2+H(+M)
C6H5CH3(+M)<=>C6H5+CH3(+M)
C6H5CH3+H<=>C6H6+CH3
C6H5CHO+H<=>C6H5CO+H2
C6H5CHO+OH<=>C6H5CO+H2O
C6H5+CO<=>C6H5CO
C6H5+H(+M)<=>C6H6(+M)
C6H6+H<=>C6H5+H2
C6H6+O<=>C6H5+OH
C6H6+OH<=>C6H5+H2O
C6H5+O2<=>C6H5O+O
C6H5O<=>CO+C5H5
C5H5+O<=>C4H5-N+CO
C2H3+C2H2<=>C4H5-N
NC7H16+O2<=>NC7H15+HO2
NC7H16+OH=>NC7H15+H2O
NC7H16+HO2=>NC7H15+H2O2
NC7H15+O2<=>NC7H15OO
NC7H15OO<=>NC7H14OOH
NC7H14OOH+O2<=>OONC7H14OOH
OONC7H14OOH=>NC7KET+OH
NC7KET=>OH+CH2O+NC5H11CO
NC5H11CO+O2=>IC3H7+C2H3+CO+HO2
NC7H15OO<=>NC7H14+HO2
NC7H14+O2=>C3H6+C2H5+CH2O+HCO
NC7H15=>C3H6+C2H5+C2H4
IC8H18+HO2<=>C8H17+H2O2
IC8H18+O2<=>C8H17+HO2
IC8H18+OH<=>C8H17+H2O
C8H17=>IC3H7+C3H6+C2H4
C8H17+O2<=>C8H17O2
C8H17O2<=>C8H16OOH
C8H17O2<=>C8H16+HO2
C8H16OOH+O2<=>C8H16OOH-O2
C8H16OOH-O2<=>IC8KET+OH
C8H16+O2=>IC3H7+CH4+C2H2+CH2O+HCO
IC8KET<=>CH2O+CH3+OH+C4H8-1+CH2CO
H2+M<=>H+H+M
H2+O<=>H+OH
H2+OH<=>H+H2O
O+O+M<=>O2+M
O2+H<=>O+OH
H+OH+M<=>H2O+M
O+H2O<=>OH+OH
O+H+M<=>OH+M
H2O2(+M)<=>OH+OH(+M)
H2O2+H<=>H2O+OH
H2O2+H<=>H2+HO2
H2O2+O<=>OH+HO2
H2O2+OH<=>H2O+HO2
H2O2+OH<=>H2O+HO2
HO2+H<=>OH+OH
HO2+H<=>H2+O2
HO2+O<=>OH+O2
OH+HO2<=>H2O+O2
OH+HO2<=>H2O+O2
HO2+HO2<=>H2O2+O2
HO2+HO2<=>H2O2+O2
H+O2(+M)<=>HO2(+M)
CO+O(+M)<=>CO2(+M)
CO+OH<=>CO2+H
CO+OH<=>CO2+H
CO+HO2<=>CO2+OH
CO+O2<=>CO2+O
CH3+H(+M)<=>CH4(+M)
CH4+H<=>CH3+H2
CH4+O<=>CH3+OH
CH4+OH<=>CH3+H2O
CH4+HO2<=>CH3+H2O2
CH3+HO2<=>CH4+O2
CH4+CH2<=>CH3+CH3
CH2+H(+M)<=>CH3(+M)
CH2+O2<=>HCO+OH
CH2+O2=>CO2+H+H
CH2+O=>CO+H+H

CH2+H<=>CH+H2
CH2+OH<=>CH+H2O
CH+O2<=>HCO+O
CH+O<=>CO+H
CH+OH<=>HCO+H
CH+H2O<=>H+CH2O
CH+CO2<=>HCO+CO
CH3+O2(+M)<=>CH3O2(+M)
CH3+O2<=>CH3O+O
CH3+O2<=>CH2O+OH
CH3+O<=>CH2O+H
CH3+OH<=>CH2O+H2
CH3+OH<=>CH2OH+H
CH3+OH<=>H+CH3O
CH3+OH<=>CH2+H2O
CH3+HO2<=>CH3O+OH
CH3O2+O<=>CH3O+O2
CH3O2+H<=>CH3O+OH
CH3O2+OH<=>CH3OH+O2
CH3O2+CH3<=>CH3O+CH3O
CH3O2+CH3O2=>CH2O+CH3OH+O2
CH3O2+CH3O2=>O2+CH3O+CH3O
CH3OH(+M)<=>CH3+OH(+M)
CH3OH(+M)<=>CH2OH+H(+M)
CH3OH+H<=>CH3O+H2
CH3OH+H<=>CH2OH+H2
CH3OH+O<=>CH3O+OH
CH3OH+O<=>CH2OH+OH
CH3OH+OH<=>CH3O+H2O
CH3OH+OH<=>CH2OH+H2O
CH3OH+O2<=>CH3O+HO2
CH3OH+O2<=>CH2OH+HO2
CH3OH+HO2<=>CH3O+H2O2
CH3OH+HO2<=>CH2OH+H2O2
CH3OH+CH3<=>CH2OH+CH4
CH3OH+CH3<=>CH3O+CH4
CH3OH+HCO<=>CH2OH+CH2O
CH3OH+CH3O<=>CH2OH+CH3OH
CH2OH+O2<=>CH2O+HO2
CH2OH+O2<=>CH2O+HO2
CH2OH+H<=>CH2O+H2
CH2OH+HO2<=>CH2O+H2O2
CH2OH+HCO<=>CH2O+CH2O
CH2OH+HCO<=>CH3OH+CO
CH2OH+CH3O<=>CH2O+CH3OH
CH2OH+OH<=>H2O+CH2O
CH2OH+O<=>OH+CH2O
CH2OH+CH2OH<=>CH2O+CH3OH
CH3O+O2<=>CH2O+HO2
CH3O+H<=>CH2O+H2
CH3O+HO2<=>CH2O+H2O2
CH3O+CH3<=>CH2O+CH4
CH3O+CH3O<=>CH3OH+CH2O
HCO+H(+M)<=>CH2O(+M)
CO+H2(+M)<=>CH2O(+M)
CH2O+O2<=>HCO+HO2
CH2O+O<=>HCO+OH
CH2O+H<=>HCO+H2
CH2O+OH<=>HCO+H2O
CH2O+HO2<=>HCO+H2O2
CH2O+CH3<=>HCO+CH4
CH2O+CH3O<=>HCO+CH3OH
HCO+M<=>H+CO+M
HCO+O2<=>CO+HO2
HCO+O<=>CO+OH
HCO+H<=>CO+H2
HCO+OH<=>CO+H2O
HCO+CH3<=>CH4+CO
HCO+HCO<=>CH2O+CO
HCO+O<=>CO2+H
HCO+HO2=>CO2+H+OH
HCO+HCO=>H2+CO+CO
CH2O+H(+M)<=>CH2OH(+M)
CH3O(+M)<=>CH2O+H(+M)
C2H4+H(+M)<=>C2H5(+M)
C2H5+H<=>C2H4+H2
C2H4+C2H4<=>C2H5+C2H3
C2H5+CH3<=>CH4+C2H4
CH3+CH3<=>H+C2H5
C2H5+O2<=>C2H4+HO2
C2H3+H(+M)<=>C2H4(+M)
C2H4+O2<=>C2H3+HO2
C2H4+H<=>C2H3+H2
C2H4+OH<=>C2H3+H2O
C2H4+CH3O<=>C2H3+CH3OH
C2H4+CH3<=>C2H3+CH4

C2H4+CH3<=>C2H3+CH4
C2H4+O<=>CH3+HCO
CH+CH4<=>C2H4+H
C2H4+OH<=>CH3+CH2O
C2H2+H(+M)<=>C2H3(+M)
C2H3+O2<=>C2H2+HO2
C2H3+O2<=>C2H2+HO2
C2H3+O2<=>CH2CO+OH
C2H3+O2<=>CH2CO+OH
C2H3+O2<=>CH2O+HCO
C2H3+O2<=>CH2O+HCO
C2H3+O2=>CH2O+H+CO
C2H3+O2=>CH2O+H+CO
C2H3+O2<=>CO+CH3O
C2H3+O2<=>CO+CH3O
C2H3+O2<=>CO2+CH3
C2H3+O2<=>CO2+CH3
C2H3+H<=>C2H2+H2
C2H3+OH<=>C2H2+H2O
C2H3+CH3<=>CH4+C2H2
C2H3+C2H3<=>C2H2+C2H4
C2H2+O<=>CH2+CO
C2H2+O<=>HCCO+H
C2H2+HO2<=>CH2CO+OH
C2H2+HCO<=>C2H3+CO
C2H2+OH<=>CH2CO+H
C2H2+OH<=>CH3+CO
CH3CO(+M)<=>CH3+CO(+M)
CH3CO(+M)<=>CH2CO+H(+M)
CH3CO+H<=>CH2CO+H2
CH3CO+O<=>CH2CO+OH
CH3CO+CH3<=>CH2CO+CH4
CH2+CO(+M)<=>CH2CO(+M)
CH2CO+H<=>HCCO+H2
CH2CO+O<=>HCCO+OH
CH2CO+OH<=>HCCO+H2O
CH2CO+H<=>CH3+CO
CH+CH2O<=>H+CH2CO
CH2CO+O<=>CH2+CO2
CH2CO+OH<=>CH2OH+CO
CH2CO+CH3<=>C2H5+CO
HCCO+OH=>H2+CO+CO
HCCO+O=>H+CO+CO
CH+CO+M<=>HCCO+M
HCCO+O2=>OH+CO+CO
HCCO+O2=>CO2+CO+H
CH+HCCO<=>CO+C2H2
CH3O+HCO<=>CH3OH+CO
IC3H7+H<=>C2H5+CH3
IC3H7+OH<=>C3H6+H2O
C2H3+CH3(+M)<=>C3H6(+M)
C2H3+CH3<=>C3H5-A+H
C2H3+CH3<=>C3H5-A+H
C3H6<=>C2H3+CH3
C3H6<=>C3H5-A+H
C3H6<=>C3H5-A+H
C3H6+H<=>C3H5-A+H2
C3H6+O2<=>C3H5-A+HO2
C3H6+O<=>C3H5-A+OH
C3H6+OH<=>C3H5-A+H2O
C3H6+HO2<=>C3H5-A+H2O2
C3H6+CH3<=>C3H5-A+CH4
C3H6+CH3O<=>C3H5-A+CH3OH
C3H6+O<=>C2H5+HCO
C3H6+O=>CH2CO+CH3+H
C3H6+H<=>C2H4+CH3
C3H6+H<=>C2H4+CH3
C3H6+H<=>IC3H7
C3H6+H<=>IC3H7
C3H6+HO2<=>IC3H7+O2
C3H5-A+C2H5<=>C2H4+C3H6
C3H5-A+HCO<=>C3H6+CO
C3H5-A+O2<=>CH3CO+CH2O
C2H3+CH2O<=>C2H4+HCO
C2H2+CH3<=>C3H5-A
C3H5-A+CH3(+M)<=>C4H8-1(+M)
C2H5+C2H3(+M)<=>C4H8-1(+M)
C4H8-1+H<=>C2H4+C2H5
C4H8-1+H<=>C2H4+C2H5
C4H8-1+H<=>C3H6+CH3
C4H8-1+H<=>C3H6+CH3
C4H8-1+O=>CH2CO+C2H5+H
C2H5+O<=>CH3CHO+H
C2H5+O2<=>CH3CHO+OH
CH3CHO(+M)<=>CH3+HCO(+M)
CH3CHO(+M)<=>CH4+CO(+M)

CH3CHO+H<=>CH3CO+H2
CH3CHO+O<=>CH3CO+OH
CH3CHO+OH<=>CH3CO+H2O
CH3CHO+O2<=>CH3CO+HO2
CH3CHO+CH3<=>CH3CO+CH4
CH3CHO+HO2<=>CH3CO+H2O2
C2H4+OH<=>CH3CHO+H
C2H5OH<=>C2H4+H2O
C2H5OH<=>C2H5+OH
C2H5OH+O2<=>SC2H4OH+HO2
C2H5OH+H<=>SC2H4OH+H2
C2H5OH+OH<=>SC2H4OH+H2O
C2H5OH+HO2<=>SC2H4OH+H2O2
C2H5OH+O<=>SC2H4OH+OH
C2H5OH+CH3<=>SC2H4OH+CH4
SC2H4OH<=>CH3CHO+H
SC2H4OH+O2<=>CH3CHO+HO2

Appendix II Reduced SCR Mechanism

NH3 + S1* ⇔ NH3S1*
NH3 + S2* ⇔ NH3S2*
H2O + S2* ⇔ H2OS2*
2NH3S1* + 1.5O2⇒N2 + 3H2O + 2S1*
2NH3S2* + 1.5O2⇒N2 + 3H2O + 2S2*
NO + 0.5O2 ⇔ NO2
4NH3S1* + 4NO + O2⇒4N2 + 6H2O + 4S1*
4NH3S2* + 4NO + O2⇒4N2 + 6H2O + 4S2*
4NH3S1* + 3NO2⇒3.5N2 + 6H2O + 4S1*
4NH3S2* + 3NO2⇒3.5N2 + 6H2O + 4S2*
2NH3S1* + 2NO2⇒N2 + NH4NO3S1* + H2O
NH4NO3S1* + NO⇒NO2 + N2 + 2H2O + S1*
2NH3S2* + 2NO2⇒N2 + NH4NO3S2* + H2O
NH4NO3S2* + NO⇒NO2 + N2 + 2H2O + S2*
NH4NO3S1* ⇒NH3S1* + NO2 + 0.25O2 + 0.5H2O
NH4NO3S2* ⇒NH3S2* + NO2 + 0.25O2 + 0.5H2O
2NH3S1* + 2NO + O2⇒N2 + N2O + 3H2O + 2S1*
2NH3S2* + 2NO2⇒N2 + N2O + 3H2O + 2S2*
N2O + 0.5O2⇒2NO